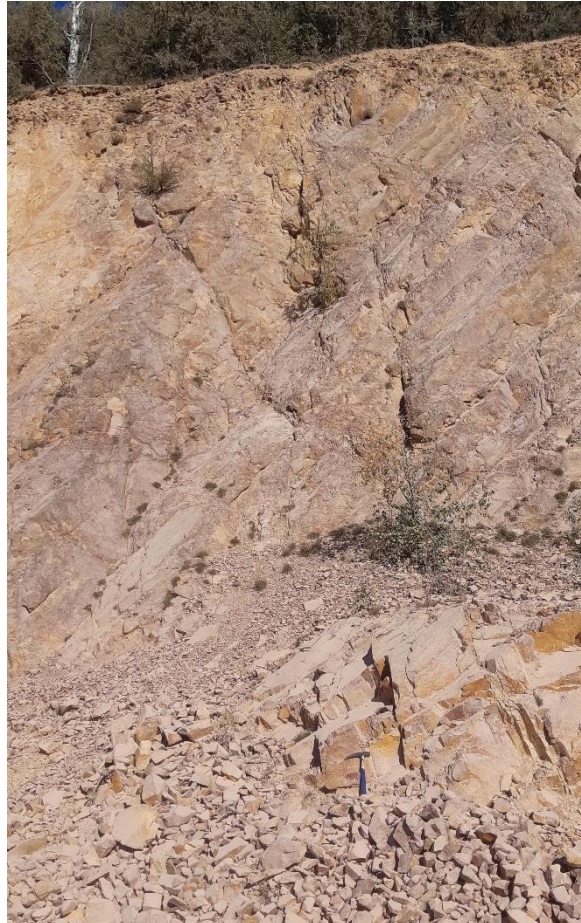


Petrological, Geochemical and Structural Characteristics of Rhyolite Dykes from the Freiberg District, Eastern Germany

Zanne E. R. Korevaar

14-4-2022



Supervisors:

Prof. Paul Mason – Utrecht University

Prof. Mike Buxton – TU Delft

Dr. Feven Desta – TU Delft



**Utrecht
University**



Delft
University of
Technology

Abstract

The Freiberg district in Eastern Germany hosts rhyolite dykes of early Permian age, that are associated with regional hydrothermal vein mineralization, but with an unknown origin and petrogenic evolution.

In this context, these dykes were investigated to determine the composition of their parental magmas and to constrain their magmatic evolution. A secondary goal was to identify the extent of any hydrothermal alteration associated with their emplacement. Twenty samples were collected from the dykes in outcrop as well as from associated blocks of uncertain provenance. Samples were selected to include generations one and three of the Sayda-Berggiesshübel dyke swarm (SBDS) and two dykes from north-west of the city of Freiberg that are not part of this swarm. Orientation and dip measurements were obtained during field work to further constrain the structural relationship between the dykes and their mineralogy was constrained by petrographic analysis. Fourier-transform Infra-Red (FTIR) spectroscopy and portable X-ray Fluorescence (pXRF) were used to determine alteration mineralogy. Bulk geochemical composition was determined by XRF and Inductively Coupled Plasma-Mass Spectroscopy (ICP-MS). Also, a table top Scanning Electron Microscope (TTSEM) was used to identify accessory minerals in some samples.

The degree of weathering in most samples was found to be small, and the mineralogical content and major geochemical signature of the dykes therefore closely corresponded to an estimated primary rhyolitic composition. However, their trace element and rare earth element (REE) patterns show a strong variability linked to varying degrees of magma evolution, especially controlled by accessory mineral fractionation. Key accessory minerals included zircon, titanite and iron-oxides. Trace element data also show a role for a phosphorus rich phase such as monazite or apatite, but this could not be found in the rocks. Especially for the north-western dyke system, titanite fractionation seems to have been important during magma evolution, supported by a strong middle rare earth element (MREE) depletion. This may suggest that these dykes were derived from a distinct magmatic system. In addition, several petrological disequilibrium textures such as oscillatory zoned K-feldspar, sieve textured feldspar and abundant resorbed quartz phenocrysts indicate the occurrence of one or more magma mixing events during magma evolution. This may be supported by ductile deformation structures as identified in the field, that have in previous work been interpreted to represent mixing with a more intermediate melt.

To place geological history of the dykes in a regional geological context, many of the geological characteristics of the dykes from the SBDS can similarly be applied to the neighbouring Teplice Rhyolite (TR) from the Altenberg Teplice Caldera (ATC). The common features for the TR and the SBDS such as three eruption cycles, a variable degree of magma evolution in their REE patterns and disequilibrium textures indicating the importance of magma mixing may suggest a genetic link between the two igneous units.

For a link between the rhyolite dykes and the regional hydrothermal system, a clue could be found in the abundant sericitic alteration that is identified in many of the samples from the SBDS. This alteration feature may be caused by the large-scale hydrothermal activity in the region that occurred after dyke emplacement. The anomalous behaviour of the redox-sensitive element Ce in some of the samples could be linked to this event. However, Ce concentrations could have also been influenced by accessory mineral fractionation. The link between the Freiberg rhyolite dykes and the regional hydrothermal system thus remains unclear.

Table of Contents

1. Introduction	4
2. Geological Background.....	6
3. Methods	9
3.1 Fieldwork and samples	9
3.2 Microscopy	9
3.3 Fourier-transform Infrared spectroscopy	9
3.4 Portable X-ray Fluorescence.....	10
3.5 Whole rock geochemistry	10
4. Results	11
4.1 Field observations	11
4.2 Major mineralogy and alteration features	15
4.3 FTIR spectroscopy and pXRF	17
4.4 Petrology.....	27
4.5 Textures linked to dyke emplacement	29
4.6 Accessory mineralogy	30
4.7 Geochemistry	33
5. Discussion	43
5.1 The influence of alteration processes	43
5.2 Flow differentiation.....	44
5.3 Fractional crystallization history	46
5.4 Magma mixing.....	51
5.5 Tectonic setting	53
5.6 Link between the Sayda-Berggiesshübel dyke swarm and the Altenberg Teplice Caldera.....	55
5.7 Link to hydrothermal system	60
6. Conclusions	63
7. Acknowledgements	65
8. References	66
Appendices	72
Appendix 1: Sample pictures.....	72
Appendix 2: Field measurements.....	84
Appendix 3: FTIR spectroscopic and pXRF chemical data	85
Appendix 4: Microscopic textural and alteration features.....	93
Appendix 5: Table-Top Scanning Electron Microscopy.....	94

1. Introduction

Dykes are common igneous features that form (sub-)vertical sheet-like intrusions in magmatic systems and facilitate important magma pathways in the Earth's crust (Kjøll et al., 2019). A large group of dykes is called a dyke swarm, in which individual dykes can range in length from meters up to tens of kilometres and in width from cm up to hundreds of metres (Ernst et al., 2001). Dyke emplacement usually accommodates tectonic extension and crustal heterogeneities and magma viscosity play an important role in emplacement mechanisms (Kjøll et al., 2019 and references therein). There are many examples of dyke swarms around the world, with a great variety in extent and magmatic composition (e.g. Independence dike swarm, U.S.A.; Carl & Glazner, 2002, Orano dyke swarm, Italy; Dini et al., 2008).

The Freiberg district, located in the Erzgebirge in eastern Germany (Figure 1), hosts part of the rhyolitic SBDS and further north-west to the city of Freiberg some small rhyolitic dykes are located that are not part of this group (Wetzel, 1984). The SBDS comprises more than 350 dykes that cross-cut the metamorphic basement in the area and all dykes in the district are of Permian age (Müller, 1901; Winter et al., 2008; Freymark et al., 2015). The district is well known for its large epithermal system with abundant polymetallic ore veins, where during the last centuries mainly silver mining was booming (Swinkels et al., 2019). In this context, its metallogeny, economical potential and geological history have been studied extensively. Recently, mineralisation of the veins has been linked to the large-scale early Permian magmatic activity in the region, indicated by geochemical, petrographic and geochronologic observations (Swinkels et al., 2021; Burisch et al., 2019 and references therein). However, relatively little research has been done on the rhyolite dykes of the SBDS and the other rhyolite dykes in the area (Wetzel, 1984; Winter et al., 2008; Freymark et al., 2015).

Winter et al. (2008) did some structural, petrological and geochemical work on the SBDS and mainly focussed on the genetic history of pyroclastic bodies, that are part of the dyke system, and the dykes' possible genetic relation with the surrounding larger igneous complexes. Freymark et al. (2015) investigated the Freiberg – Frauenstein (FF) dyke, also part of the SBDS, and looked into its emplacement mode and also correlation with neighbouring igneous centres. Older research, for example by Wetzel (1984), involved structural mapping and some geochemical work. However broad structural, petrological and chemical characterisation of the dykes has not been done before and little is currently known about the source magma of these rocks and their relation to the hydrothermal system in the area.

This MSc thesis has the main objective to structurally, petrologically and geochemically characterise the rhyolitic SBDS and the secluded north-western rhyolite dykes in the Freiberg district, with focus on identification of the magmatic source. The structural and petrological characteristics of the dykes may give information about the regional structure of the area, such as the location of the source intrusion and its geodynamic history. The chemical and mineralogical composition of the rhyolite could tell about the genetic evolution of the parental magma. Another goal for this research project is to search for any signs of hydrothermal influences and/or alteration and characterize a possible relationship between the dykes and the regional hydrothermal system.

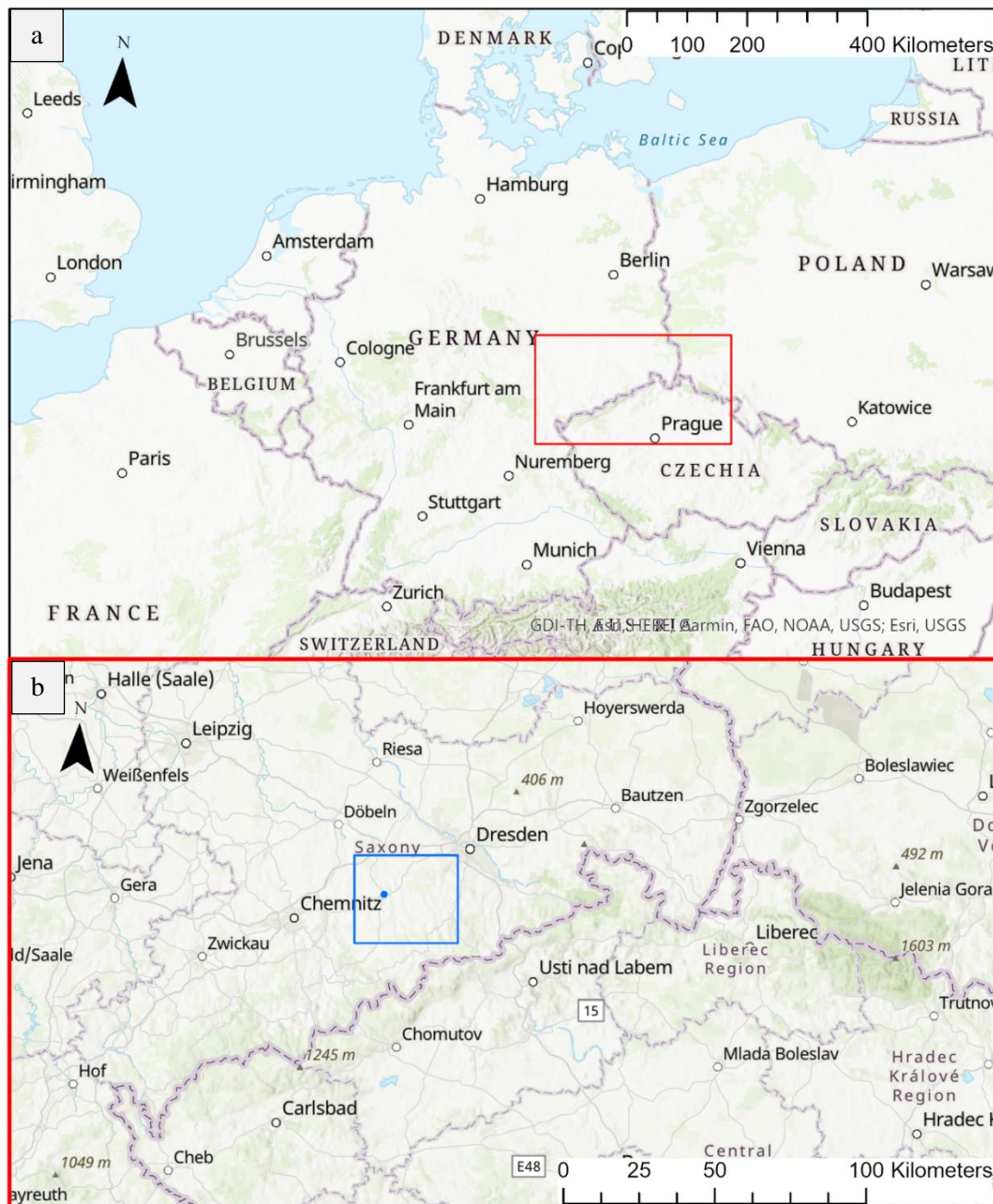


Figure 1: a) Map of northern Europe with indicated location of the Erzgebirge (red square). b) Map of part of the Erzgebirge (same area as red square in Figure 1a) with indicated location of the Freiberg district (blue square) and the city of Freiberg (blue dot). Map from ArcGIS® software by Esri. ArcGIS®: topographic basemap,

2. Geological Background

The Late Paleozoic collision of Gondwana and Laurussia resulted in the formation of Pangea and the Variscan orogeny (Kroner and Romer, 2013). The Saxo-Thuringian zone is part of the Variscan orogenic belt in Europe and is located at the north-western border of the Bohemian massif; a Gondwana related crustal block (Breiter et al., 1999; Kroner et al., 2007). The Saxo-Thuringian zone extends from Eastern Germany to the Czech Republic and hosts the mountain ridge of the Erzgebirge (Kroner et al., 2007).

The Erzgebirge comprises a nappe stack of initially sedimentary and granitic rocks that forms a NE-SW oriented anticlinorium along the German-Czech border (Casas-García et al., 2019 and references therein). At ~340 Ma, as obtained by $^{207}\text{Pb}/^{206}\text{Pb}$ dating of three metamorphosed zircons (340.5 ± 0.7 Ma, 341.2 ± 0.5 Ma and 341.6 ± 0.5 Ma), the sedimentary and granitic rocks were metamorphosed into gneisses, eclogites, mica-shists and phyllites (Kröner and Willner, 1998). After peak metamorphism and the Variscan orogenic climax, orogenic collapse caused an extensional regime and intrusion of voluminous, large scale, mainly acidic magmatism in the metamorphic basement between about 325 and 295 Ma (Förster et al., 1999; Burisch et al., 2019). Just after this period of rifting and acidic magmatism (280 Ma), a period of hydrothermal ore formation started in the Erzgebirge and lasted up until the Cenozoic (Bauer et al., 2019; Burisch et al., 2021). The magmatic activity that was caused by this rifting event is associated with the beginning of the ore formation in the area, as are several other distinct phases in the geological history of the Erzgebirge, eventually leading up to the formation of the extensive polymetallic epithermal vein system there is today (Burisch et al., 2021). The fieldwork area is located in the north-eastern Erzgebirge, around the city of Freiberg (Figure 2). The predominant lithology in the area is a gneiss unit that forms a dome-like body and was intruded multiple times during the post-collisional extension in the region (Swinkels et al., 2021). To the North-East, the area of interest is confined by the Niederbobritzscher biotite granite and the Tharandter Wald volcanic Complex (TWC) and east of the fieldwork area lies the ATC, all hosted by the gneiss unit (Swinkels et al., 2021 and references therein). The ATC consists of several plutonic and volcanic units, with both S-type and A-type affinities (Casas-García et al., 2021 and references therein). To the S-type units belong the pre-caldera Fláje biotite granite and the Schönfeld-Altenberg Depression Complex (SADS) with a peraluminous nature (Figure 2). The slightly peraluminous and normally zoned TR represents the caldera products, together with microgranitic ring dykes that were formed during caldera collapse (Figure 2). North-west and west of the fieldwork area lie mica-shists that have overthrust the Freiburger gneiss dome and further to the south more gneiss units are located (Swinkels et al., 2021 and references therein). Between the larger scale volcanic complexes in the area, numerous rhyolite and lamprophyre dykes have intruded the metamorphic basement (Winter et al., 2008; Swinkels et al., 2021 and references therein).

The SBDS comprises a large group of rhyolitic dykes that mostly lies between the TWVC and ATC with a mainly NE-SW striking orientation (Müller, 1901; Winter et al., 2008) (Figure 2). The dykes

have an extent from meters up to several kilometres in length and from decimetres up to hundreds of meters in width and are genetically related to the ATC as a vent and/or feeding system (Winter et al., 2008). A number of pyroclastic bodies are part of the SBDS that include circular and elongated lenses of welded rhyolitic tuff that represent ancient fall-back vent-fill (Winter et al., 2008). For the SBDS, three generations of dykes have previously been distinguished, of which the first and third generation are featured in the fieldwork area (Wetzel, 1984; Winter et al., 2008 and references therein). The FF dyke is from the first generation and represents the longest dyke in the system with a length of about 23 km and a contrasting NW-SE striking orientation (Figure 2). In older literature there is some debate about whether the dyke generations exist and, if so, how they are distributed (Kramer, 1962 and references therein). Also, the identification of the generations was based on poorly defined structural observations (Wetzel, 1984). Nevertheless, the idea and spatial distribution of the dyke generations as determined by Wetzel (1984) is adopted in all later work and therefore also in this thesis.

Other rhyolitic dykes, that are presumably not part of the SBDS and are unrelated to the larger scale intrusive complexes in the region, lie further north-west of Freiberg and the TWVC (Hoth et al., 1995). These dykes have a NNW-SSE striking orientation and were likely formed after the intrusion of the SBDS (Wetzel, 1984). However, the exact timing of formation is unknown and no previous geochronological or geochemical work has been done on these dykes.

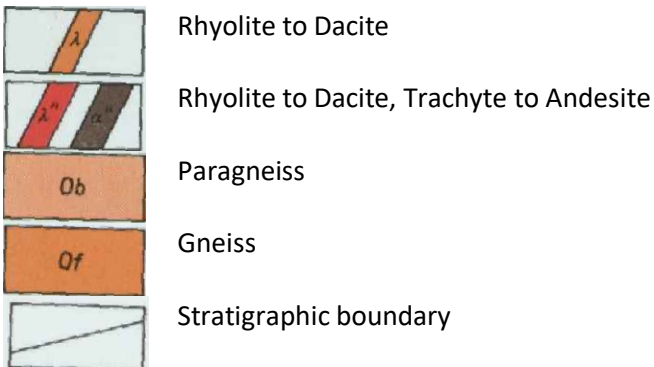
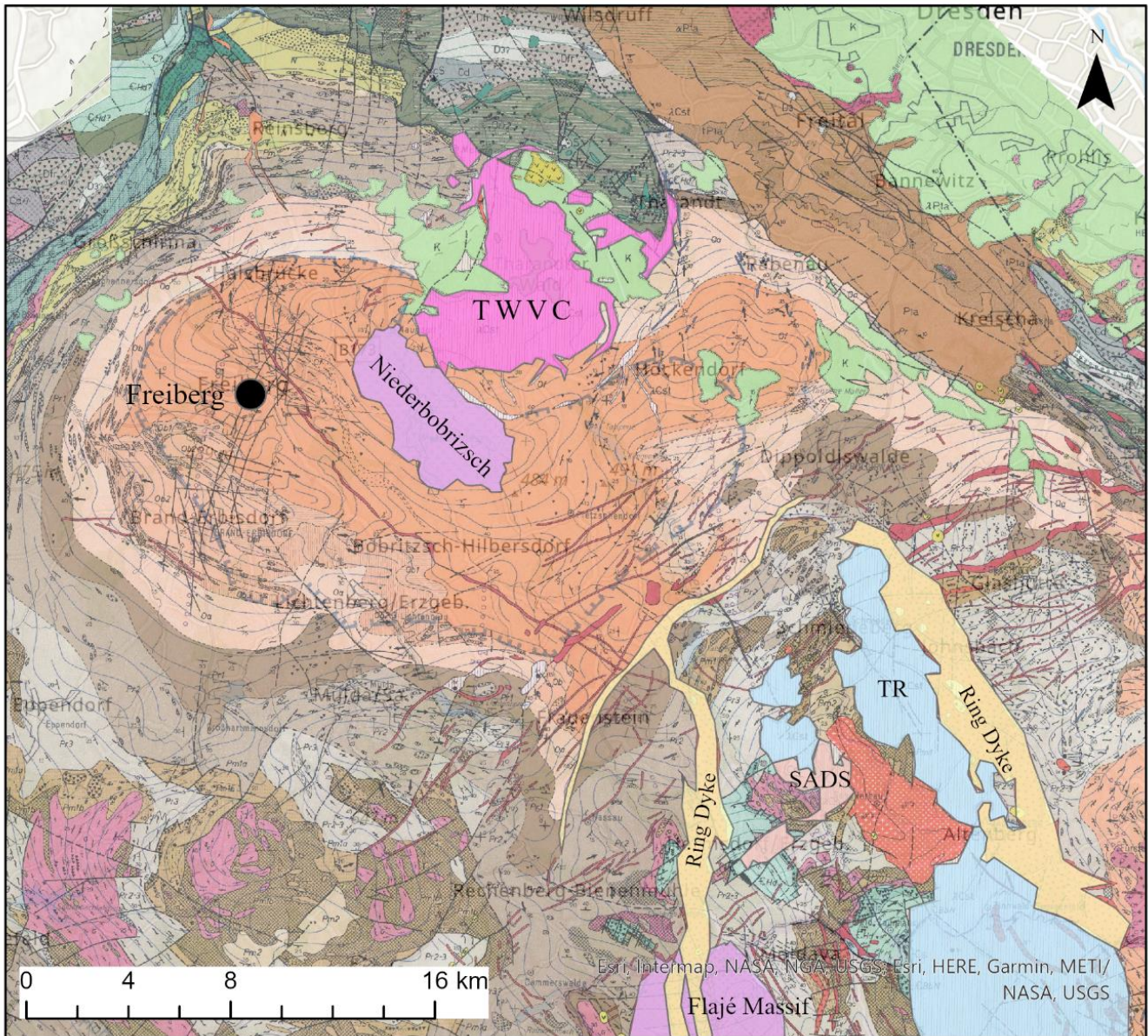


Figure 2: Geological map of the fieldwork area including polygons that indicate TWVC, Niederbobritzsch granite, TR, SADS, Flajé Massif and microgranitic ring dykes. Legend includes relevant units only. Map from Hoth et al. (1995).

3. Methods

3.1 Fieldwork and samples

For this study, 20 rock samples were taken for analysis during a fieldtrip to the Erzgebirge, around the city of Freiberg. This suit of samples includes dykes from the first and third generation of the SBDS and two dykes further to the north-west of the city of Freiberg that are not part of this swarm. At some outcrops, planes were measured in strike-dip orientation. Since the area is highly vegetated and the rhyolite dykes are poorly exposed, some samples were taken from floatstones (i.e. loose boulders of unknown provenance) and there was no opportunity for doing measurements on dyke extent and/or thickness. Two samples were selected from a PhD project by Li (1978) at the archive of the Geological Survey of Freiberg. The floatstone samples are normally incorporated in the dataset, unless there are strong petrological and/or chemical indications of deviation from the samples that were taken in situ.

3.2 Microscopy

From the whole suit of samples, polished thin sections were made at Utrecht University. All thin sections were digitalised with ZEISS Axioscan. Petrological and mineralogical characteristics were determined through optical microscopy using a Axio Scope with a color 305 Axiocam. Modal mineral abundances were determined by point counting in the open access JMicroVision software. For every sample, the dataset consists of a minimum of 1000 points. For six samples of the 20 samples, A JEOL Neoscope II JCM – 6000 table-top Scanning Electron Microscope (TTSEM) was used to identify accessory minerals. This was done at an acceleration voltage of 15 kV and a probe current of 1 nA. In preparation for the TTSEM analysis, thin sections were coated with a thin layer of evaporated carbon to induce conductivity and prevent build-up of electric charge.

3.3 Fourier-transform Infrared spectroscopy

In order to identify alteration and/or weathering features and rock forming minerals, analyses were performed using the Agilent portable 4300 Fourier-transform infrared spectroscopy (FTIR) sensor at TU Delft. Reflected light was measured and the spectral range was set from 4000 cm^{-1} to 650 cm^{-1} (Mid-Wave Infra-Red (MWIR) to Long-Wave Infra-Red (LWIR)) with a sample scanning rate of 64 and a calibration scanning rate of 128. The Background Valid time limit was set to 15.0 minutes. For optimal light reflectance, the FTIR instrument was used on the smooth surfaces of the cut edges of the rock samples.

Measured points were identified based on distinct features such as colour and shape (e.g. ‘white spot’, ‘red line’), with a focus on weathering characteristics. Spectral data smoothing was applied using 30 points window in order to avoid or minimize unwanted variation within the data and enhance the

signal pertaining to the analytical information. Interpretation of the IR spectra was conducted using reference spectra from different mineral libraries and published articles.

3.4 Portable X-ray Fluorescence

For better understanding of the mineralogical and geochemical composition of the analysed weathering features in the samples, a Thermo Scientific Niton XL5 Plus portable X-ray Fluorescence (pXRF) spectrometer was used on the same spots as the FTIR spectrometer to obtain corresponding geochemical data. The spot that is measured has a radius of about 8 mm and the instrument was used in the 'mining' mode for 20 seconds per measurement. The chemical data obtained from the pXRF is given in parts per million (ppm).

3.5 Whole rock geochemistry

For whole rock geochemical analysis, all samples were crushed using a steel hammer and then powdered in a tungsten carbide mill. The powdered samples were heated for the evaporation of organic compounds and volatiles in steps of 105 °C, 450 °C, 550 °C, 800 °C and 1000 °C by a TGA701, to measure the loss on ignition (LOI). The remaining powder was then used to make compositionally homogeneous glass fusion beads. These beads included 0.6 grams of the powdered sample (after TGA) and 6 grams of flux (ICPH, Fluomix 6515Lil) and were fused at 1200 °C. They were analysed for whole rock major elements by X-ray Fluorescence (XRF) at Utrecht University by a Perform'X 4200W spectrometer.

After executing the XRF analysis, the glass beads were crushed and small pieces were taken from every sample for the whole rock trace element analysis. The samples were analysed in triplicate at Utrecht University for their trace element content, by a ThermoFischer Scientific Element 2 magnetic sector Laser Ablation Inductively Coupled Plasma-Mass Spectrometer (ICP-MS) and a Lambda Physik excimer laser (193 nm) with GeoLas optics.

In both the XRF and ICP-MS analyses, four reference samples were analysed in order to assess the accuracy of the measurements. For a reference to samples with similar composition as the ones studied here, two rhyolitic samples (JR-1, JR-3) and one granitic sample (GRAN-1) were used. In addition, one soil reference sample (ISE-921) was used. For the error assessment and validation of the geochemical data, the results of the reference samples were compared to the GeoReM database. Also the results of the two samples from Li (1978) were compared to the data as obtained in 1978. For the triplicate ICP-MS measurements, the mean and the standard deviation (Stdev) were determined for every measured trace element in every sample, in order to quantify the relative standard deviation (%RSD).

4. Results

4.1 Field observations

Figure 3 and Table 1 show a geological map of the fieldwork area with the sampling sites and a list of the samples that were retrieved from the Freiberg district (Appendix 1). The suit of samples includes 13 in situ specimens (including the two samples from the archive of the geological survey of Freiberg) and seven samples from floatstones (loose boulders of unknown provenance). Most rocks were sampled from the SBDS, with an exception for in situ samples M05101 and M10101 (and possibly also floatstone samples M06101A+B and M05103) that were taken from the rhyolitic dykes further north-west of Freiberg.

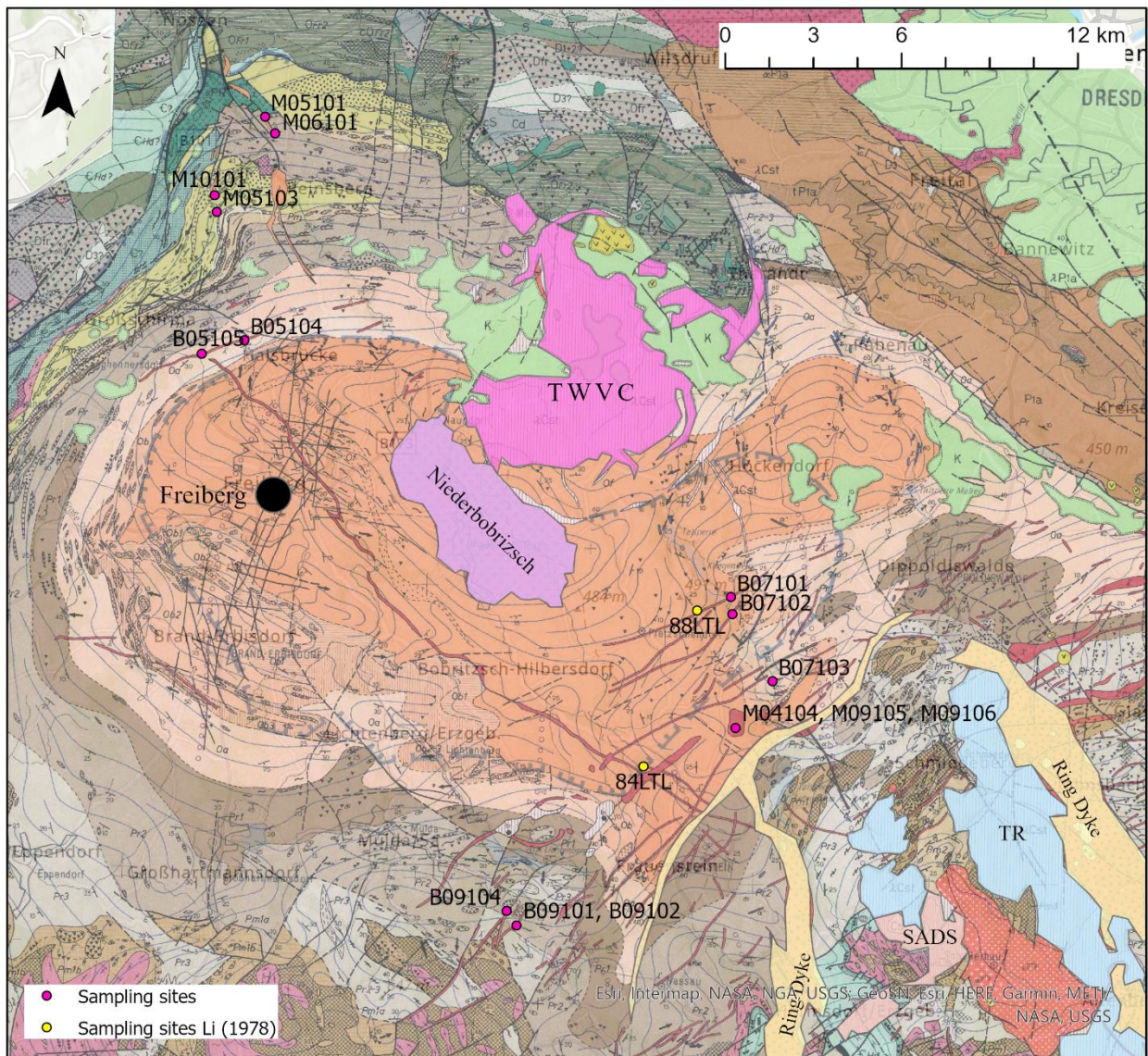


Figure 3: Geological map of the fieldwork area with sampling sites. Polygons represent same units as in Figure 2. Map from Hoth et al. (1995).

Table 1: List of samples analysed in this study. *Samples taken from Li (1978).

Sample No.	Location	Coördinates	Type	Preservation state	Generation
M04104A	Röthenbacher Berg	50.84312, 13.56519	In situ	highly weathered	1
M04104B	Röthenbacher Berg	50.84312, 13.56520	In situ	highly weathered	1
M05101	Drehfeld	51.02966, 13.33635	In situ	slightly weathered	N/A
M05103	Kleinvoigtsberg	51.000053, 13.314314	Floatstone	moderately weathered	unknown
B05104	Halsbrücke	50.576512, 13.195710	Floatstone	moderately weathered	unknown
B05105	Halsbrücke	50.573192, 13.184217	In situ	slightly weathered	3
M06101A	Muldenzacke	51.022942, 13.340558	Floatstone	highly weathered	unknown
M06101B	Muldenzacke	51.022942, 13.340558	Floatstone	moderately weathered	unknown
B07101A	Klingenberg	50.883749, 13.570003	Floatstone	slightly weathered	unknown
B07101B	Klingenberg	50.884726, 13.569471	Floatstone	highly weathered	unknown
B07102	Beerwalde	50.879800, 13.568166	In situ	slightly weathered	3
B07103	East Röthenbach	50.859671, 13.588220	In situ	slightly weathered	1
B09101	Dittersbach	50.782976, 13.466927	In situ	moderately weathered	3
B09102A	Dittersbach	50.782976, 13.466928	In situ	moderately weathered	3
B09104	Dittersbach	50.787108, 13.462865	Floatstone	highly weathered	unknown
M09105	Röthenbacher Berg	50.844125, 13.567106	In situ	slightly weathered	1
M09106	Röthenbacher Berg	50.843267, 13.567463	In situ	slightly weathered	1
M10101	Kleinvoigtsberg	51.003663, 13.312762	In situ	slightly weathered	N/A
84LTL*	South Friedersdorf	-	In situ	fresh	1
88LTL*	East Pretzschendorf	-	In situ	slightly weathered	1

Samples B09101 and M10101 were taken at outcrops where the rhyolite dykes show a flow foliation (Figure 4a, b). The orientation of this foliation is 088/58 N and 164/80 E respectively. Sample B09102A was taken about two meters north of B09101, from another outcrop that shows the contact between the rhyolite dyke and host gneiss (Figure 4c). The orientation of this contact is 048/74 SE and includes a 1 – 2 cm wide zone of gouge. For an overview of the field measurements see Appendix 2.





Figure 4: a, b) Outcrops that show foliation (foliation orientation indicated by red lines). Hammer and fieldbook for scale. c) Outcrop that shows the contact between the rhyolite dyke and the host gneiss. Hammer for scale.

Several samples (M04104A+B, M09105, M09106) were taken in the open pit mine at Röthenbacher Berg, which comprises a rhyolite dome rather than a dyke (Figure 3). Samples M04104A+B are from an outcrop at the entrance of the mine (Figure 5), that shows a ductally deformed contact zone between the rhyolite and the host gneiss. Here sample M04104B represents the direct contact with the host gneiss and sample M04104A was taken about a meter away from the contact.





Figure 5: Outcrop that shows the ductally deformed contact between the rhyolite (top) and the host gneiss (bottom) at the Röthenbacher mine. a) Overview of the outcrop with deformed contact indicated by the white line. Backpack for scale. b) Close-up of the contact. Hammer for scale.

4.2 Major mineralogy and alteration features

For all samples, the major mineralogy is similar and Table 2 shows the modal mineral abundances. The major minerals that constitute the rhyolites are quartz, K-feldspar, plagioclase, biotite, muscovite and opaque minerals. Almost all samples have a porphyritic texture, typical for volcanic rocks, and show signs of some degree of weathering/alteration. The main weathering/alteration features (Figure 6) are (partly) altered mica crystals, (partly) altered feldspar crystals, entirely recrystallized crystals, quartz veins, fractures with carbonate infill and holes in the section resulting from removal of crystals by weathering. These holes that are classified as weathering features are different from the extra feature class in sample M06101B. This rock contains many vesicles with irregular shapes that are presumed to be a primary feature. In almost all samples that contain (partly) recrystallized/altered phenocrysts, the recrystallization product consists (partly) of sericite (Figure 6f). In most of these samples, sericitization also significantly affected the matrix.

Table 2: Modal abundances of major minerals and weathering features. All weathering features (see text) were classified together. Values are given in %

Sample	Matrix	Quarz	K-Feldspar	Plagioclase	Mica	Weathering features	Hole in sample
M04104A	94.8	3.5	0.3	0.1	0	1.3	
M04104B	90.3	4.3	1.8	0.7	0	3.0	
M05101	78.3	10.0	5.4	0.2	1.1	5.0	
M05103	96.2	1.7	1.3	0	0	0.9	
B05104	89.7	2.3	2.6	0.8	0.1	4.6	
B05105	90.8	5.1	0.4	0.7	0	3.1	
M06101A	81.6	6.9	5.2	0	2.0	4.3	
M06101B	77.8	8.1	4.6	0	0	2.6	6.9
B07101A	38.9	16.6	17.0	21.0	0	6.6	
B07101B	99.3	0.1	0	0	0	0.6	
B07102	60.9	13.5	10.6	13.3	1.7	0.4	
B07103	29.1	15.2	11.8	8.4	3.8	31.8	
B09101	80.9	6.0	3.7	2.1	0	7.4	
B09102A	83.4	6.5	5.5	2.0	0.1	2.6	
B09104	84.7	10.4	0.8	0	0.1	4.0	
M09105	81.4	6.9	8.5	2.0	0.1	1.1	
M09106	79.0	7.8	7.9	2.9	0.1	2.3	
M10101	94.2	2.3	0.9	0.6	0	2.1	
84LTL	63.7	7.0	7.9	14.2	6.5	0.8	
88LTL	99.3	0.4	0	0	0	0.3	

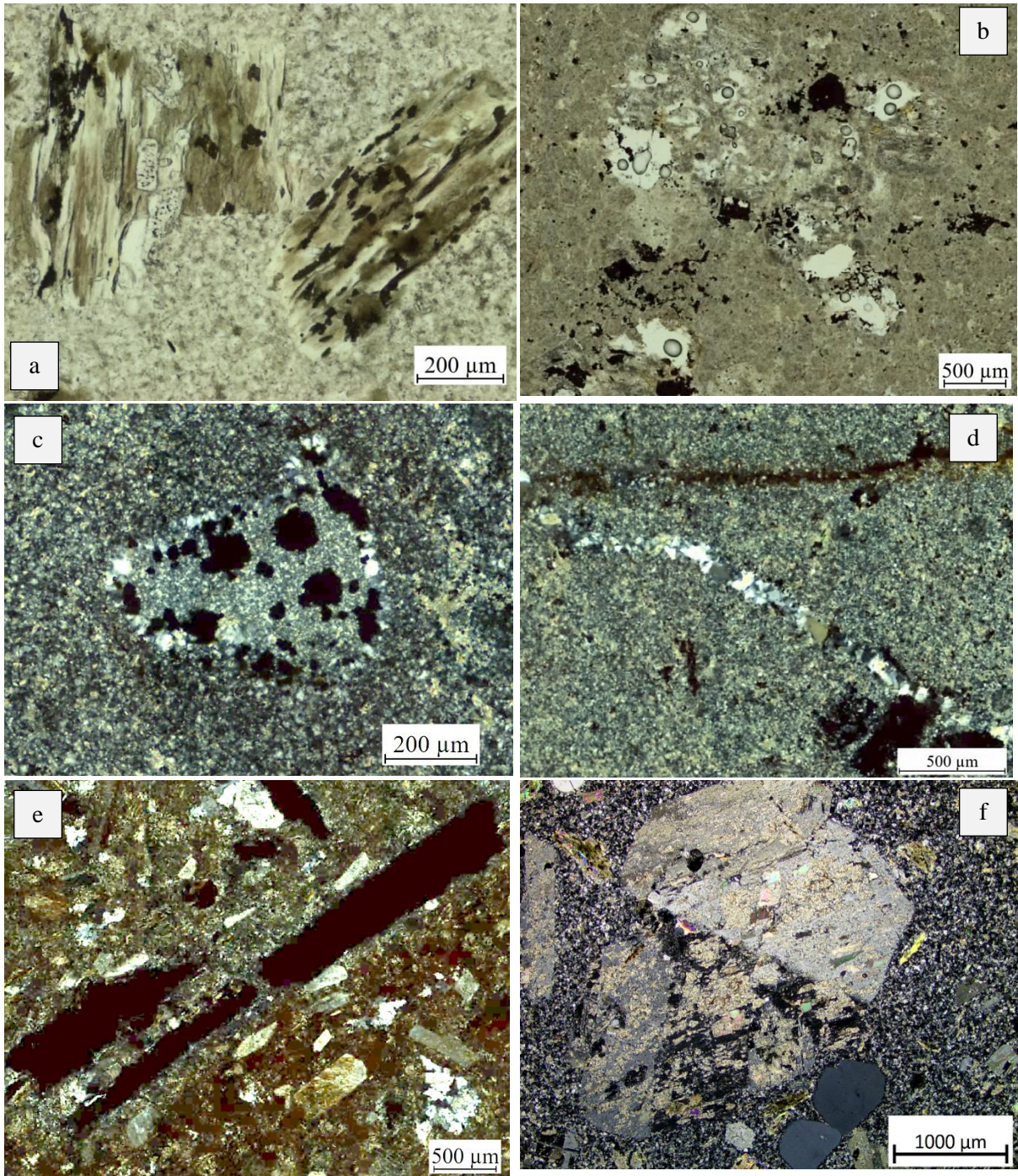


Figure 6: a) Weathered/altered muscovite crystals (PPL, 84LTL). b) Weathered feldspar crystals (PPL, B05105). c) Entirely recrystallized phenocryst (XPL, B05104). d) Quartz vein and fracture with carbonate infill (XPL, B05104). e) Hole in section as remnant of weathered crystal (PPL, B07103). f) Sericitized feldspar phenocryst (XPL, 84LTL).

4.3 FTIR spectroscopy and pXRF

As mentioned above some samples have a poor preservation state and thin sections show several alteration/weathering features. In this context, the spectral and point-geochemical data as obtained by FTIR spectroscopy and pXRF analysis could provide complementary results to the microscopic observations and could be used to further characterize possible weathering features in the rhyolite samples. With a focus on identifying weathering patterns, distinct points defined by characteristic features (e.g. colour and shape) were measured. Some of the IR spectra and the pXRF measurements that are representative for the whole dataset are described in the following section. However, spectral interpretation should be done with caution, since the spectrum that is obtained from the FTIR analysis can be mixed due to mineral co-occurrence. The total dataset of IR spectra and pXRF analyses are presented in Appendix 3.

Before looking into possible weathering features, it is important to identify the IR signals of the rock-forming minerals in the rhyolite samples. Figure 7 shows the IR spectrum of a ‘red spot’ on sample B09104. The two large reflectance peaks around 8.2 μm and 9 μm and the three smaller peaks around 4.6 μm , 12.5 μm and 12.8 μm make a strong resemblance with the reference spectra of quartz in Figure 8 and are therefore accounted to this mineral. These peaks are due to Si-O stretching. The corresponding pXRF data is plotted in Figure 9.

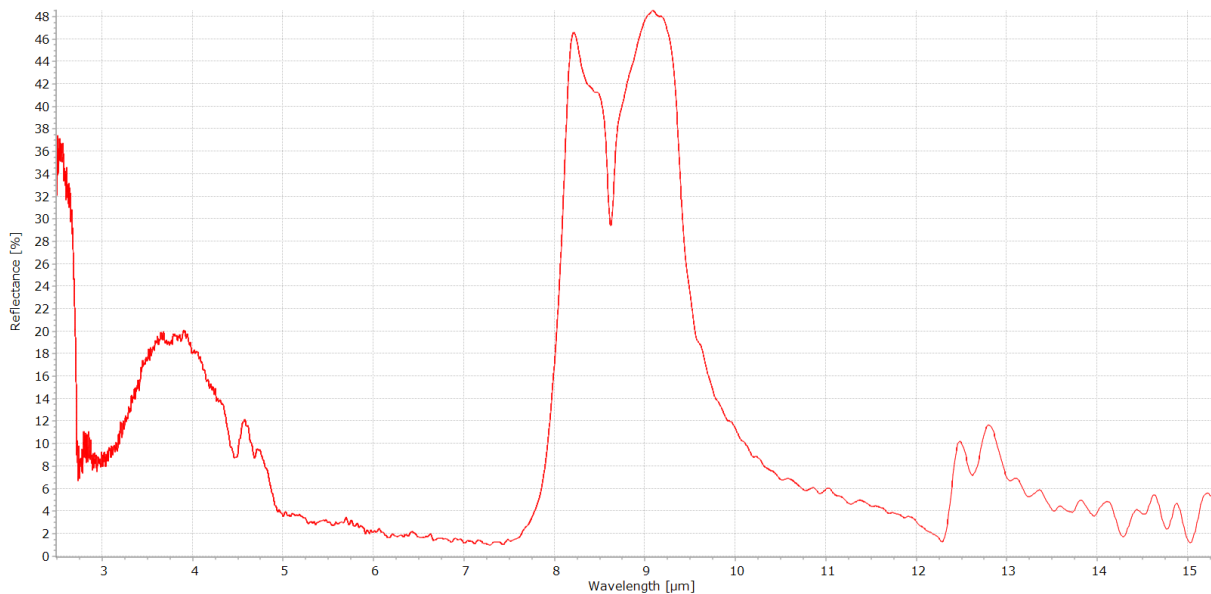


Figure 7: FTIR spectrum of a ‘red spot’ on sample B09104.

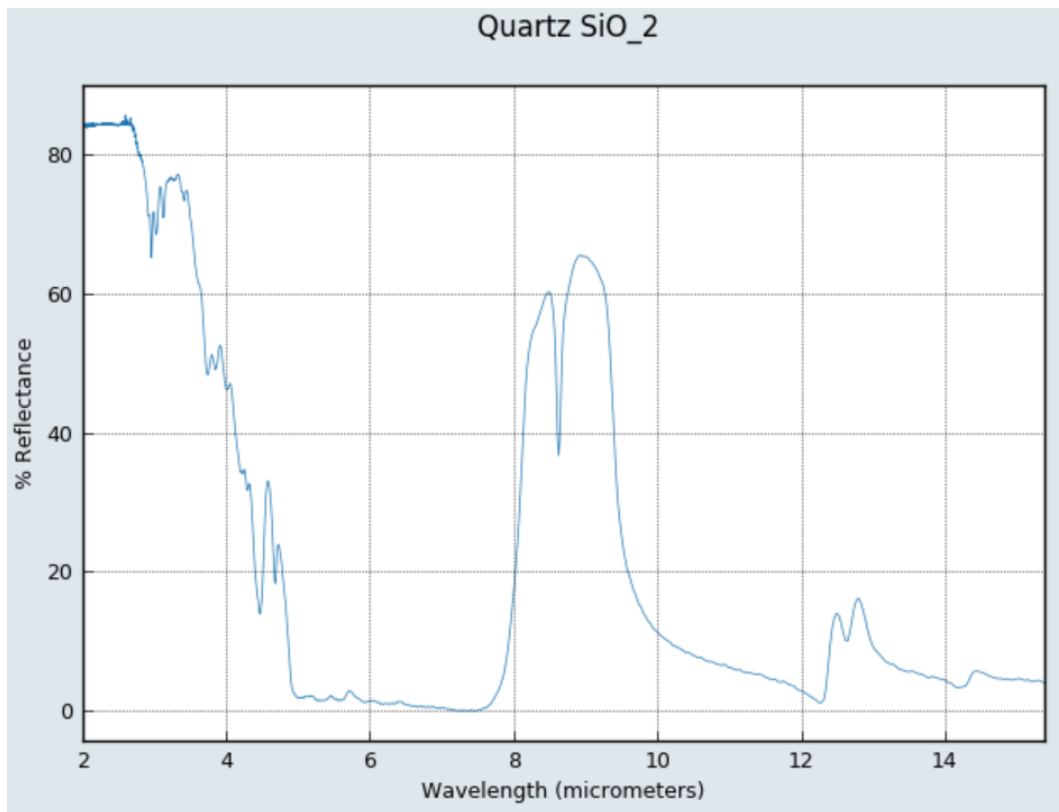


Figure 8: FTIR spectrum of quartz. From Baldridge et al. (2009), Meerdink et al. (2019).

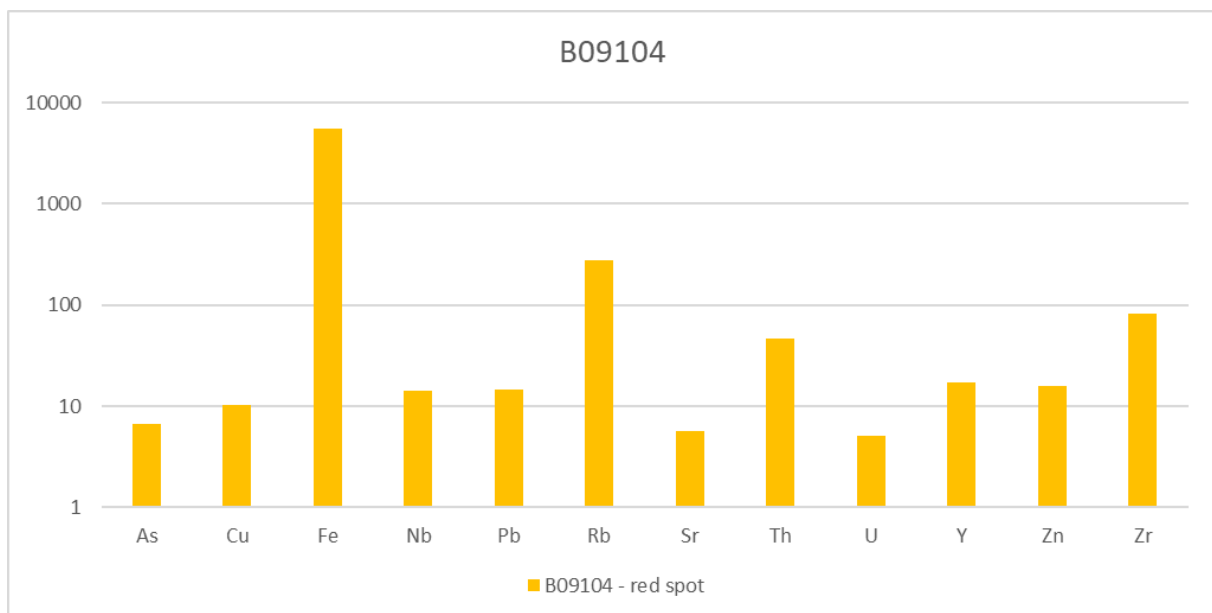


Figure 9: pXRF data of a 'red spot' on sample B09104. Values are given in ppm.

The IR spectrum that is shown in Figure 10 represents the signal of a 'dark spot' on sample B07102. In Figure 10a, the small spectral features around 13.7 μm could be caused by the Al-O-Si stretching vibration. The broad peak at about 9.7 μm likely indicates the presence of Si-O and/or Si(Al)-O stretching. The peak at about 8.9 μm indicates Si-O stretching. For comparison with the reference spectrum, the spectrum in Figure 10b is plotted in wavenumbers. Here, the broad, irregular reflectance

peak between about 8 μm ($\sim 1250\text{ cm}^{-1}$) and 10.5 μm ($\sim 9500\text{ cm}^{-1}$) resembles the broad, irregular peak around 1055 cm^{-1} ($= 9.5\text{ }\mu\text{m}$) in the orthoclase reference spectrum from Figure 11. Therefore these spectral features are (mainly) accounted to K-feldspar. The corresponding pXRF data is shown in Figure 12. The relatively high Rb concentration (that is featured in almost all pXRF measurements (Appendix 3)) may be linked to Rb commonly substituting for K in K-feldspar. Again, the pXRF data shows a high concentration of Fe.

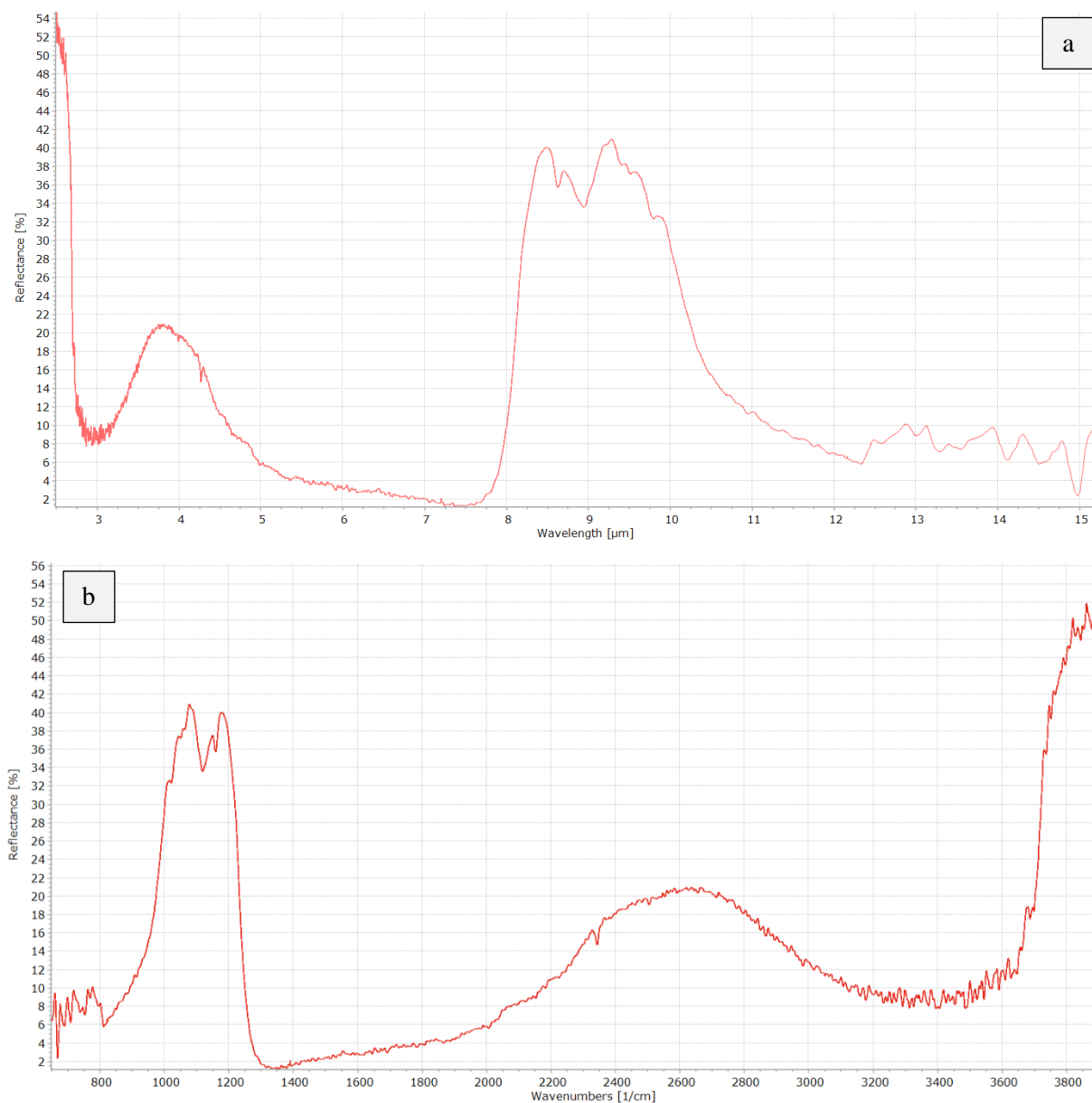


Figure 10: a) FTIR spectrum of a 'dark spot' on sample B07102 in wavelength (μm). b) Same spectrum as in Figure 10a but here plotted in wavenumber (cm^{-1}) on the x-axis.

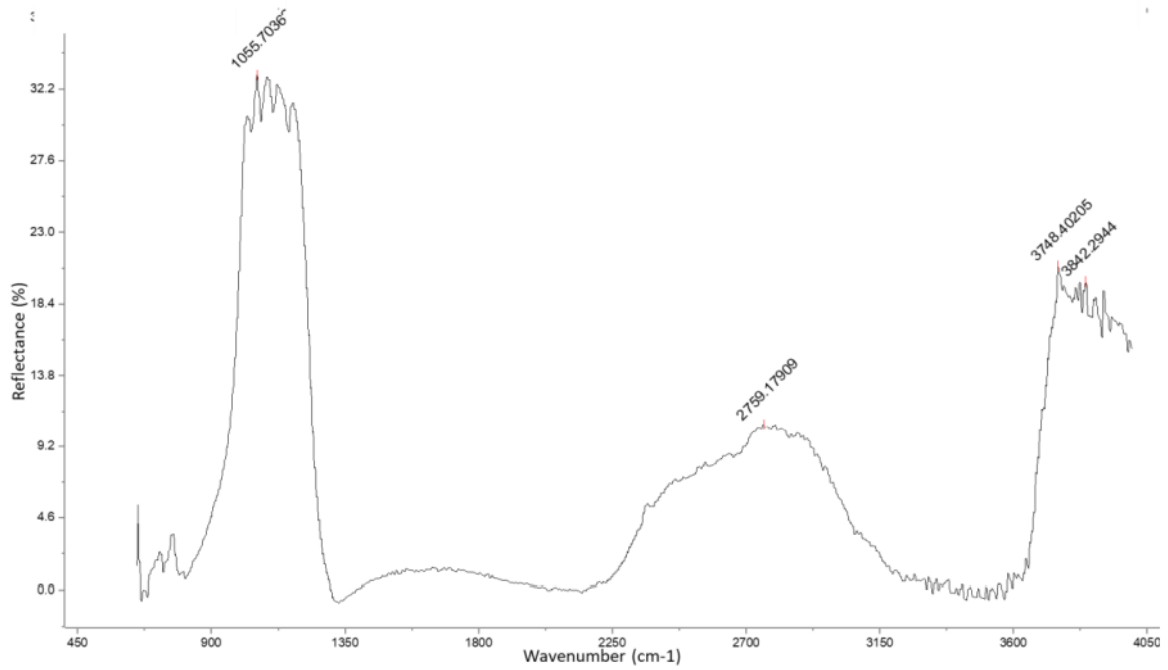


Figure 11: FTIR spectrum of orthoclase. From Gatti (2022).

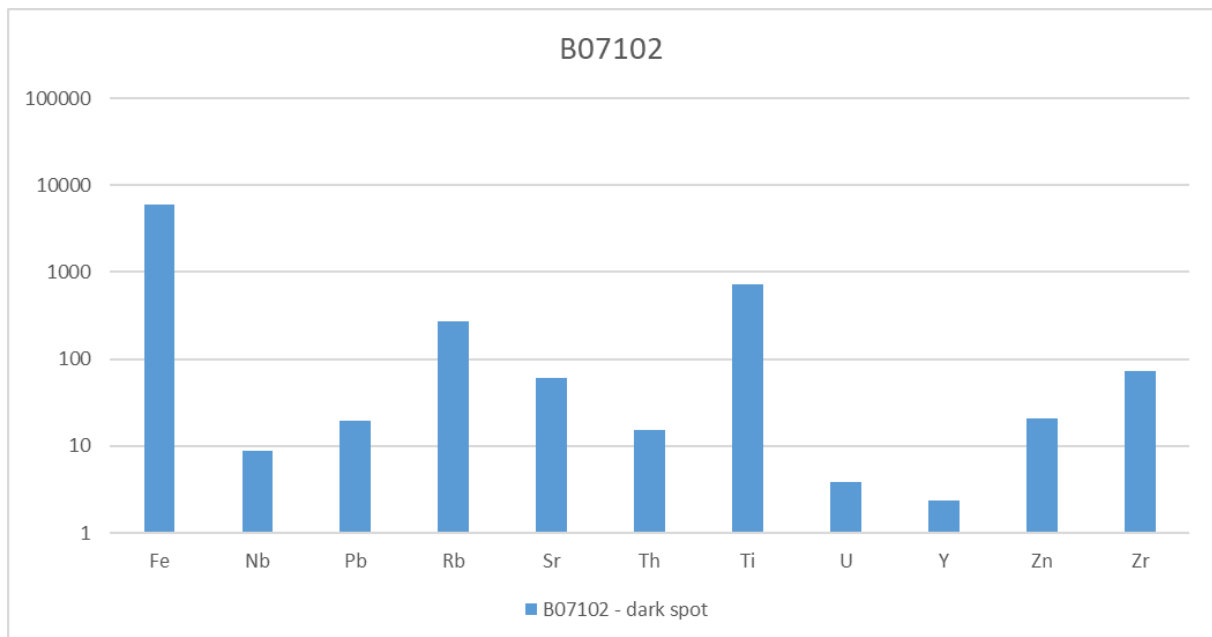


Figure 12: pXRF data of a 'dark spot' on sample B07102. Values are given in ppm.

In Figure 13, the IR spectrum of a 'white spot' in sample B07103 is shown. In Figure 13a, the four peaks at about 8.4 μm , 8.7 μm , 9.6 μm and 9.9 μm correspond to the four main peaks shown in Figure 13b. These features make a resemblance with the plagioclase reference spectrum from Figure 14 that includes similar shaped peaks around 910 cm^{-1} (= 10.9 μm), 1100 cm^{-1} (= 9.1 μm) and 1120 cm^{-1} (= 8.9 μm) for anorthite and around 1000 cm^{-1} (= 10 μm), 1100 cm^{-1} (= 9.1 μm) and 1150 cm^{-1} (= 8.7 μm) for albite. Therefore, this spectrum is (mainly) accounted to plagioclase.. The corresponding pXRF data to the 'white spot' on sample B07103 is given in Figure 15.

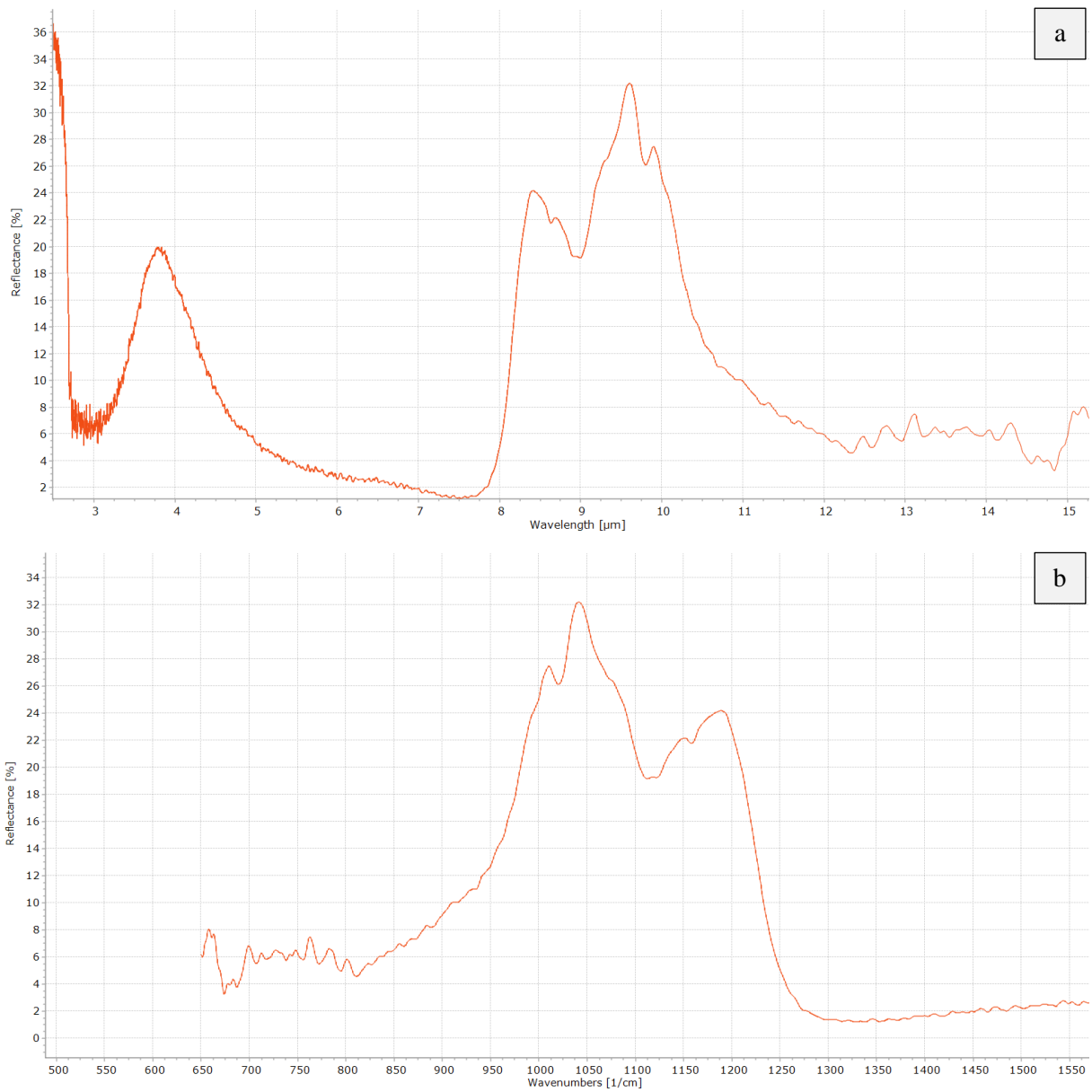


Figure 13: a) FTIR spectrum of a 'white spot' on sample B07103 in wavelength (μm). b) Same spectrum as in Figure 13a but here plotted in wavenumber (cm^{-1}) on the x-axis.

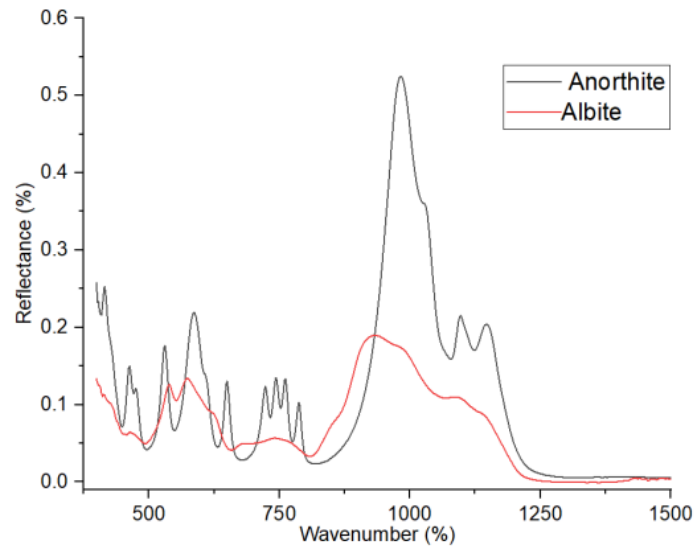


Figure 14: FTIR spectra of albite and anorthite. From Lafuente (2015). Note: the wavenumber on the x-axis is given in cm^{-1} , not %.

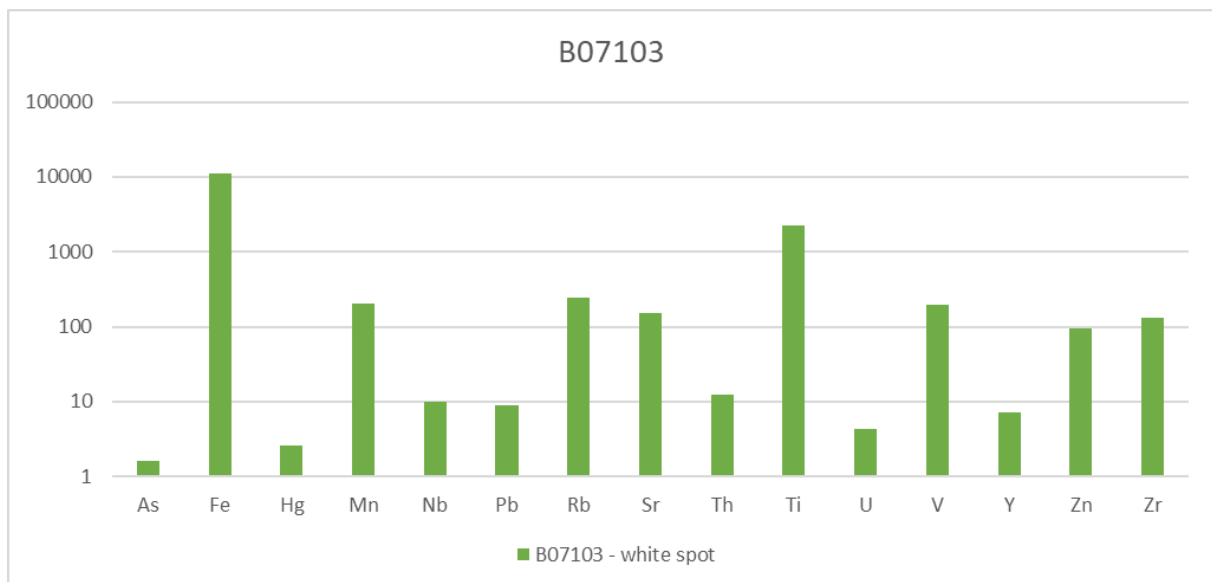


Figure 15: pXRF data of a 'white spot' on sample B07103. Values are given in ppm.

In addition to the signals in the IR data that are linked to the rock forming minerals, as described above, there are also other features in the FTIR spectra that have not been addressed yet and may be accounted to weathering and/or alteration products.

Figure 16 shows the IR spectrum of a 'red spot' on sample B07101B. Here, the most prominent reflectance peak lies around $4 \mu m$, with a smaller peak around $6.5 \mu m$.

These peaks are represented in the IR spectrum of almost every sample (Appendix 3) and do not correspond to any of the rock forming minerals as described above. Instead, another phase could cause these spectral features, as is also suggested by the pXRF data. The pXRF data of the 'red spot' in sample B07101B is given in Figure 17, and shows that the analysed spot contains a large

concentration of iron. This large iron concentration is also featured in the pXRF of almost all other samples (Appendix 3). Iron-oxide minerals are common weathering products of other Fe-bearing minerals and could therefore be the cause of the abundant spectral features as described above (Blake et al., 1966). In addition, the red colour that was often used in this study to characterize the measured points during spectral analysis of the samples and is a common feature in the rock samples is typical for Fe and could therefore also be linked to the presence of iron-oxides (Appendix 3). In the pXRF data, also the relatively high Ti concentrations could be a result of iron-oxide weathering products, since Ti is a common element in iron-oxide minerals (such as ilmenite (FeTiO_3), Ti-magnetite ($(\text{Fe,Ti})_2\text{O}_4$) and Ti-hematite ($(\text{Fe,Ti})_2\text{O}_3$)).

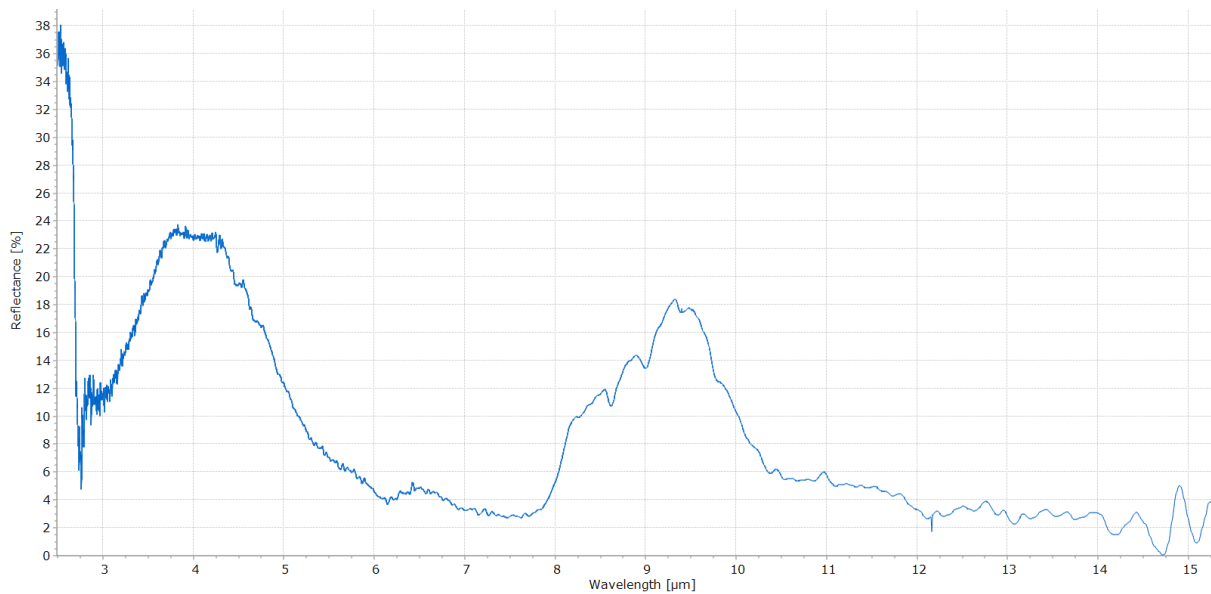


Figure 16: FTIR spectrum of a 'red spot' on sample B07101B.

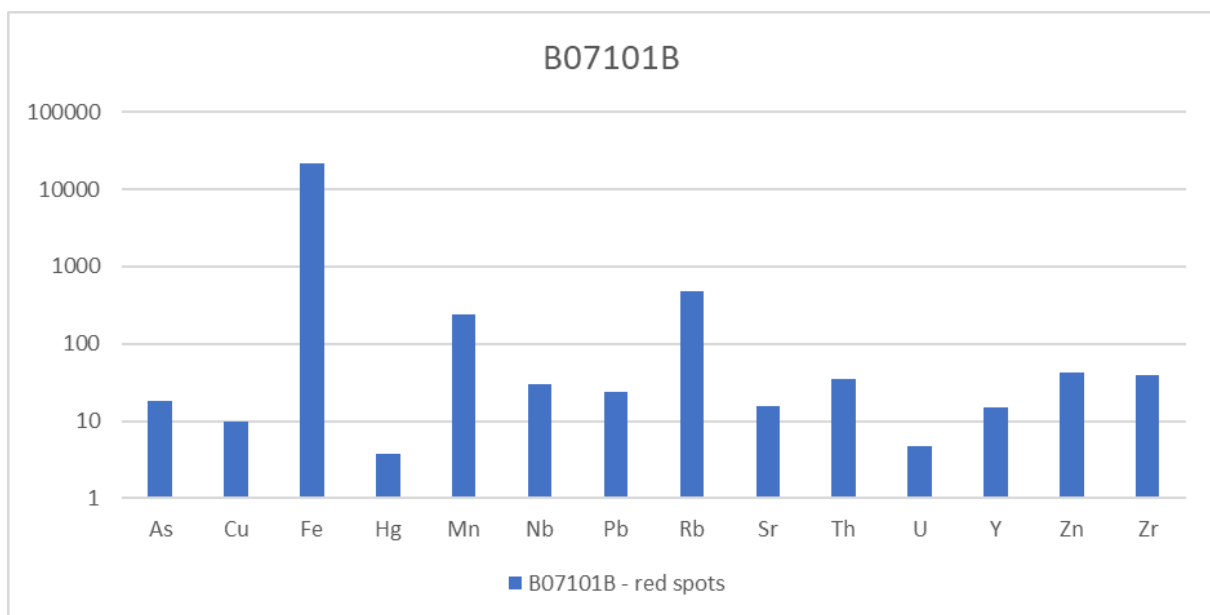


Figure 17: pXRF data of a 'red spot' on sample B07101B. Values are given in ppm.

The spectrum as shown in Figure 18 is from sample 84LTL. This spectrum, representing a 'yellow spot' on the rock, includes two strong peaks in the shorter wavelength area at about 3.7 μm and 4.2 μm (Figure 18b). The carbonate reference spectrum from Figure 19, with very similar reflection peaks around 3.7 μm and 4.2 μm strongly resembles the spectrum from sample 84LTL. Also the peak at about 6.4 μm in Figure 18a, can be linked to the carbonate spectrum wherein carbonate ions cause a reflectance band between 6 μm and 8 μm (Lesaignoux et al., 2013). The corresponding pXRF data for sample 84LTL is shown in Figure 20. In contrast to iron-oxides, for the presence of carbonate minerals, no clear indication is observed in the pXRF data to validate the spectral features. However, in addition to the strong resemblance of the spectrum of sample 84LTL with the reference spectrum of carbonate, also the yellow colour of the analysed weathering features could be linked to the presence of this mineral. In addition, like described above, carbonate features were identified in some thin sections. Overall, carbonates are thus likely a common weathering product in the sample set, which could also be reflected in the IR data.

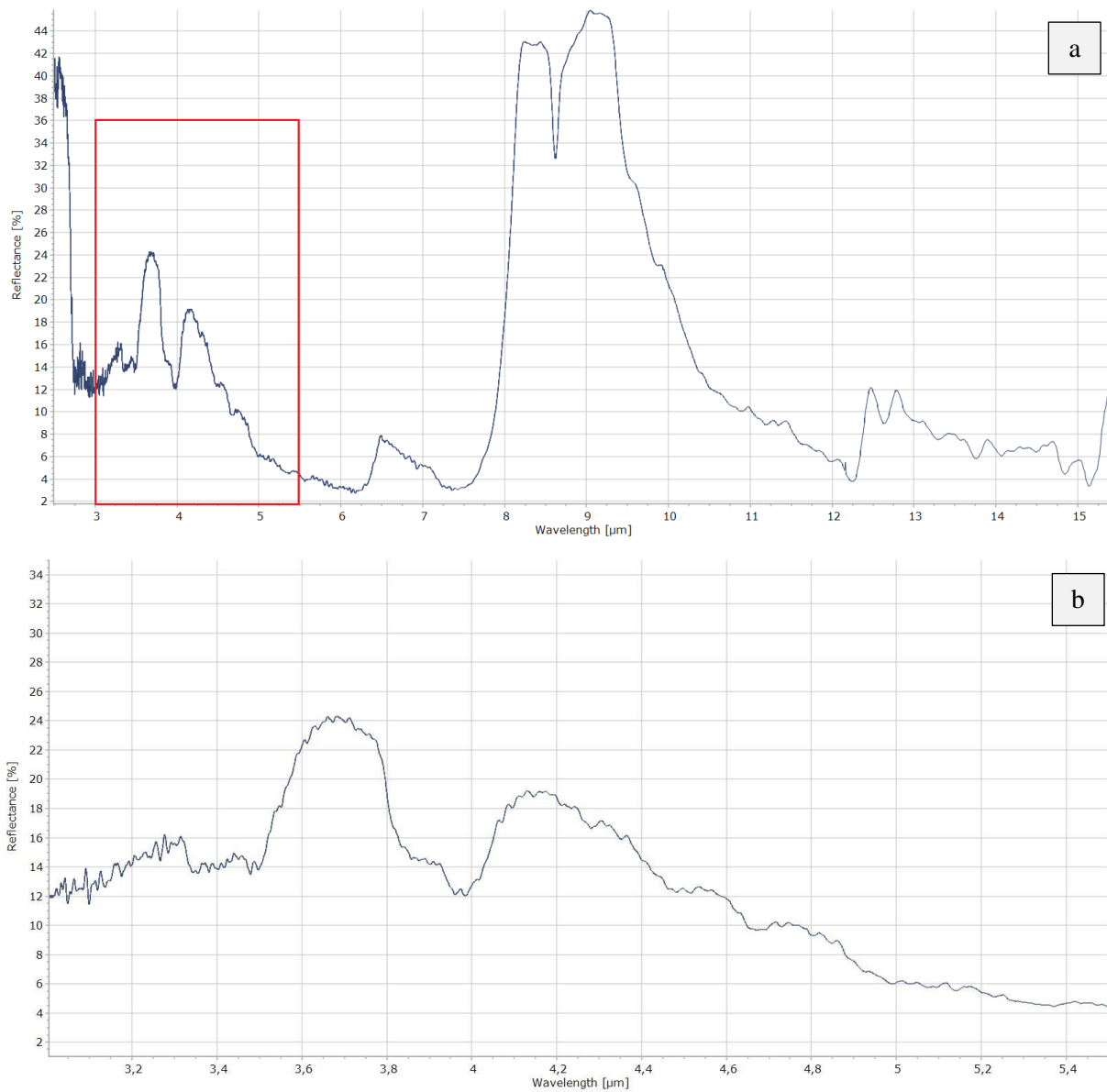


Figure 18: a) FTIR spectrum of a 'yellow spot' on sample 84LTL. Red square indicates axes range that represents Figure 18b. b) FTIR spectrum of a 'yellow spot' on sample 84LTL.

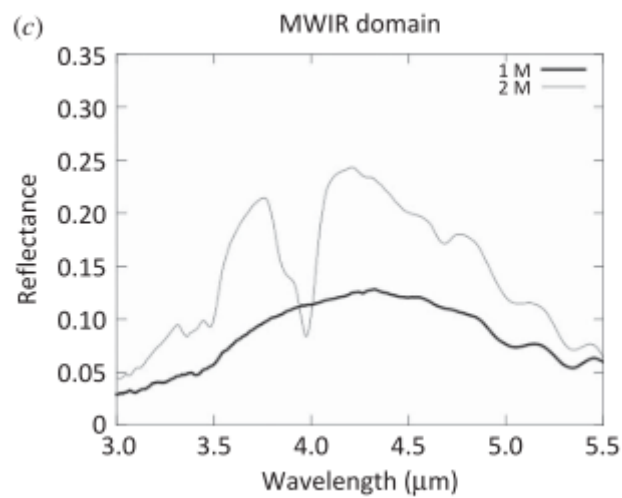


Figure 19: MWIR spectra of carbonate ions. From Lesaignoux et al. (2013).

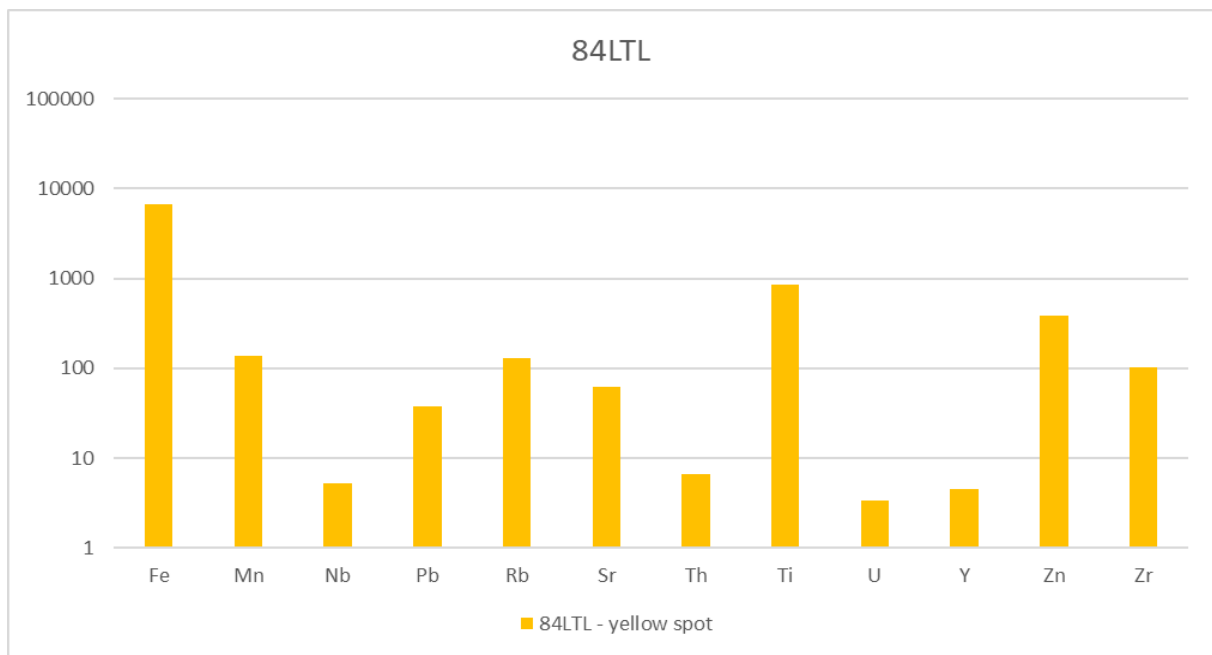


Figure 20: pXRF data of a 'yellow spot' on sample 84LTL. Values are given in ppm.

In the context of IR spectra and FTIR data, it is important keep in mind that the spectra of different minerals can strongly overlap. Therefore, the spectra that are obtained from the FTIR measurements can represent a combination of different minerals. Also, the interpretation of minerals using infrared spectra are sometimes challenging for different reasons, such as the co-occurrence of minerals, environmental influences (e.g., moisture) and a weak spectral response from some of the minerals. When using the pXRF data to validate the IR spectra, it should be kept in mind that the analysing beam of the pXRF instrument has a significantly larger radius (8 mm) than the beam of the FTIR spectrometer (2 mm), yielding a slight offset between the two datasets.

4.4 Petrology

Table 2 shows that the samples consist mainly of matrix (< 60%), with two exceptions in samples B07101A (38.86%) and B07103 (29.11%). Sample B07103 is strongly weathered and therefore a relatively large part of the section is classified as ‘weathering features’. This gives a distorted view of the distribution of the other classes in the rock. However, specimen B07101A resembles a microgranite more than a rhyolite and almost includes a phaneritic texture (Figure 21a). This sample also includes feldspar crystals that seem to feature an anti-rapakivi-like texture, with a rounded plagioclase core and an overgrowth of a mineral that resembles K-feldspar (Figure 21b).

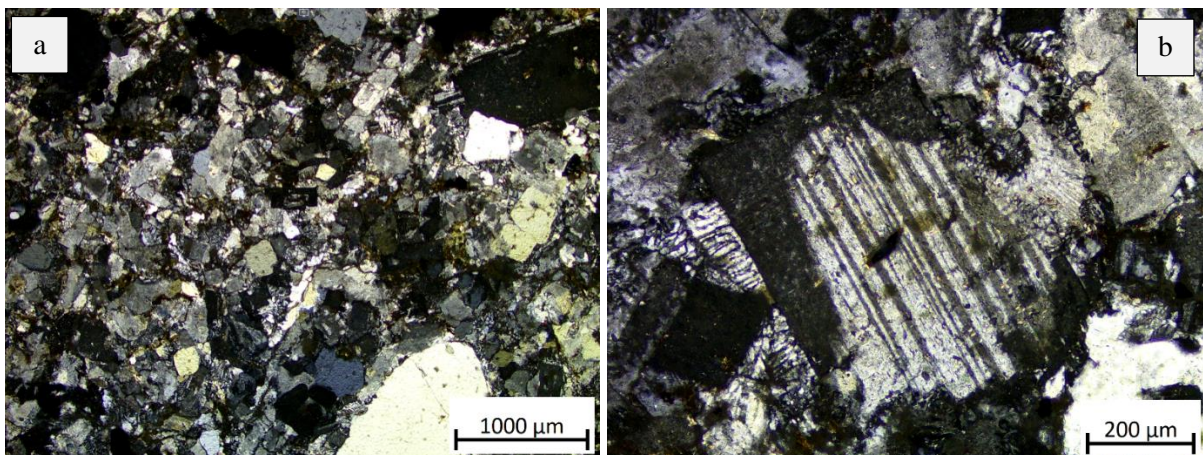


Figure 21: Sample B07101A (XPL). a) Phaneritic texture. b) Anti-rapakivi-like texture in feldspar crystal.

In the majority of the samples, the matrix consists of devitrified glass with a yellow to red or pale green colour and sometimes with a patchy appearance (Figure 22a). In some thin sections, the matrix shows a foliation texture. For example, in sample M04104B this foliation consists of alternating bands of different grain size and in sample M06101A a foliation can be observed in bands of small opaque minerals (Figure 22b). In the both sections, the foliation bends around the phenocrysts. In other sections, such as for sample B07103, the phenocrysts have a preferred orientation that defines a foliation texture (Figure 22c). However, the rocks that were collected at an outcrop that shows foliation on macroscopic scale (samples B09101 and M10101) do not show any clear foliation texture on microscopic scale.

The rhyolites contain abundant quartz phenocrysts that very often have a rounded shape with embayments and a small alteration halo/reaction rim (Figure 22d). K-feldspar often shows exsolution and samples M05101 and M06101A include zoned K-feldspar and/or plagioclase (Figure 22e). Glomerocrysts are a common feature in the rocks, sometimes with a granophyric texture (Figure 22f). In samples M04104A+B, this granophyric texture is combined with a sieve texture in the feldspar crystals that have intergrown with quartz. In these rocks, the sieve texture is also observed in other, solitary feldspar phenocrysts, that show a dendritic texture (Figure 22g). The sieve texture is also featured in feldspar crystals from samples M06101A and B09104.

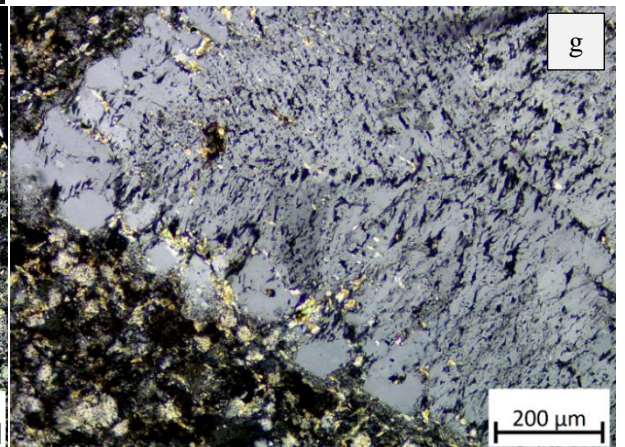
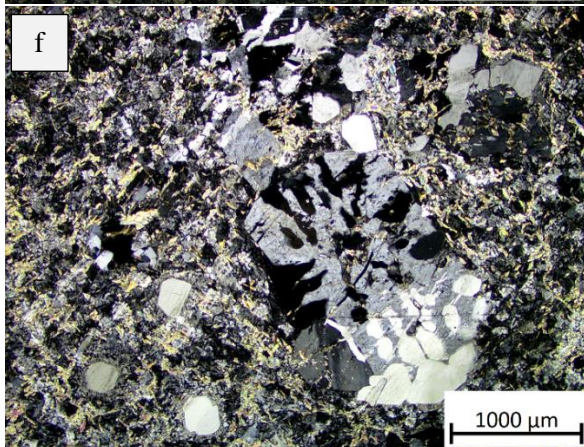
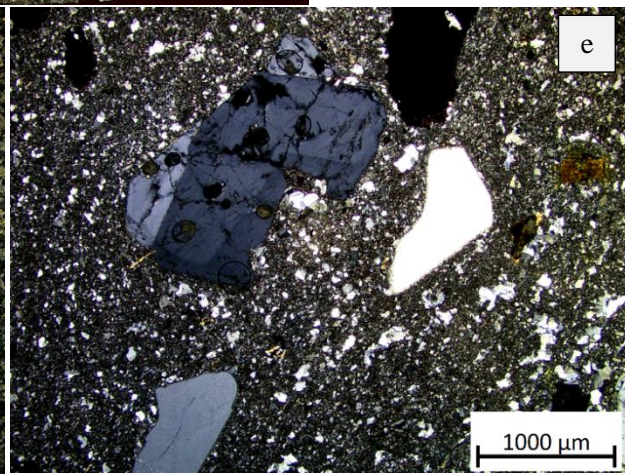
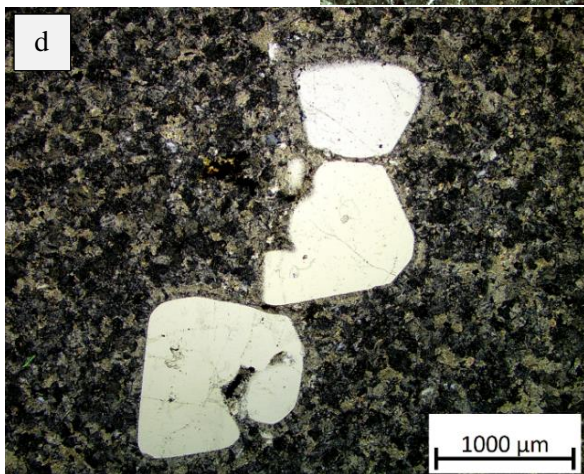
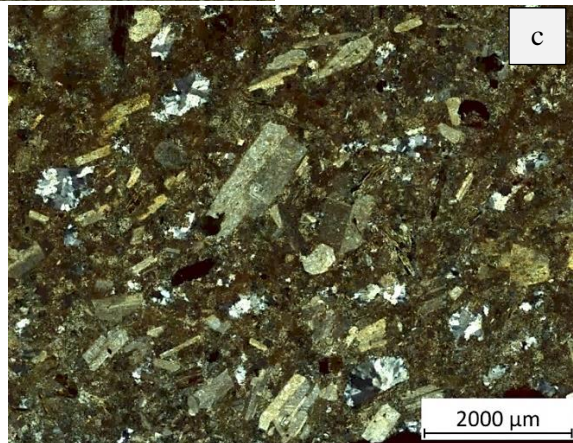
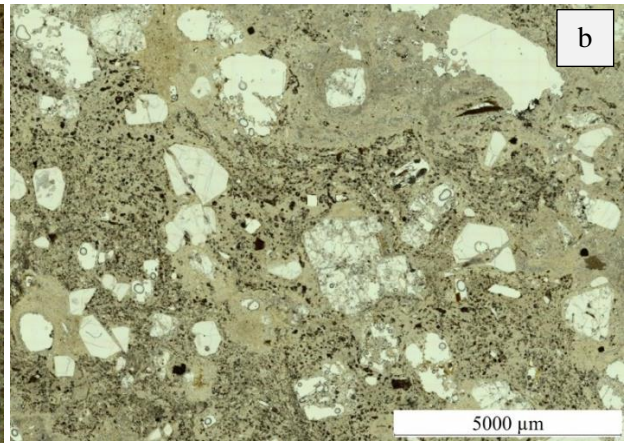
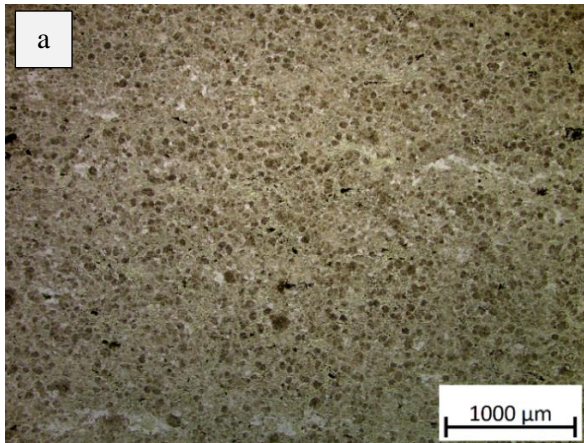


Figure 22 (previous page): Main textural features in the samples. a) Devitrified glass matrix with patchy appearance (PPL, B07101B). b) Banded and bend foliation in matrix (PPL, M06101A). c) Preferred orientation in phenocrysts (PPL, B07103). d) Resorbed and embayed quartz phenocrysts (XPL, B05105). e) Zoned K-feldspar (XPL, M05101). f) Glomerocryst with a granophyric texture (XPL, B09101). g) Feldspar phenocryst with a dendritic and sieve texture (XPL, M04104A). For an overview of all petrological features in the samples, see Appendix 4.

4.5 Textures linked to dyke emplacement

The flow banding that was identified on a macroscopic scale in the field and on a microscopic scale in some thin sections, is linked to the preferred orientation of the larger, elongate phenocrysts in some sections that is also caused by flow dynamics. This flow foliation was also identified by Freymark et al. (2015) for the FF-dyke, who measured the orientation of the long axis of phenocrysts in samples and drill cores from two localities along the dyke and determined a flow direction from SE to NW. This indicates that the source magma for the dykes was located somewhere south-east of the SBDS and that the dyke intrusion propagated north-westward. However, the FF-dyke has a more or less perpendicular orientation to the other dykes of the SBDS that were sampled in this study. It is therefore unfortunate that the oriented samples do not show any foliation on microscopic scale that could include shear sense indicators. This precludes the possibility of determining a flow direction for dykes of the SBDS that are differently orientated to the FF-dyke. Also for the dykes from the north-western system, a flow direction could not be determined.

The granophyric texture, which is also common in the rhyolite dykes, is another petrological feature that is linked to dyke emplacement. According to Morgan & London (2012), a granophyric intergrowth of quartz and/or feldspar is caused by undercooling of the melt. There are many different settings in which undercooling can occur and these textures can be formed, and textural characteristics are mainly influenced by diffusional control (Morgan & London, 2012). Since the rhyolite dykes comprise narrow bodies of viscous magma, undercooling and thus the occurrence of a granophyric texture could be expected, especially at the rim of the dykes.

Also the grain size of the matrix in the rocks is linked to magma cooling. Samples B09101 and B09102A, that are taken from a dykes interior and exterior respectively, are chemically and petrologically very similar. However, sample B09101 does include a slightly coarser grained matrix. This is likely due to a difference in cooling rate which decreases inwards from the dykes exterior. Freymark et al. (2015) also identified this effect for the FF-dyke.

4.6 Accessory mineralogy

In five samples (M05101, M06101A, B07102, B07103, 84LTL), accessory minerals were recognised through optical microscopy and chemically identified and analysed through a TTSEM. Results are given in Appendix 5. Note that these results should be treated qualitatively rather than quantitatively. For sample M10101 the TTSEM analysis only yielded data for an iron-oxide (Fe_2O_3) crystal, likely hematite (Fe_2O_3) or magnetite (Fe_2O_4), so no accessory minerals were measured. Also in samples M05101 and B07103, iron-oxide crystals were identified.

Samples M05101, M06101A, B07102 and B07103 all contain minerals that mainly consist of TiO_2 . In most samples these minerals form mica inclusions (Figure 23a), but sample B07103 also contains larger, individual crystals with a skeletal texture (Figure 23b). The opaque inclusions, such as in sample M05101 are most likely rutile (TiO_2) crystals. However, the larger skeletal crystals in sample B07103 are transparent in PPL and contain significant SiO_2 . Therefore, these are identified as titanite ($\text{CaTi}(\text{SiO}_4)\text{O}$).

Electron microscopy also shows that samples M06101A, B07103 and 84LTL all include accessory minerals that contain ZrO_2 and SiO_2 as main constituents. Based on their chemical composition and the typical prismatic shape and concentric zoning pattern of some crystals (Figures 23c, d), these are classified as zircons ($\text{Zr}(\text{SiO}_4)$).



Figure 23: Back-scattered electron (BSE) images of samples analysed under the TTSEM. a) Sample M05101: Iron-oxide inclusions in biotite crystal. b) Sample B07103: Skeletal titanite crystal with zircon inclusions. c) Sample M06101A: Zircon inclusions in biotite crystal. d) Sample 84LTL: Zircon crystal with concentric zoning pattern.

Table 3: Whole-rock geochemical data of the samples analysed for this study. Major oxides and Loss On Ignition (LOI) are in wt%, trace elements are in ppm. The SUM shows to total of the wt% oxides and is given in %.

Element	M04104A	M04104B	M05101	M05103	B05104	B05105	M06101A	M06101B	B07101A	B07101B	B07102	B07103	B09101	B09102A	B09104	M09105	M09106	M10101	S4LTL	S8LTL
Al ₂ O ₃	13.08	14.07	10.23	12.13	11.40	12.24	10.74	10.51	13.23	13.07	13.83	14.74	12.86	12.35	11.59	12.58	12.36	10.21	14.81	12.72
CaO	0.10	0.13	0.09	0.07	0.05	0.04	0.07	0.07	0.24	0.05	0.35	0.36	0.09	0.17	0.04	0.14	0.26	0.07	1.81	0.04
Fe ₂ O ₃	1.43	3.14	1.69	0.03	1.05	1.06	1.67	-0.08	0.50	0.83	1.07	2.26	0.40	0.69	0.97	1.25	1.07	0.34	1.95	1.83
K ₂ O	5.60	7.52	7.32	10.25	5.84	6.50	7.65	8.12	7.15	6.53	6.60	6.04	5.75	5.42	3.71	5.51	5.61	6.22	4.28	5.78
MgO	0.23	0.41	0.20	0.05	0.30	0.25	0.15	0.05	0.11	0.25	0.22	0.83	0.06	0.10	0.26	0.09	0.08	0.03	0.83	0.14
MnO	0.01	0.02	0.02	0.00	0.03	0.02	0.01	0.00	0.01	0.02	0.02	0.04	0.02	0.02	0.01	0.01	0.01	0.01	0.04	0.03
Na ₂ O	0.11	0.34	0.47	0.31	0.02	0.04	0.23	0.24	2.37	0.08	3.08	3.10	2.32	2.63	-0.02	2.53	2.54	0.51	2.66	0.04
P ₂ O ₅	0.00	0.01	0.04	0.00	0.01	0.01	0.01	0.02	0.16	0.00	0.21	0.14	0.00	0.00	0.00	0	0	0	0.13	0
SiO ₂	78.61	73.21	78.67	76.55	80.39	78.91	78.47	79.98	74.35	78.45	73.23	70.67	77.47	77.72	82.52	77.07	77.04	81.9	71.92	78.42
TiO ₂	0.02	0.03	0.16	0.06	0.04	0.05	0.13	0.14	0.19	0.03	0.19	0.39	0.01	0.01	0.03	0.03	0.03	0.04	0.31	0.03
SUM	100.68	100.27	100.38	100.90	100.66	100.62	100.62	100.57	99.72	100.80	100.19	99.91	100.45	100.59	100.68	100.67	100.46	100.89	100.11	100.52
LOI	2.015	1.861	0.877	0.654	1.466	1.277	1.205	0.963	0.967	1.405	0.807	1.459	0.831	0.707	1.701	0.78	0.717	1.606	2.826	1.573
Sc	7.9	9.7	6.1	6.4	7.7	7.4	3.9	4.0	5.3	7.3	4.7	6.3	6.3	6.2	6.9	5.1	5.6	5.2	6.9	7.2
Ti	236.8	303.2	1230.7	474.3	414.2	451.2	1111.6	1109.4	1446.9	316.2	1490.4	2924.9	171.7	171.1	331.4	358.7	335.9	335.4	2257.0	310.1
V	8.5	15.9	16.5	4.71	6.1	4.6	16	14	13	3.2	14	33	4.0	4	5.8	2.9	3.6	3.5	29.2	3.6
Cr	36	36	42	131.9	43	33	37	40	34	30	37	43	32	34	47.1	68.17	32	21.35	43	49.4
Mn	99	181	144	50.78	224	180	119	51	67	216	139	357	200	150	97	124	87	69	338	210
Co	22.9	23.8	42.6	17.63	28.5	33.6	41	40	32	17	22	124	30	42	30	30	21	29	20	30
Ni	20	20	19.3	10.8	22	8.7	11	11	31.98	9	11	16	11	12	14	27.1	11.9	33.4	15.1	52.8
Cu	12.4	20.3	20.9	15.943	7.1	5.3	10	11	114.2	11	8.4	4.3	417.4	11	27	32.29	11.7	5.9	4.2	16
Zn	79	102	41.1	39.5	54	40	34	41	67	64.9	50	108	48	37	30	89.6	65.7	23.7	631	24
Ga	26.4	37.7	45.9	20.5	21.0	23	18	19	30	23	27	40	28	27	21	27	29	12	29	19
As	7.5	20.3	86.3	7.3	46.9	14	71.7	133	5.0	16	3.4	5.0	46.3	25	39	40.99	15.4	60.15	5.03	14
Rb	446	674	409	642	424	521.5	402	424	410	606	356	258	610	560	327	460	480	405	209	458
Sr	21.5	30.7	94.2	18	60.1	25.5	84	88	103	20	90	162	51	53	8.0	17	15.7	26	162	17
Y	48	64	17	13	30	37	9	12	14	27	15	17	71	52	29	39	50	9.4	15	32
Zr	94	129	105	78.8	86	93	93	89	109	58	113	173	93	100	90	107	99	54	130	62
Nb	26	27	14	29	32	33	14	13	15	25	15	13	30	39	17	23	23	22	8.3	27
Mo	1.8	2.0	2.6	2.87	2.1	1.47	1.4	2.0	1.5	1.8	1.6	1.7	1.6	2.27	2.84	4.54	1.71	1.67	1.1	2.2
Cs	8.6	28.6	17.4	21.4	13.4	10.2	42	38	8.5	30	5.7	24	19	18	10	18	12	48	11	22
Ba	146	303	1380	113	106	138	399	648	423	44	398	963	111	194	127	92	337	77	576	41
La	7.7	14.3	39.3	9.0	28.2	7.0	31	57	29	3.3	24	40	6.4	5.5	15	17	15	10	35	3.4
Ce	10.8	24.1	56.6	16.5	45.0	18	42	74	61	10	51	75	13	13	24	38	34	19	63	8.6
Pr	2.5	4.7	6.2	1.8	4.7	1.9	4.8	8.7	6.3	0.896	5.5	8.1	3	2	5.1	5.9	5.3	1.7	6.9	1
Nd	10.8	21.1	20.6	5.2	14.6	6.9	15	26	22	4	19	28	11	8.1	19	24	24	6.0	25	4.8
Sm	3.9	7.1	3.0	1.1	2.8	2.6	1.8	4	4.8	2.0	4.4	4.8	5.6	3.4	4.8	7.0	8.1	1	4.6	2.3
Eu	0.20	0.39	0.55	0.15	0.23	0.16	0.3	0.750	0.48	0.11	0.44	1.0	0.27	0.23	0.20	0.15	0.11	0.19	0.78	0.13
Gd	5.2	8.09	2.12	1.15	2.95	4.0	1	2.5	3	2.9	3.7	3.5	7.8	5	4.4	6.3	8.0	1.0	3.2	3.0
Tb	1.1	1.49	0.35	0.19	0.61	0.79	0.2	0.36	0.53	0.62	0.56	0.47	1.7	1.1	0.84	1.2	1.3	0.17	0.45	0.65
Dy	8.5	10.70	2.47	1.52	4.86	6.3	1.5	2.1	2.8	4.6	3.3	3.2	13	10	6.3	7.8	9.2	1.2	2.7	5.1
Ho	1.7	2.28	0.56	0.35	1.1	1.3	0.3	0.39	0.49	0.92	0.54	0.55	2.7	2.2	1	1.5	1.8	0.28	0.5	1
Er	5.5	6.82	1.68	1.15	3.5	4.24	1	1	1	2.8	1	2	8.0	7.1	4	4.5	5.3	1.0	1	3.2
Yb	6.3	8.18	2.10	1.84	4.2	5.0	1	1.4	1.2	3.4	1	1.7	9.6	9.1	4.4	5.0	5.9	1	1.2	3.9
Lu	0.87	1.15	0.32	0.30	0.66	0.71	0.2	0.21	0.15	0.45	0.17	0.26	1	1	0.61	0.71	0.79	0.24	0.18	0.55
Hf	5.5	7.50	3.47	3.80	4.9	5.4	3.1	2.9	3.4	3.6	3.7	4.8	6.2	6.6	4.7	6	5.5	3	3.7	4.0
Ta	3	3.77	1.99	3.49	3.2	3.2	2	2	2	3.4	2	2	6.8	7.1	2.3	3	3.0	3	2	3
Pb	7.0	12.15	16.22	14.55	16.0	6.7	17	22	35	17	15	2.7	28	11	8.1	14	8.6	15	42	10
Th	43	59.26	24.30	28.41	35.2	40.4	26	24	20	31	20	15	35	38	49	49	47	25	14	32
U	5.27	7.23	3.24	9.85	2.2	3.8	3	4.2	6.8	3.4	6.3	4	19	14	8.3	5.5	7.8	5.2	6.1	6

4.7 Geochemistry

Whole rock major and trace element contents of the 20 samples analysed for this study are presented in Table 3. The data shows that all samples have a very high silica (SiO_2) content, ranging from 69.64 wt% to 81.12 wt%. Also the aluminium (Al_2O_3) contents are high, ranging from 10.05 wt% to 14.52 wt%. Other major oxide contents (in wt%) are K_2O (3.65 – 10.18), CaO (0.04 – 1.76), Na_2O (0 – 3.06), Fe_2O_3 (0 – 1.89), MgO (0.03 – 0.82), MnO (0 – 0.04), P_2O_5 (0 – 0.21) and TiO_2 (0.01 – 0.38). The error assessment of the ICP-MS data, yields that the analytical precision for the trace elements Cr, Ni, Cu, Zn, As and Mo is relatively low ($\text{RSD}\% > 10$ for 6 samples or more). Important to note is that for Ni (%RSD of 9 – 118) this is due to the slow breakdown of the skimmer cone inside the mass spectrometer that consists of nickel. For the rare earth elements (REEs), only europium (Eu) has a significant analytical error ($\text{RSD}\%$ of 11 – 83 for 17 samples). Caution is thus required in interpreting data from these elements.

The rock classification diagram in Figure 24 confirms that the rocks can be classified as rhyolites.

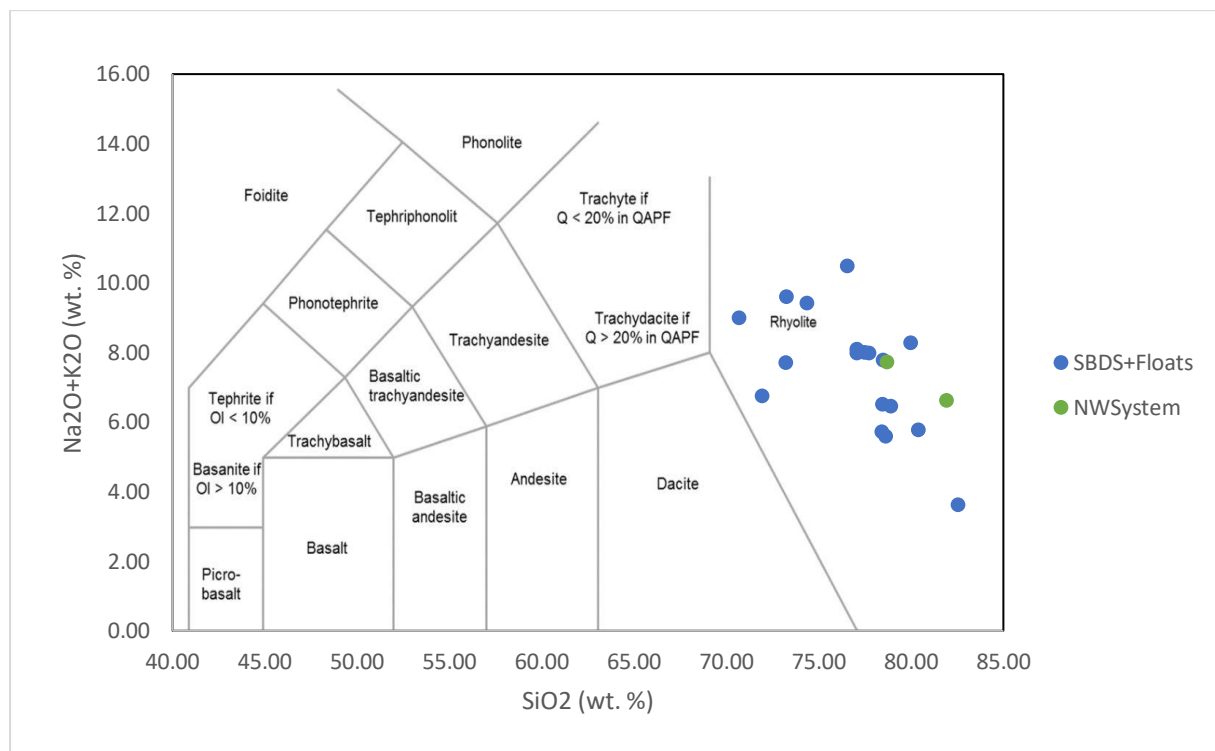
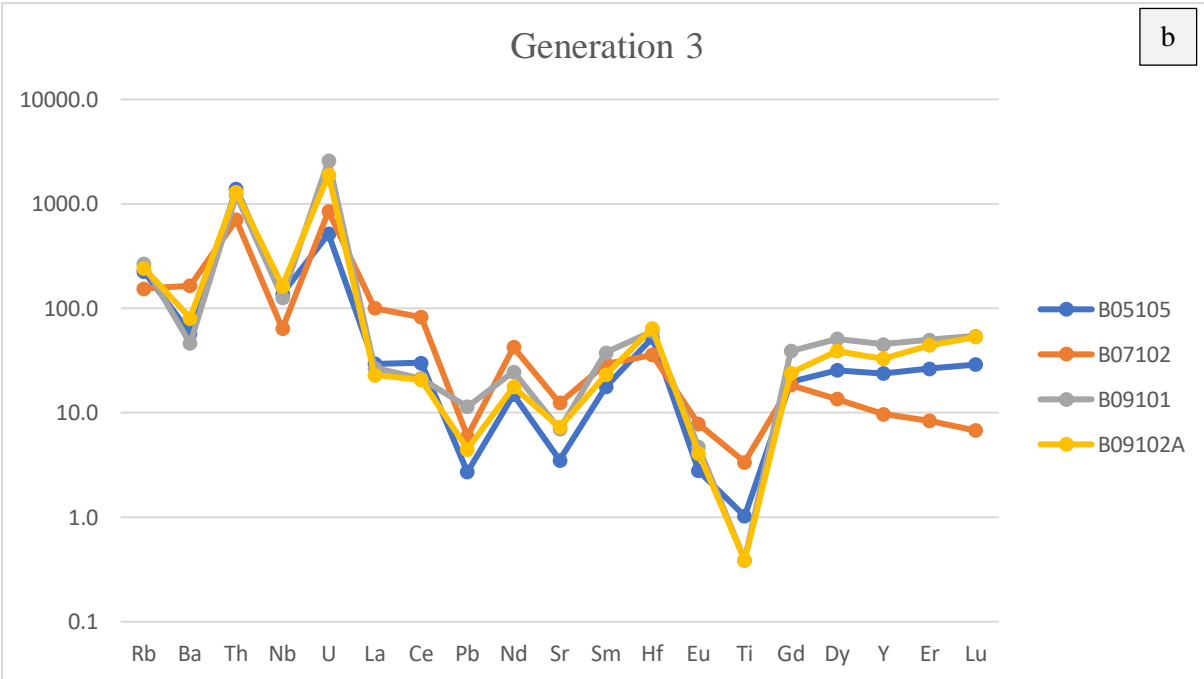
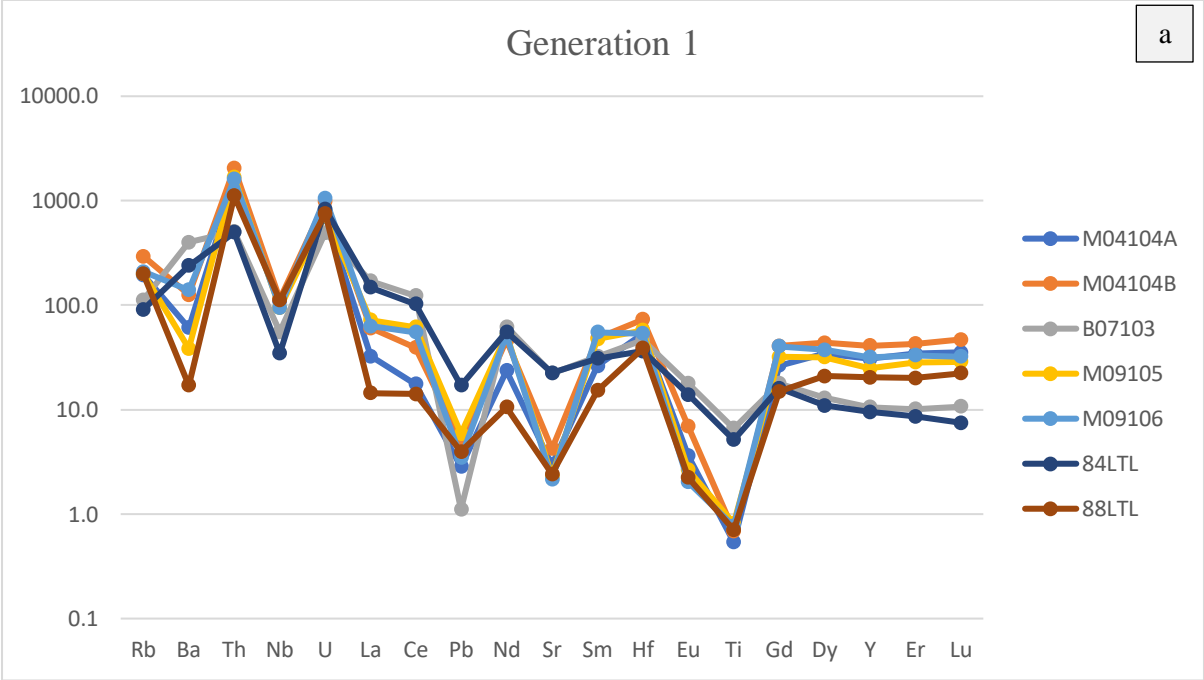


Figure 24: SiO_2 vs. $\text{Na}_2\text{O} + \text{K}_2\text{O}$ rock classification diagram after Le Bas et al. (1986).

Chondrite-normalized trace element spider diagrams are presented in Figure 25. Here, samples are grouped, based on dyke generation. Floatstones are plotted separately, as are samples M05101 and M10101 from the north-western part of the Freiberg district. The diagrams show that there is much variation in the dykes' geochemical content and that there is no clear geochemical distinction between the dyke generations.

All samples contain (strong) positive Th and U anomalies. Also negative Ba, Pb, Sr and Ti anomalies are a general feature, with an exception for samples B07103 and 84LTL from generation 1 and sample M05101 from the north-western dyke system that show contrasting (weakly) positive Ba anomalies. There is a strong variability in the strength of these four anomalies and a pattern can be observed; they all vary similarly within the same sample. This means that samples with a weak (or even slightly positive) Ba anomaly, also contain relatively weak Pb, Sr and Ti anomalies. Again, sample B07103 provides an exception on this rule, since it contains a very strong Pb anomaly, in contrast to the other three elements.



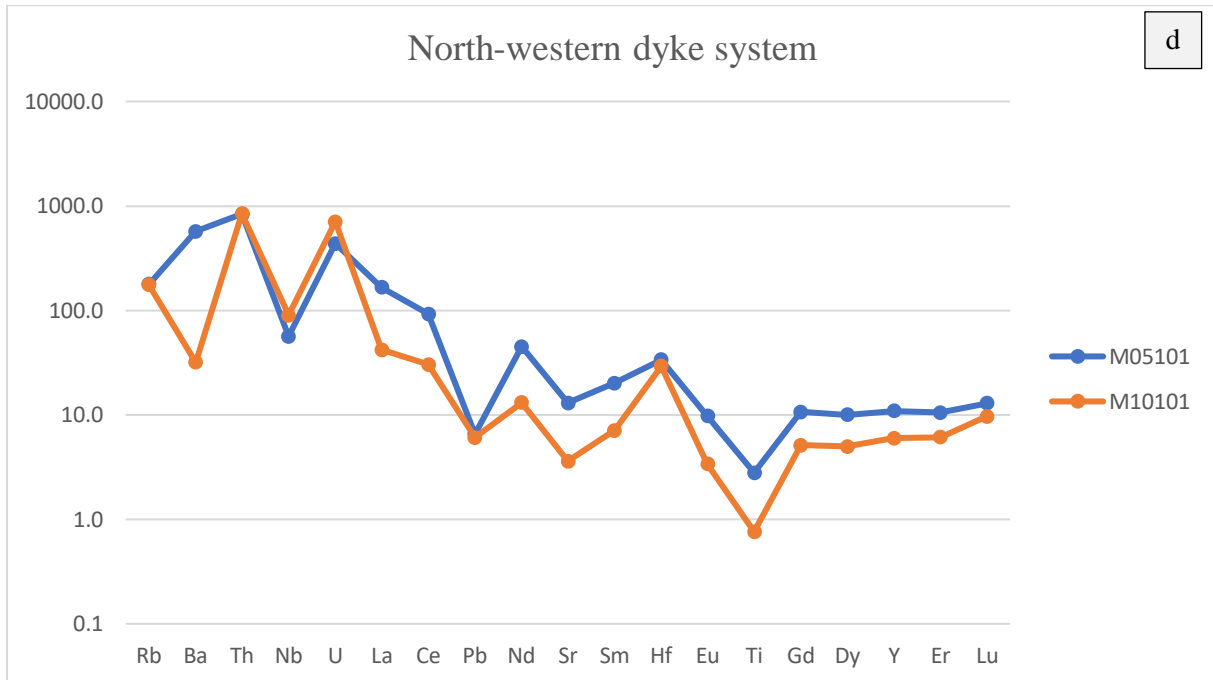
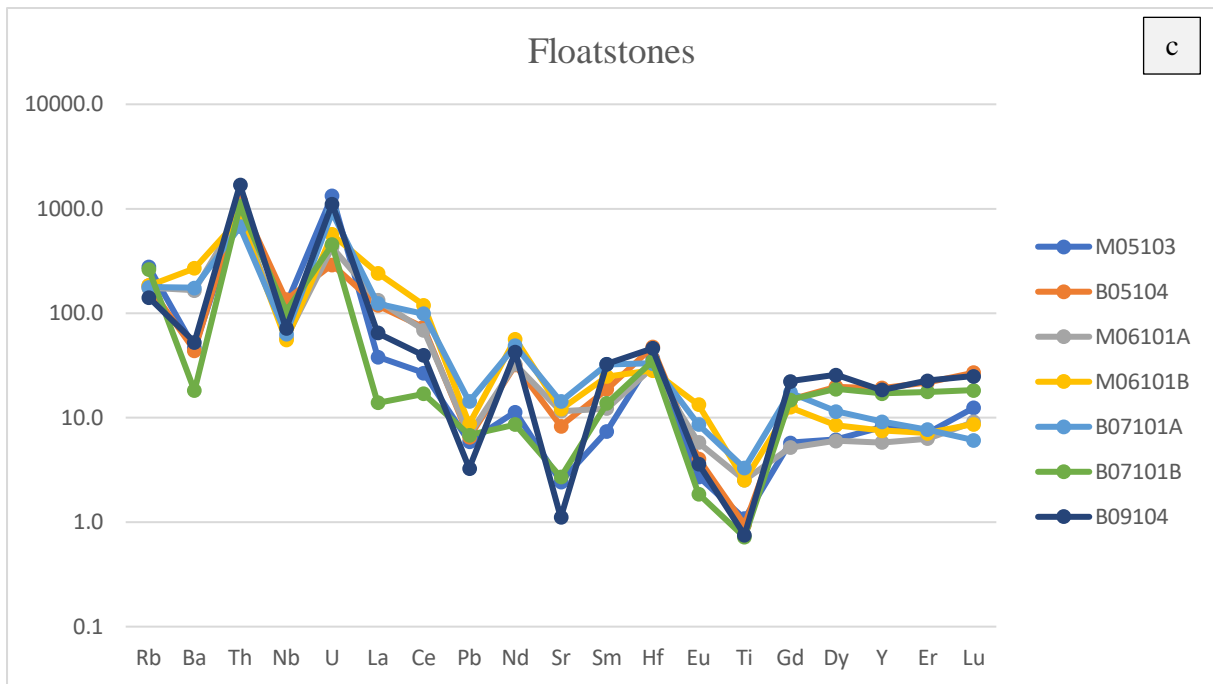


Figure 25: Chondrite-normalized trace element patterns of a) samples from the first generation of the SBDS, b) samples from the third generation of the SBDS, c) samples from floatstones and d) samples from the North-Western part of the Freiberg district. Normalization values from Sun & McDonough (1995). Values are given in ppm.

Figure 26 shows the chondrite-normalized REE patterns. Again, it becomes apparent that there is a strong variability in geochemical content of the samples and that there is no clear distinction between dyke generations one and three.

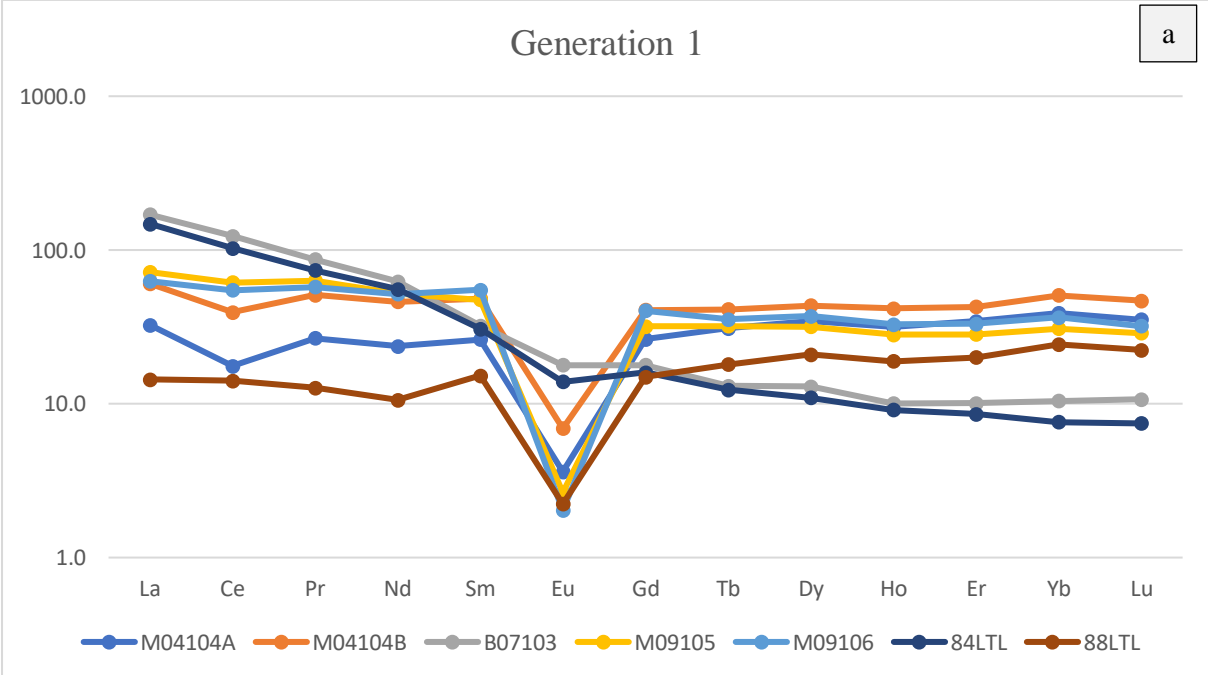
Based on the REE pattern, roughly four groups can be identified for samples from the SBDS. The first group has a negative slope (light rare earth elements (LREEs) > heavy rare earth elements (HREEs))

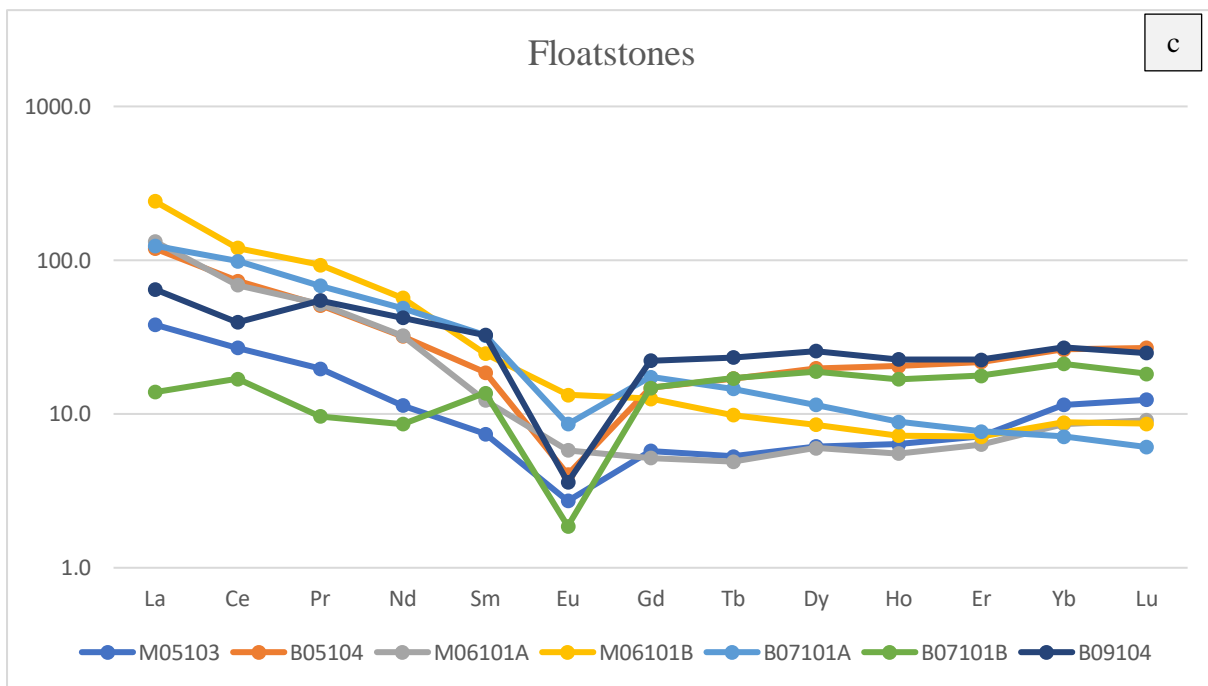
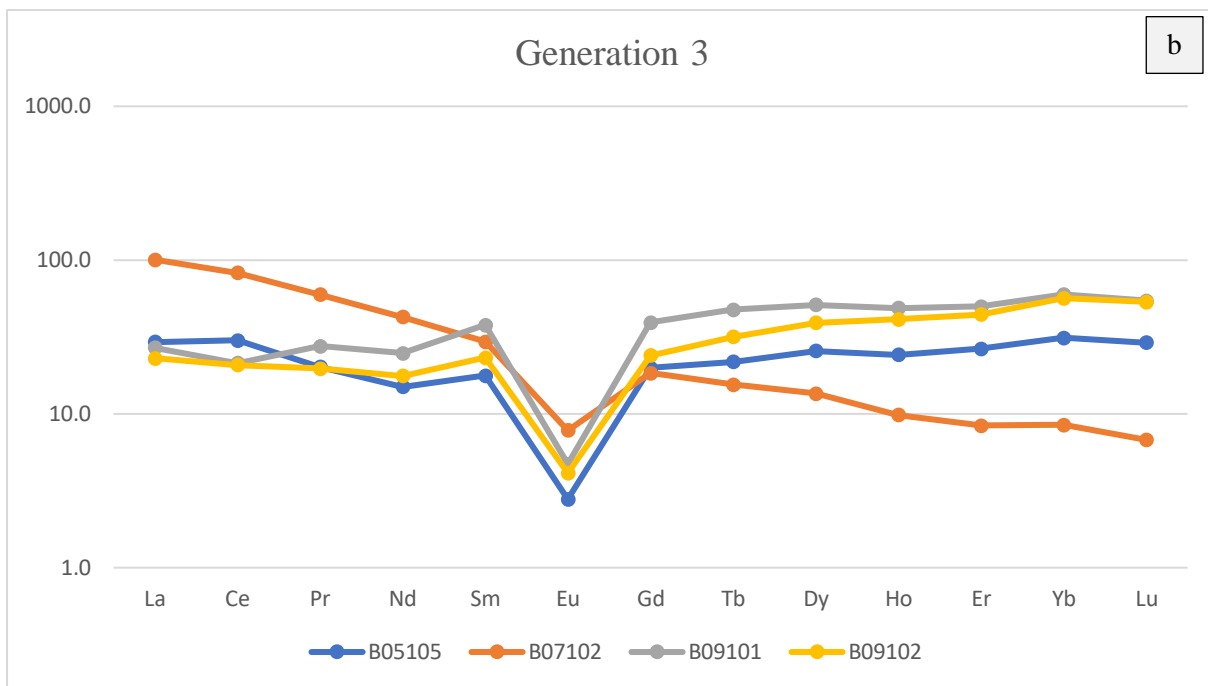
and a weak to almost absent negative Eu anomaly. To this group belong samples B07103 and 84LTL from generation 1, sample B07102 from generation 3 and floatstones M05103, M06101B and B07101A. Important to note is that the absolute REE contents of these samples strongly vary, but the overall pattern is similar. This group with a weak Eu anomaly coincides with the group of samples that include relatively weak Ba, Pb, Sr and Ti anomalies in their trace element spider patterns (Figure 25). Similarly to group one, the second groups of samples also has a (weak) negative slope, but shows a much stronger negative Eu anomaly. Samples M09105 and M09106 from generation 1 and floatstones B09104 and B05104 are appointed to this group.

The third group of samples has a flat (LREEs = HREEs) to positive slope (LREEs < HREEs) in their REE pattern and a strong negative Eu anomaly. Samples M04104A, M0410B and 88LTL from generation 1, samples B05105, B09101 and B09102 from generation 3 and floatstone B07101B show such a pattern. In a similar relation as for group one, the samples that are classified as groups 2 and 3 with a relatively strong negative Eu anomaly also contain strong negative Ba, Pb, Sr and Ti anomalies in their trace element spider diagrams (Figure 25).

The two samples from the north-western dyke system and sample M06101A from the floatstones form the last group, based on their REE content. These rocks include a negative slope in their REE pattern (LREEs > HREEs) and a weak to almost absent Eu anomaly, similarly to the first group as described above. However, this group also has a strong middle rare earth element (MREE) depletion, which causes the REE pattern to flatten out from about Eu onward to the heavier elements.

In all groups, some samples display anomalous Ce behaviour, with both weak to strong positive and negative anomalies in the REE pattern.





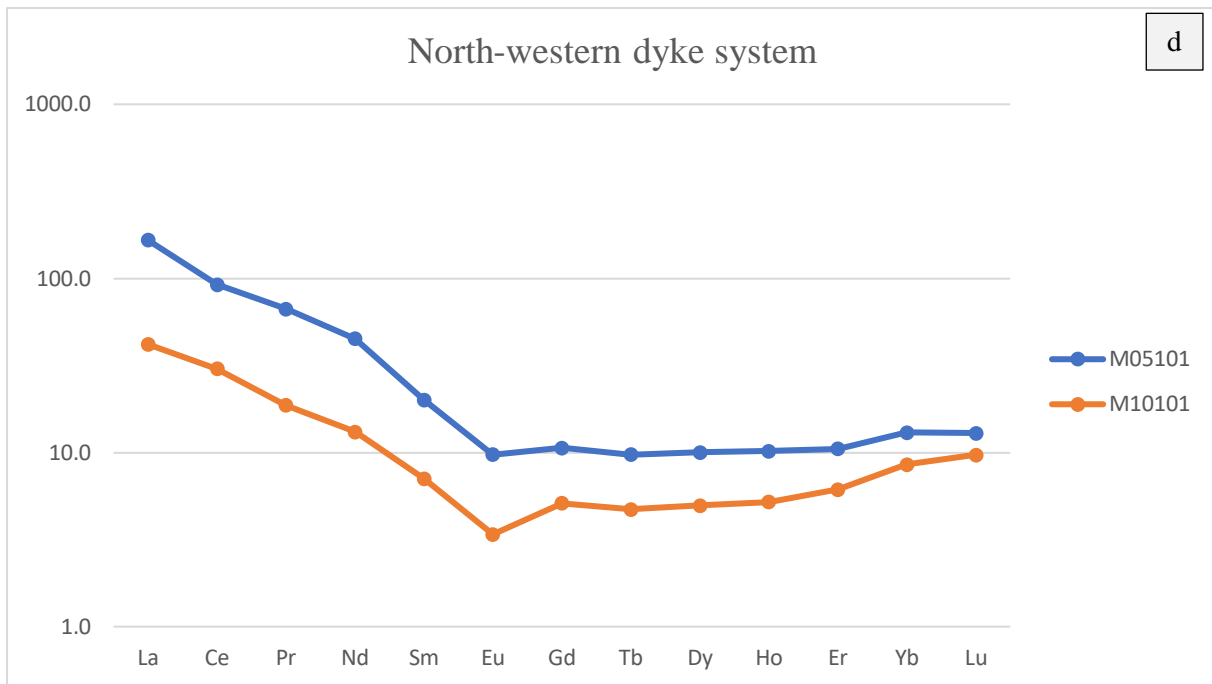
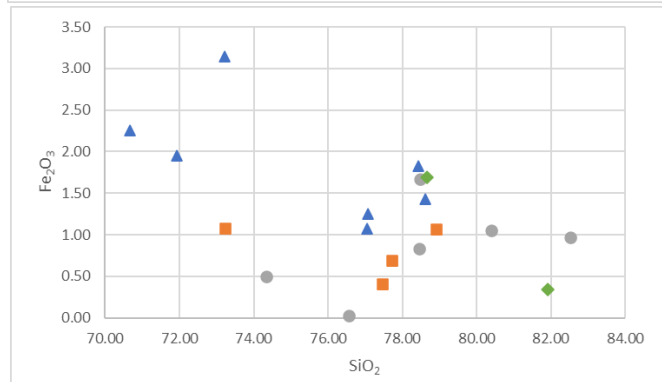
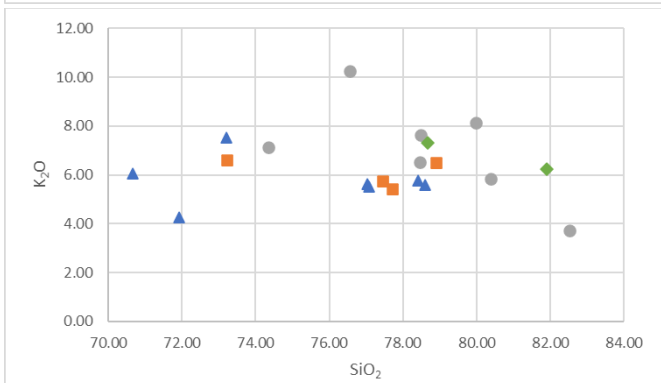
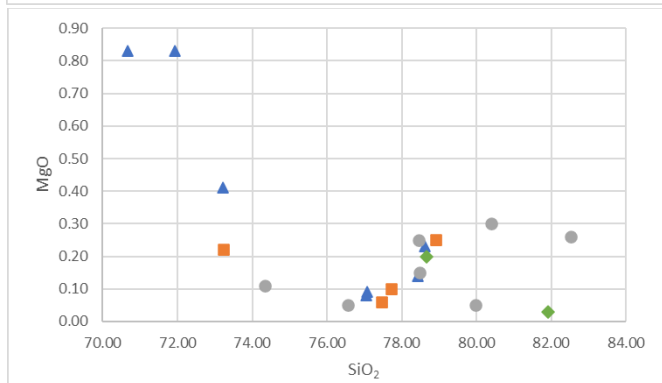
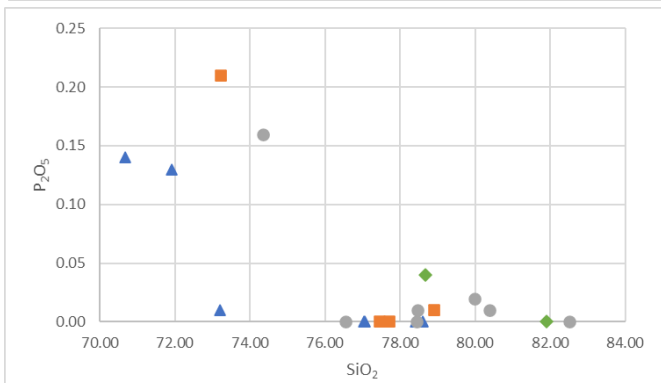
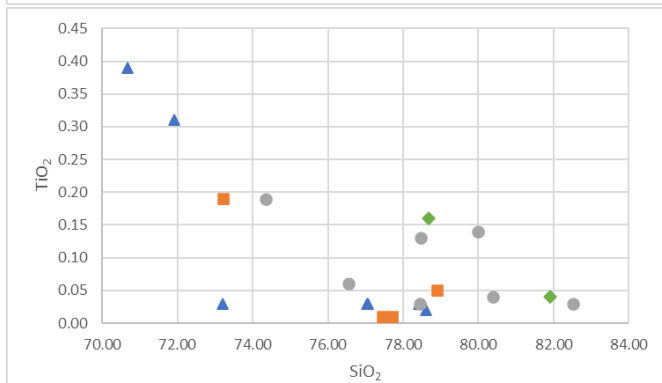
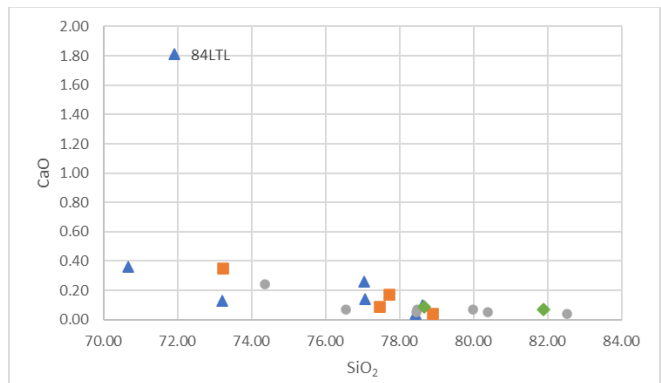
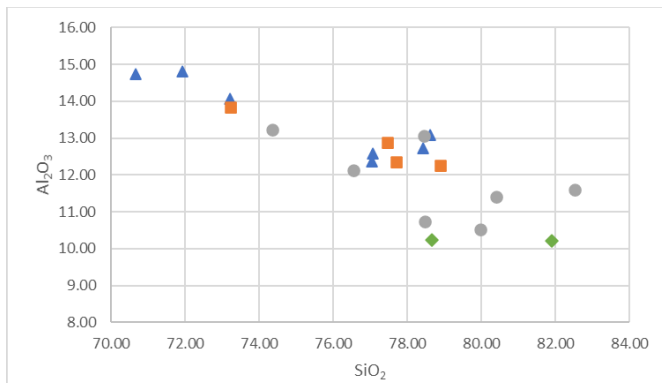
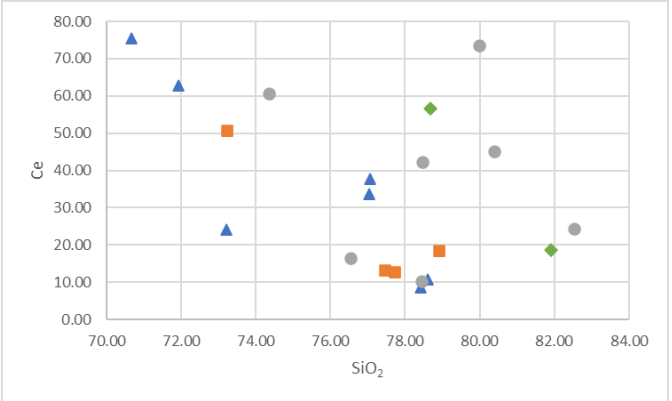
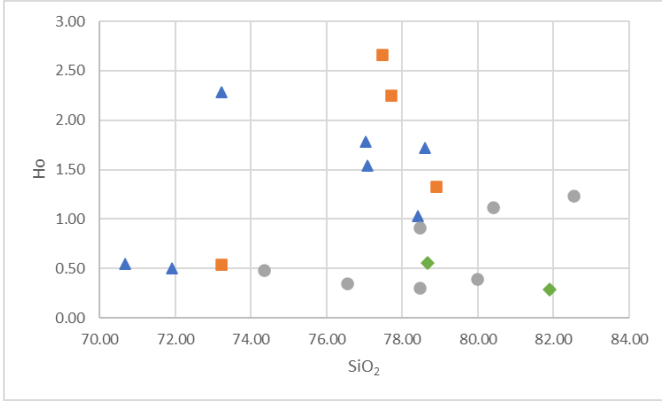
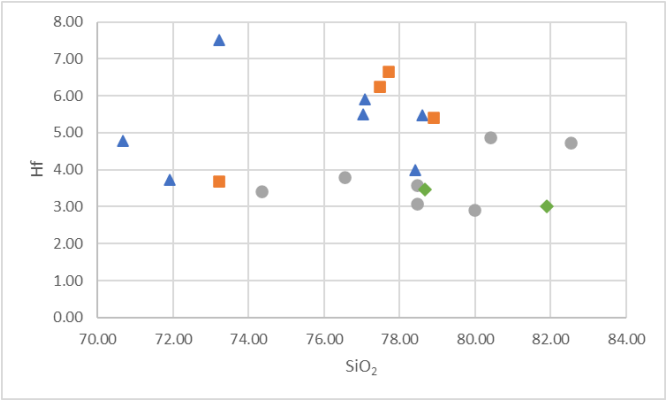
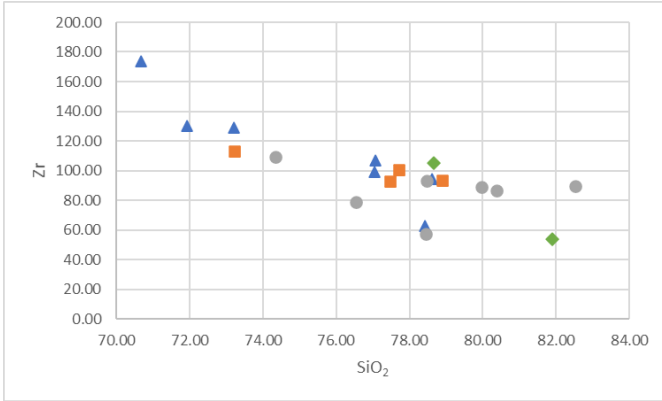
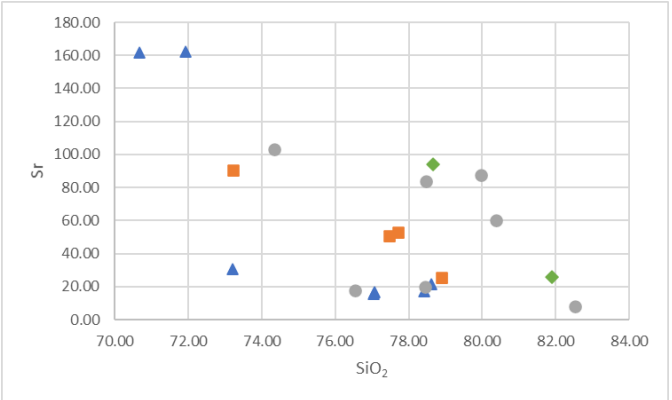
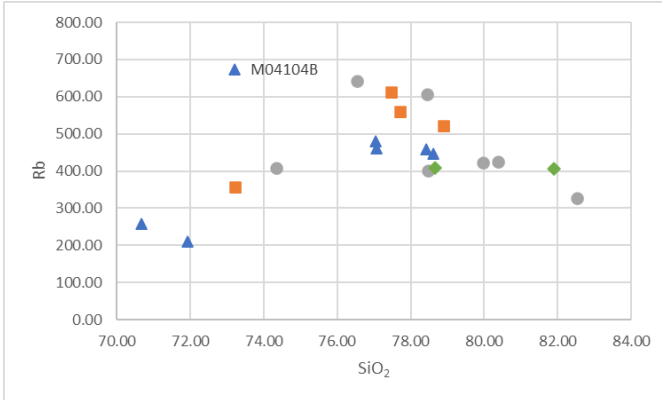
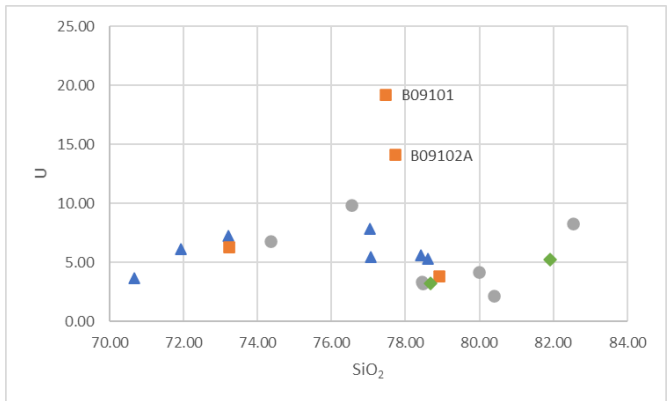
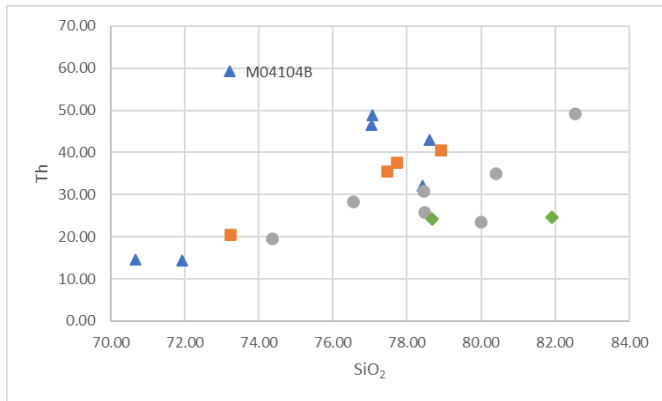


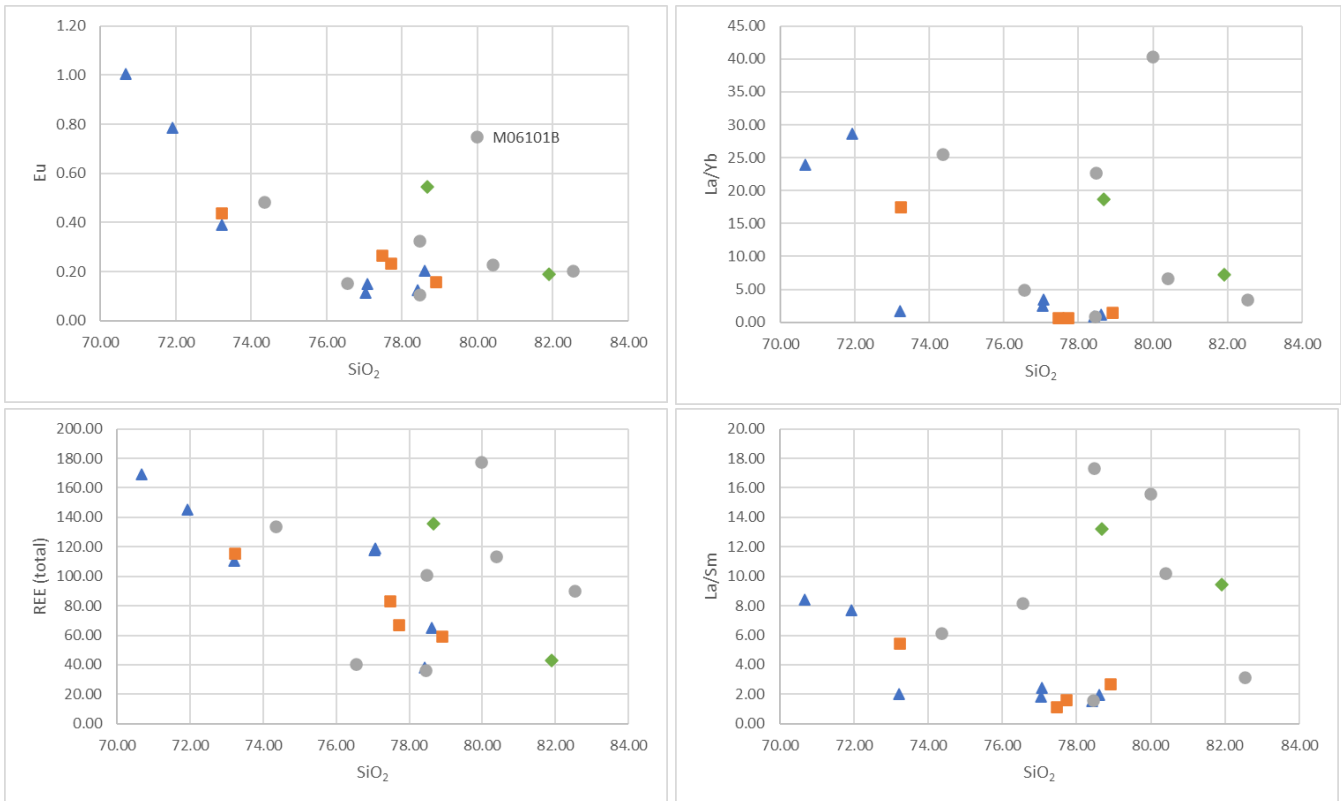
Figure 26: Chondrite-normalized REE patterns of a) samples from the first generation of the SBDS, b) samples from the third generation of the SBDS, c) samples from floatstones and d) samples from the North-Western part of the Freiberg district. Normalization values from Sun & McDonough (1995). Values are given in ppm.

Harker variation diagrams plot the concentration of a chemical constituent of a rock against a fractionation index; mostly its main constituent. These diagrams can therefore show fractionation trends in an igneous system. The Harker variation diagrams in Figure 27 plot SiO₂ as a fractionation index against other major and trace elements of the SBDS and the north-western dykes. In principle, these diagrams can only be applied to single systems. However, for comparison, samples M05101 and M10101 are also plotted. These two samples do unfortunately not provide a sufficient dataset to interpret any correlations/trends from for the north-western dyke system.



Legend:
 ▲ = Generation 1
 ■ = Generation 3
 ● = Floats
 ◆ = North-western dyke system





Legend:

- ▲ = Generation 1
- = Generation 3
- = Floats
- ◆ = North-western dyke system

Figure 27: Harker variation diagrams for all 20 samples from this study. Major oxides are in wt.% and trace elements are in ppm.

Many diagrams show a correlation in the dataset and often there is a kink in the slope of this correlation at about 78% silica, as will be described below.

For the major oxides, the Al_2O_3 and CaO plots shows a clear negative correlation with SiO_2 , that slightly flattens out around 78% silica. However, sample 84LTL forms an outlier in the CaO diagram, with an anomalously high calcium concentration. A similar pattern can be observed in the TiO_2 , P_2O_5 and MgO diagrams, but here the change in slope around the 78% silica boundary is stronger than for Al_2O_3 and CaO . In the K_2O plot this 78% silica boundary is only weakly defined, but it represents the transition from a slightly positive to a slightly negative slope in the data correlation. In the Harker diagram that plots the Fe_2O_3 concentration there is no strong correlation in the dataset, but generally the datapoints seem to follow a negative slope.

For the trace elements and REEs, a clear negative correlation is shown in the diagrams for Sr, Zr, Hf and Eu. However, there is a variation in the strength of the negative slope that is defined, with a much weaker negative trend in the Hf diagram than in the Sr, Zr and Eu diagrams. Sample M06101B forms an outlier in the Eu plot. Also, similar to the Al_2O_3 and CaO correlations, the slope (slightly) flattens

out around 78% silica on the x-axis. The Th, U and Rb datasets display the same pattern as K_2O , with a positive to negative slope transition around 78% silica. In both the plots for Th and Rb, sample M04104B provides an outlier with a high concentration. Sample B09101 and B09102A have a high concentration of U and also form outliers. In the diagrams that plot the REEs Ce, Ho and the REE ratio's La/Yb and La/Sm the data is scattered and no clear correlation can be observed. However, the total REE content of the samples shows a decrease with increasing fractionation index. Important to note is that in all Harker diagrams, similar fractionation patterns can be observed for both the first and third dyke generations. Also, samples M05101 and M10101 from the north-western dyke system do not plot significantly different from the SBDS in most of the diagrams. However, in the Harker diagrams that include REEs, the correlation patterns for the two dyke systems are similar but there is an offset between the two trends in which the north-western dykes plot above the SBDS.

5. Discussion

5.1 The influence of alteration processes

Rock alteration due to weathering is an important factor that needs to be avoided when accurately determining the (primary) whole-rock geochemical composition of a sample. Therefore, it is important to identify and take into account any weathering features before doing geochemical and mineralogical interpretations. As described in the results section, most samples from this study have a poor preservation state and include multiple weathering features as identified through microscopy and IR spectroscopy. FTIR data and corresponding pXRF measurements show (spectral) features that may indicate that the presence of iron-oxides is abundant in the obtained IR spectra from the samples. Therefore, in terms of geochemical analysis, the Fe_2O_3 data correlation in the Harker diagram from Figure 27, could be influenced by weathering processes and interpretation of this diagram should be done with caution.

However, to further assess the significance of the influence of weathering processes on the geochemical composition of the samples, a good indication of the degree weathering is given by their loss on ignition value. In contrast to the what is discussed above and suggested by microscopic and spectroscopic observations, the LOI values that were determined during the whole rock XRF measurements of the samples and that give an indication of the concentration of volatile compounds that are included in the rock are all relatively low (< 2.826 wt.%) (Table 3). Also, there is no clear indication in the geochemical results for a significant influence of weathering, with one possible exception; the Ce concentration. Ce is part of the LREEs and Figure 26 shows that several samples include (slightly) anomalous Ce concentrations in their REE pattern (samples M05101, M06101A,B, M04104A,B, B09101, B05105, B07101B and B09104). In contrast to other REE elements, Ce can be prone to weathering due to its strong sensitivity to the redox state of the environment (Middelburg et al 1988). Oxidation – reduction reactions that might occur during the weathering process could cause a transformation of Ce^{3+} to Ce^{4+} and vice versa, which influences the solubility of the element (Middelburg et al., 1988). However, according to Lee et al. (2013) (and references therein) the negative Ce anomaly in fresh granites could, apart from supergene processes after emplacement (weathering), be inherited from a hydrous magma source that previously existed near the surface or be caused by oxidizing conditions in general. For the dykes from the Freiberg district, a near-surface magma source is unlikely, which will be discussed further down below. Instead, oxidizing conditions and thus the anomalous behaviour of Ce could, apart from weathering processes, be caused by magma-fluid interaction as a consequence of the hydrothermal activity in the area, which is also the case for part of the ATC (Förster et al. 2011). This link between the rhyolite dykes and the large hydrothermal system from the Freiberg district will also be discussed below.

Overall, weathering processes undoubtedly had an influence on the mineralogical characteristics of the rhyolite dykes from the Freiberg district. However, in contrast, there is no strong indication that

weathering processes had a significant influence on the geochemical signature of the rocks that is therefore interpreted to represent primarily their magmatic composition.

5.2 Flow differentiation

The rocks from the SBDS and the north-western dyke system feature a strong variation in concentration of matrix and mineral abundances as shown by the point counting results (Table 2). Here it should be noted that floatstone sample M06101B, that seems to include vesicles, could be a lava based on this characteristic. As for weathering processes, the cause for the strong variation in textural and mineralogical characteristic in the suit of samples could be of importance in the geochemical content of the rocks and therefore in determining the magmatic history of the dykes.

The strong variation in phenocryst content of the SBDS was also recognised by Freyemark et al. (2015) for the FF-dyke. They made a spatial divide in their samples, based on matrix percentage. Type A is phenocryst rich (matrix $< \pm 60\%$) and occurs in the south-eastern part of the FF-dyke, type B is phenocryst poor (matrix $> \pm 60\%$) and occurs in the north-western part of the FF-dyke (Freyemark et al., 2015). For the samples from this study that were taken in situ, only samples B07102 and 84LTL could be classified as type A, with a matrix concentration of 60.9% and 63.7% respectively. However, since these are only two samples that were taken from both a first and third generation dyke, it is not possible to either spatially nor temporally apply the divide between the two rhyolite types of Freyemark et al. (2015) on the whole SBDS.

An important factor in the large scale variation in phenocryst and mineral content of the dykes from the Freiberg district, that is also identified by Freyemark et al. (2015) for the FF-dyke, could be flow differentiation. Along the whole length of the FF-dyke flow differentiation occurred during dyke emplacement, causing an increase in phenocryst concentration from dyke rim to centre (Freyemark et al., 2015). This mechanism could also account for the difference in point counting results of the samples from Röthenbacher Berg (M04104A+B, M09105, M09106).

But flow differentiation not only causes a zonation in phenocryst content in the dykes, as a consequence also a chemical zonation can be identified (Freyemark et al., 2015). Freyemark et al. (2015) systematically sampled the FF-dyke from rim to core and obtained a chemical profile along this sampling axis for several trace elements (Figure 28). The profile shows the chemical effect of flow differentiation, which could also be of influence in the chemical difference between samples B09101 and B09102A (Figure 29), that were taken from a dykes' interior and exterior respectively. In fact, the effect of the chemical zonation in the FF-dyke as visualized in Figure 28 for U, La, Pr, Nd, and Sm can be similarly applied to samples B09101 and B09102A, with a slightly larger concentration of La, Pr, Nd and Sm in the dykes' interior (B09101) than exterior (B09102A) and a very similar concentration of U along the sampling profile (Figure 29). However, this effect is only small. Also, on

regional scale, the ratio's of elements are per sample evenly influenced by the differentiation process and the chemical zonation effect is only slight for the elements of interest (Figure 29). Therefore, the effect of flow differentiation is considered to be insignificant for this study in terms of geochemistry and only to provide a background noise in the geochemical dataset.

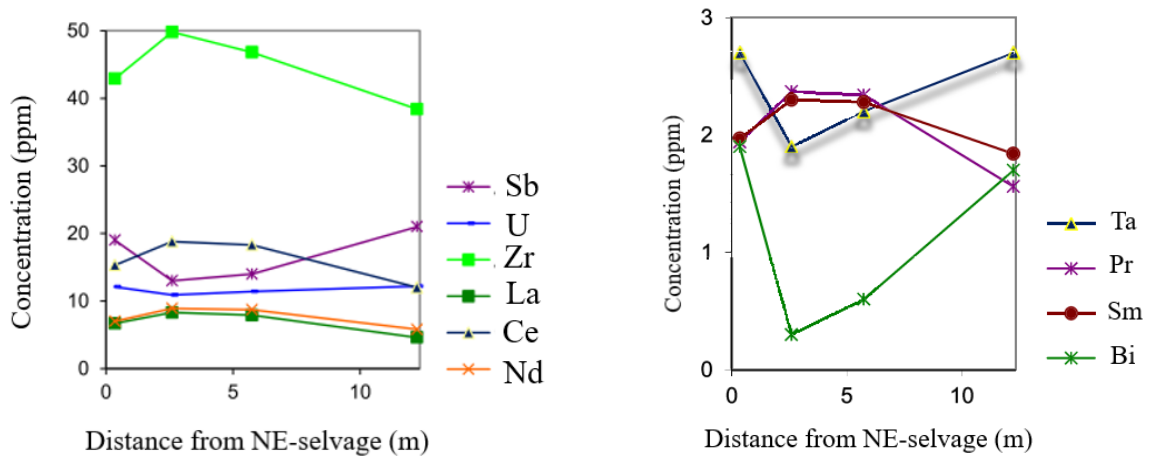
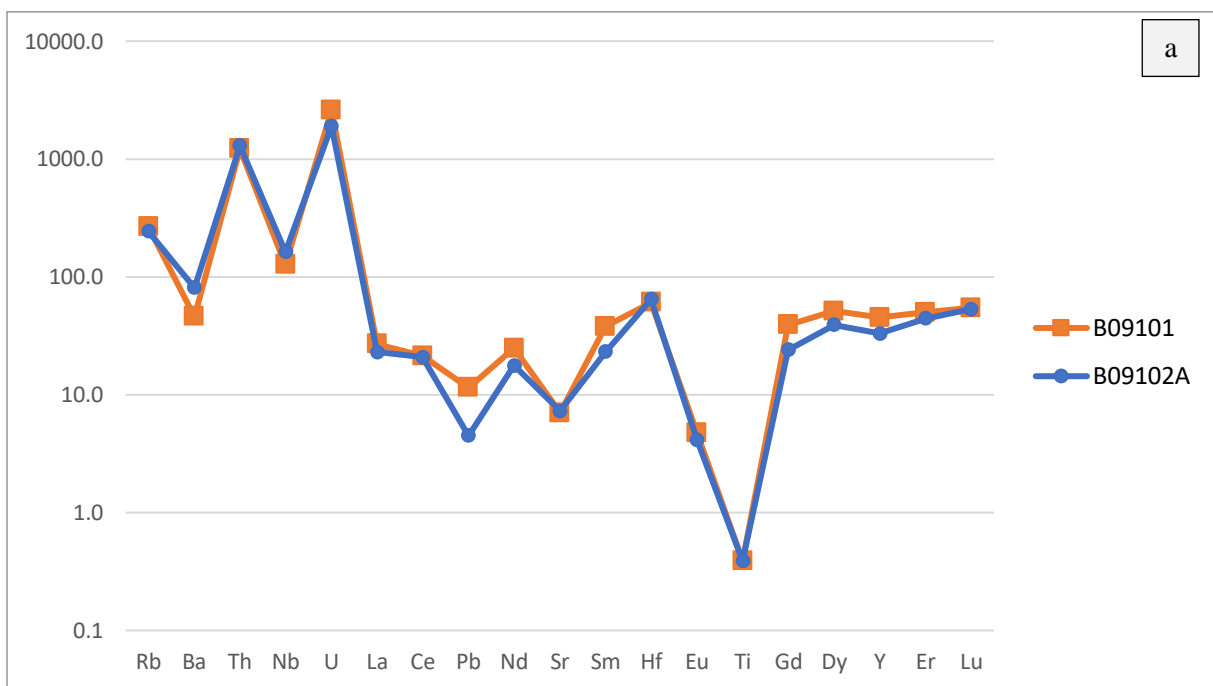


Figure 28: Selected trace elements in the profile of the FF-dyke in the Reiche Zeche mine. From Freyemark et al. (2015) (translated).



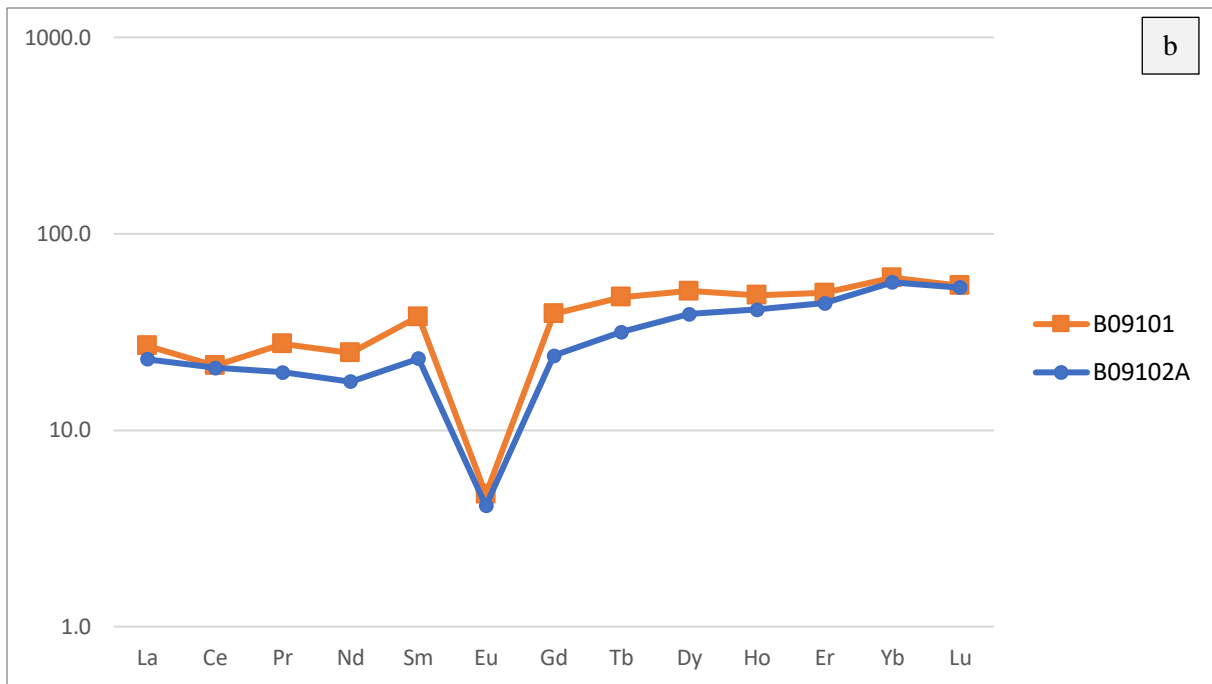


Figure 29: Chondrite-normalized trace element (a) and REE (b) patterns of samples B09101 and B09102A that are from a dykes' interior and exterior respectively. Normalization values from Sun & McDonough (1995). Values are given in ppm.

5.3 Fractional crystallization history

After concluding that the samples from this study have retained their primary composition during weathering processes and that flow differentiation was a chemically insignificant factor during dyke emplacement, clues about magmatic history and source magma composition can be derived from the geochemical content of the rock. Therefore, the geochemical data from this study may shed light on some important fractional crystallization trends that occurred during magma evolution. In many of the Harker diagrams, fractionation trends are visualised that reflect the formation of the rock-forming minerals in the dykes (Figure 27). The negative trends in the Al_2O_3 and CaO diagrams are linked to plagioclase fractionation. Also the Sr and Eu Harker diagrams show this fractionation trend, since these are compatible elements in the mineral. This is consistent with the negative Eu anomaly that is to a certain degree featured in the REE patterns of all samples (Figure 26). The fact that the negative slope in the Al_2O_3 and CaO diagrams flattens out around the 78% silica boundary is linked to the pattern that is observed in the K_2O Harker plot. The trend in the K_2O data first features a positive slope and around the 78% silica line this shifts to a slope with a negative sign. Earlier in the melt history K_2O is thus an incompatible compound, which changes during the system's evolution. This is consistent with the common early fractionation of plagioclase from the melt and subsequent fractionation of K-feldspar, that readily incorporates K_2O in its structure. This fractionation effect is also observed in the Rb Harker diagram, since Rb can substitute for K in K-feldspar.

The negative trend that is shown by the MgO Harker plot is caused by biotite fractionation. MgO is also fractionated by amphibole, which is a very common mineral and could also be of influence on the correlation pattern. However, no amphibole was recognized in the rock samples, so there is no indisputable evidence for this. Crystallization of amphibole from the melt could also have had an effect on fractionation of Fe₂O₃, but again the Fe₂O₃ Harker plot does not confirm this theory. The scattered character of the Fe₂O₃ dataset in the Harker diagram is common, since Iron is a constituent of many minerals and its concentration is thus influenced by many factors. Also the relatively high concentration of iron in the weathering features in the samples, as discussed previously, could be of influence on this scattered plot.

Some Harker diagrams show outliers in the dataset such as sample 84LTL in the CaO plot and sample M04104B in the Rb diagram. This could have to do with different local events in the history of the samples that are common in magmatic systems such as local magma mingling, assimilation or even weathering and bad preservation.

As shown in the results section, the dykes from both the first and third generation and the floatstones show a great variation in trace element patterns and REE patterns with positive and negative slopes and a great variety in the strength of the negative Eu anomaly (Figure 26). This suggests that both evolved and less evolved rocks were formed during intrusion of both dyke generations. Winter et al. (2008) and Freymark et al. (2015), who only studied first generation dykes of the SBDS, obtained similar geochemical data (Figure 30). Here, the FF-dyke represents a less evolved species. In this context, it is important to note that the two dyke generations of the SBDS also show very similar correlation patterns in all Harker diagrams (Figure 27). These characteristics could indicate a repeatedly fractionated magma source for the dyke swarm rather than a continuously fractionating source or maybe even different source magmas for the different dyke generations. This idea could also be linked to the change in slope of the correlation trend around the 78% silica line, which is defined in almost all Harker diagrams. However, the appearance of this line could also just be linked to continuous fractional crystallization, as is the case for the plagioclase – K-feldspar fractionation sequence, or indicate a magma mixing event, which will be further discussed later.

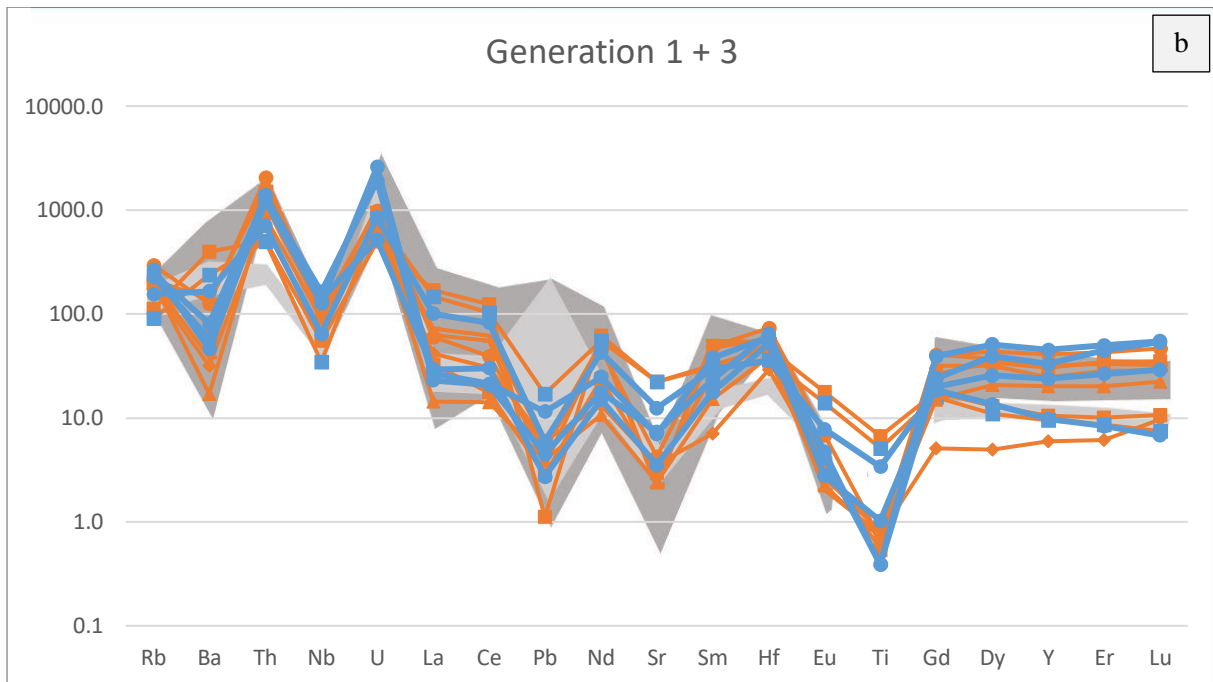
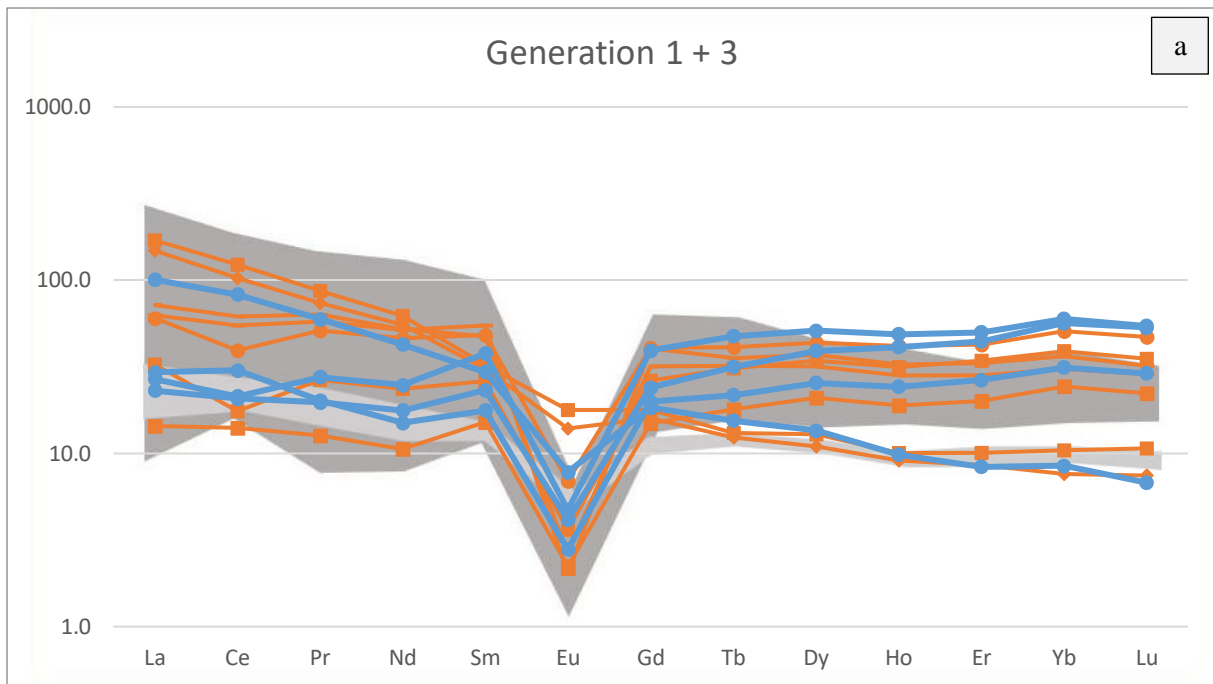


Figure 30: Chondrite-normalized REE patterns (a) and trace element patterns (b) of samples from the first (red) and third (blue) generation of the SBDS. Data from Winter et al. (2008) is represented by the dark grey background inset; from 'coherent rhyolite' samples only. Data from Freymark et al. (2015) is represented by the light grey background inset; only includes the FF-dyke. Normalization values from Sun & McDonough (1995).

The above discussion focusses on the general trends in the geochemical dataset, but something that is not accounted for is the actual cause of the broad variation in the REE and trace element patterns of the different dyke generations. In this context, the role of accessory mineral fractionation is important and will be discussed next.

In general, REEs are considered to be incompatible elements in magmatic systems (Miller & Mittlefehldt, 1982). However, HREEs are considered compatible in a system where garnet and/or amphibole fractionation is/are important (Miller & Mittlefehldt, 1982). In rhyolitic rocks, that are formed from highly evolved and fractionated magmas, a HREE depletion is thus common. Also, zircon crystals incorporate HREEs into their structure. The Zr Harker diagram clearly indicates continuous zircon fractionation throughout the melt evolution since the concentration of Zr almost continuously decreases with increasing silica content. Hf is similarly affected by zircon fractionation, but in the Hf Harker diagram the trend is less clearly defined. In addition, three of the four samples from the SBDS that were analysed under the TTSEM contain zircon crystals. These samples represent first generation dykes (B07103, 84LTL) and a floatstone (M06101A). In sample B07102, from a third generation dyke, no zircons were found. However, since the set of samples that was analysed under the TTSEM is small, drawing conclusions from the accessory mineral data should be done with caution and does not necessarily indicate a lack of zircon fractionation for the third dyke generation. There seems to be a drop in the La/Yb and La/Sm ratios and the total REE content around the 78% silica line in the Harker plots. This could also be linked to the HREE element fractionation by zircon. However, since there is no clear change in fractionation intensity of Zr at the 78% silica line, the quick drop in REEs in the Harker diagrams could also be caused by a change in zircon composition or fractionation of other accessory minerals. The latter will be discussed down below. To further investigate this idea, zircon mineral chemistry should be determined by a microprobe. The fact that no zircons were identified in samples M05101 and M10101 from the north-western dyke system could indicate a different fractionation history for these dykes. In addition, the REE patterns of the samples from the north-western dykes show a much stronger MREE depletion in comparison to the generations from the SBDS (Figure 26). This could be linked to the offset between the SBDS and north-western fractionation trends that can be observed in the REE Harker diagrams and will be discussed later. However, for this dyke system the suit of samples is too small to draw conclusions from and only yields substantiated speculation. Therefore still no clear indications are given for a genetic difference between the two dyke systems from the Freiberg district.

Apart from zircon, there are also indications of fractionation of other accessory minerals. For example, the Th and U trends in the Harker diagrams show a shift from a positive to a negative correlation around 78% silica concentration. At lower silica contents these elements are thus incompatible in the magma system, whereas in the more evolved state of the system this changes. Commonly, these elements have a high partitioning in zircon. However, since there is no correlation between the Harker diagram that plots Zr with a continuous negative slope and the Th and U correlation patterns, this suggests that other minerals also played an important role in the history of these elements and the source magma evolution.

This idea is supported by the TTSEM results and the flat REE pattern or even MREE and/or LREE depletion that is observed in many of the samples from the Freiberg district but is much less common in rhyolites than the previously discussed HREE depletion. As the SEM results show, samples M05101, M06101A, B07102, B07103 and 84LTL not only include zircon, but also rutile and/or titanite crystals. This is consistent with the relatively weak Ti anomaly in the normalized trace element patterns and the negative correlation trend in the TiO₂ Harker diagram. In addition, these samples show a distinct REE pattern with a negative slope, weak Eu anomaly and MREE depletion, which is particularly well defined in samples M06101A and M05101 (Figure 26). These characteristics likely have a causal link, since titanite fractionates MREEs over HREEs and LREEs and is the main MREE fractionating phase in high silicate, rhyolitic liquids (Xu et al., 2022). Also, titanite fractionation implements a positive Eu anomaly on the residual melt in granitic systems with an I- to A-type evolution, opposite to plagioclase (Xu et al., 2022). The effect of titanite fractionation on the whole rock REE pattern of the SBDS could thus yield the chemical results as obtained. In particular in the north-western dyke system titanite fractionation seems to have played an important role during magma evolution since both north-western samples display strong MREE depletion (Figure 26). The fact that the MREE depletion for these samples is much stronger than for the SBDS and thus possibly titanite fractionation played a key role in the magmatic history of these rocks, may be consistent with a separate magmatic evolution for the north-western dykes.

Furthermore, as stated above, the large variation in geochemical signature of the SBDS also includes samples with a positive REE slope and LREE depletion (Figure 26). Some accessory minerals, such as allanite (REE(Al, Fe)₃(Si₂O₇)(SiO₄)O(OH)) and monazite (REE(PO₄)), readily trap LREE in their crystal structure (Miller & Mittlefehldt, 1982). These minerals form during late stages of felsic magma fractionation and can cause a depletion in the rocks that are formed last from a felsic system (Miller & Mittlefehldt, 1982). The flat REE pattern in samples M04104A+B, M09105, M09106, B05105 and B09104, or even the positive slope in the REE pattern of samples B09101, B09102A, 88LTL and B09101B, could thus be caused by continuous fractional crystallization of the magma source and extremely late stage crystallization of the dykes. Unfortunately, any LREE fractionating minerals were not identified under the TTSEM, but this does not mean that such fractionation did not occur since accessories are easily overlooked. In fact, the P₂O₅ and total REE concentration Harker diagrams do suggest that one or more REE-rich and/or phosphorous phases fractionated in the more evolved magma system, with a negative correlation for both the two generations of the SBDS and the north-western dykes.

In addition, monazite fractionation can have the effect of creating a kink in the REE pattern at Nd – Sm, of a biotite-muscovite bearing granite (Yurimoto et al., 1990). This kink is to some degree also observed in samples M04104A, M04104B, B09101, B09102A, B05105, 88LTL, B07101B and B09104 (Figure 26). Since the composition of the rhyolite dykes from Freiberg is similar to the

biotite-muscovite bearing granite from Yurimoto et al. (1990), this could thus be indication of the influence of monazite fractionation on the irregular shaped REE pattern of the dykes. Important to note is that apart from the negative correlation trend in the P_2O_5 Harker diagram, there is no other indication of the importance of monazite fractionation in the magmatic history of the north-western dykes.

To investigate the possibility of monazite and/or other accessory mineral fractionation and to more precisely determine the crystallization history of the dykes and their source magma, fractional crystallization modelling with mineral geochemistry data could be performed in future work.

5.4 Magma mixing

During evolution of magmatic systems, the process of fractional crystallization (as discussed above for the dykes from the Freiberg district) may coincide with the process of magma mixing. Different lines of evidence, such as petrological and/or geochemical features, may be used to identify magma mixing processes and will be discussed below for the SBDS and north-western dykes.

Resorbed and embayed quartz are an abundant feature in the rhyolite dykes from the Freiberg district. Freyemark et al. (2015) also observed this textural characteristic and interpreted the resorption rims as being symplectites. However, quartz is in principle pure silica that is very inert and stable, so here this idea is discarded. Even more so since resorption of quartz has previously been studied in other granitic rocks from the Erzgebirge and is thus common in the region (Müller et al., 2005; 2008; 2010).

In definition, mineral resorption is the (partly) remelting/resorption process of crystals due to a change in intensive variables (e.g. P, T, αH_2O) in the melt (Hogan, 1993). Müller et al. (2005) looked at granitic rocks from the ATC and defined several resorption patterns in quartz crystals, by cathodoluminescence (CL) analysis. The CL analysis showed oscillatory zones inside the quartz crystals (snowball quartz) that featured truncated growth zones due to resorption. In turn, the oscillatory zoning indicates a change in mineral composition during crystal growth, that is caused by an interplay of magma chamber dynamics and local kinetic effects in the melt (Ginibre, 2002). Based on the truncated oscillatory zones in the quartz crystals from Müller et al. (2005), they interpreted the resorption texture to be caused by magma mixing, that induced a new thermal equilibrium leading to resorption and/or (re)growth of crystals. Later, they added the suggestion of semi-adiabatic magma ascent as a cause for the change in thermodynamic conditions, possibly related to mixing. Also, they found that minor resorption events could be caused by small changes in physical parameters by convection. However, since the quartz resorption is so abundant in the dyke samples from this study and can be observed to very different extends (Figure 31) a major resorption event seems more favourable here. To further investigate this idea, CL analysis could be performed to identify any possible oscillatory zones inside the quartz of the rhyolite dykes.

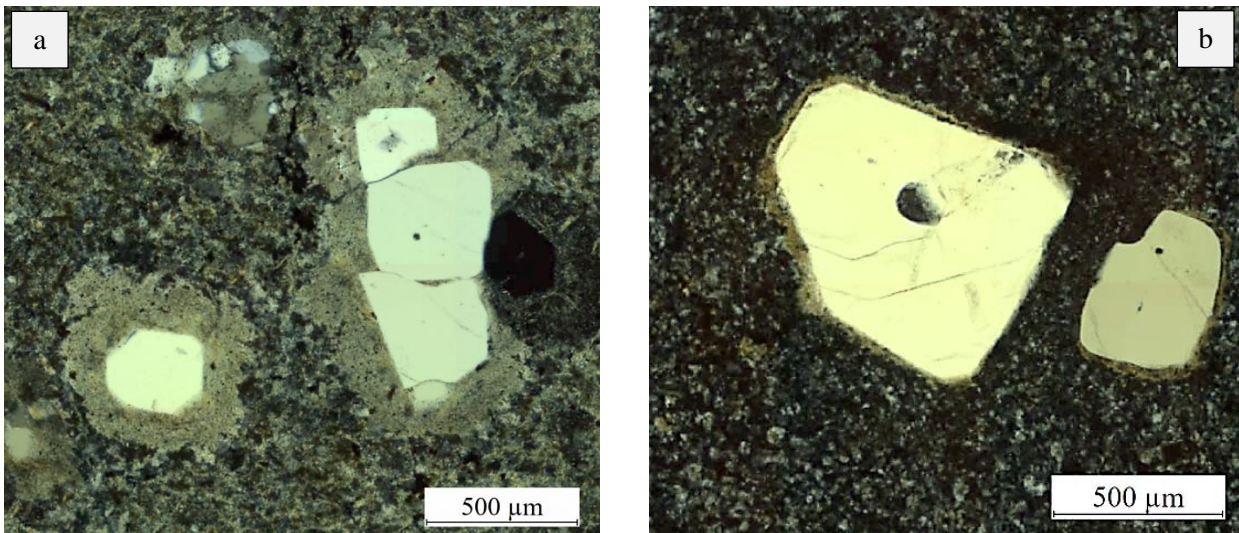


Figure 31: Different degrees of resorption in quartz phenocrysts from a) sample B09104 and b) sample M05103.

Another indication of a mixing event in the history of the source melt of the Freiburger rhyolite dykes could be found in the oscillatory zoned K-feldspar (Figure 22e). Zoning in plagioclase is common, since this mineral is one of the first to crystallize from a broad range of melt compositions (Bowen, 1922) and thus stays in suspension in the magma chamber. K-feldspar, however, crystallizes much later during melt evolution and the fractional crystallization process (Bowen, 1922). Zoning in K-feldspar thus indicates late-stage disequilibrium conditions during melt evolution and could be related to magma mixing. Furthermore, the sieve texture that is featured by some feldspar phenocrysts in the rhyolite dykes of the Freiberg district could also be linked to this possible mixing event. In fact, Müller et al. (2005, 2010) interpreted the sieve texture in plagioclase as remnants of oscillatory zoning that altered during resorption. Also, Nelson & Montana (1992) linked the sieve texture in plagioclase to the earlier mentioned adiabatic magma ascent. Again, this mechanism could well be linked to magma mixing.

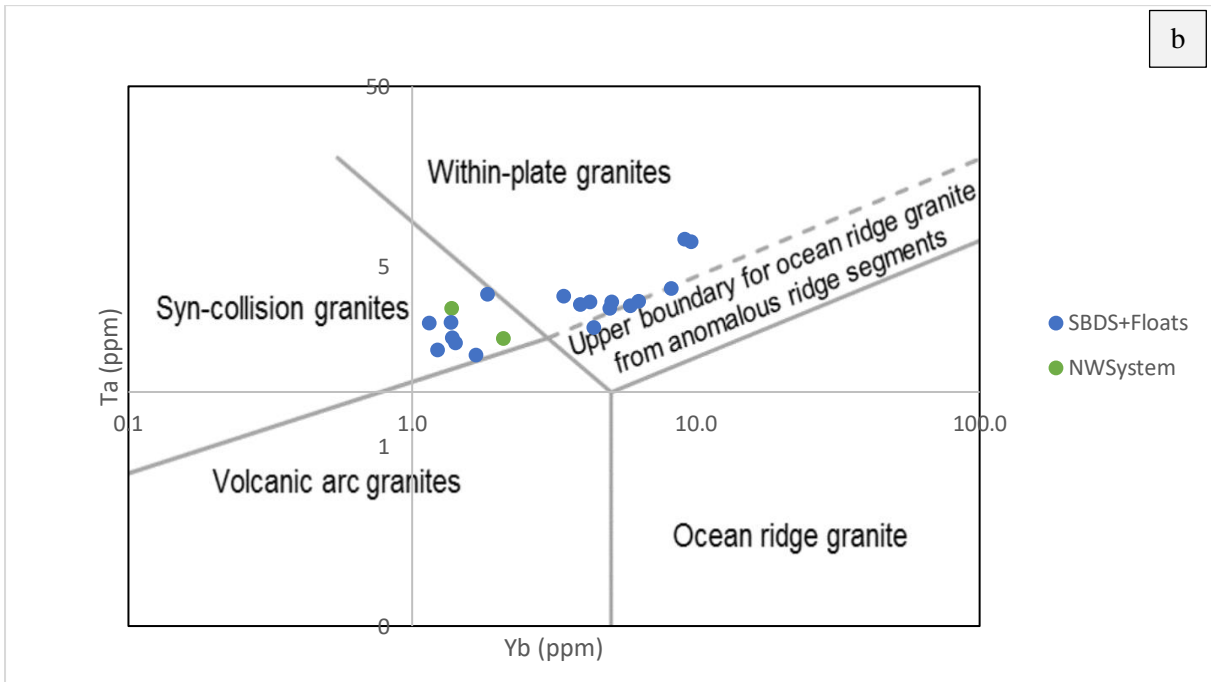
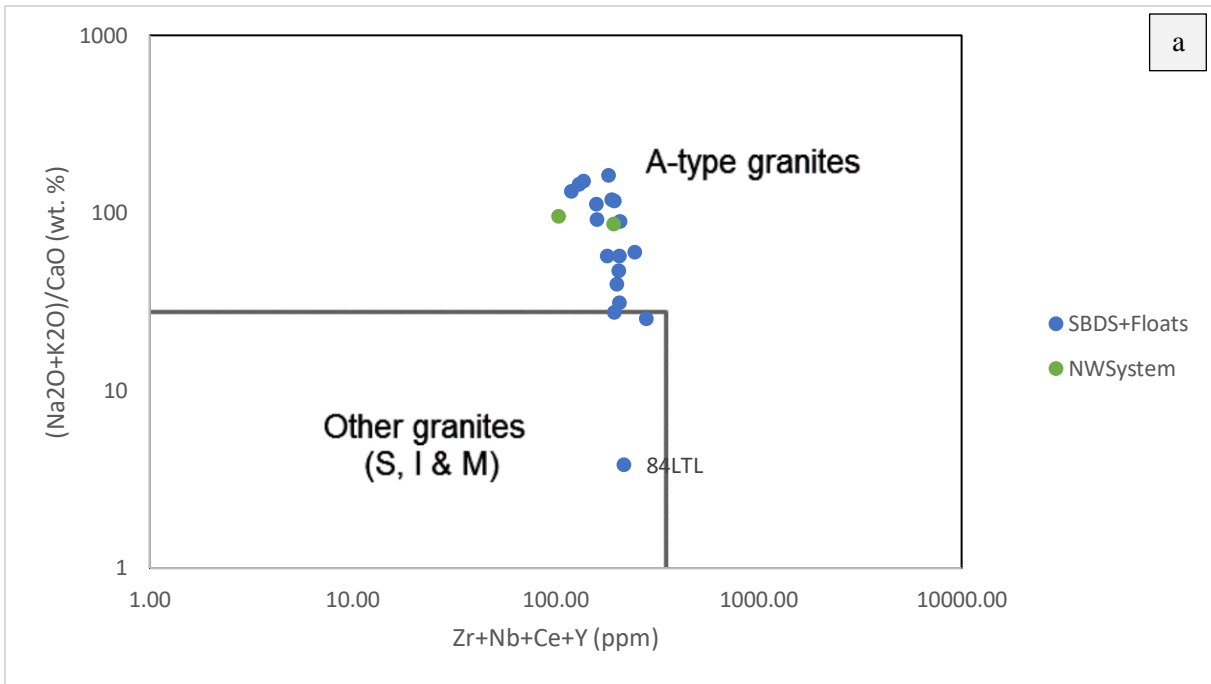
In the case that the mantled plagioclase phenocrysts in sample B07101A (Figure 21) is overgrown by K-feldspar, it features an anti-rapakivi texture. This texture, together with the dendritic plagioclase growth in for example sample M04104A, might also be linked to the idea of magma mixing. Hibbard (1981) (and references therein), who mainly studied the process of rapakivi and anti-rapakivi formation, in principle suggested magma undercooling as a mechanism for dendritic (or cellular) feldspar growth, induced by a mixing event that then yields (anti-)rapakivi textured feldspar phenocrysts. As previously mentioned, an undercooled environment could be expected during dyke emplacement. However, as a cause for the undercooling, magma mixing could thus also play role (Hibbard, 1981). Here, it is very important to keep in mind that the overgrowth on the supposed anti-rapakivi feldspar is unidentified and that sample B07101A is taken from a floatstone. The section above thus includes mere speculation.

The last important thing to discuss in the context of magma mixing is the ductile deformation structures in the open pit mine at the Röthenbacher berg (Figure 5). These structures might give a indication of magma mixing, as is also suggested by Winter et al. (2008), who actually collected samples that included more mafic, vesiculated material inside the rhyolite. Unfortunately the samples from this study that were collected at the mine did not provide such evidence. However, the discussion above gives a strong indication of the importance of magma mixing in the magmatic history of the SBDS.

How the north-western dyke system in the Freiberg district fits into the magma mixing discussion as presented above is unclear. One of the north-western dykes does include oscillatory zoned K-feldspar and resorbed quartz (sample M05101), but the other disequilibrium textures that were mentioned are absent in the two north-western samples. This might support the previously proposed idea of a distinct genetic history from the SBDS, but again, the difference in petrological character and the suit of samples from this dyke system are too small to draw well substantiated conclusions from.

5.5 Tectonic setting

Before going further into identifying the possible magmatic origin of the rhyolite dykes from the Freiberg district, based on the fractional crystallization and magma mixing history as discussed above, it is important to place the history of the rocks into a broad tectonic context. Based on their geochemical signature, rock classification diagrams show that all samples can be classified as A-type rhyolites, from a syn-collision to within-plate tectonic setting (Figure 32a, b). The high aluminium content of the rocks gives the rhyolites a peraluminous character (Figure 32c). Sample 84LTL provides an outlier in Figure 32a, due to its anomalously high CaO content. The within-plate, A-type and peraluminous nature of the rocks all fit with the tectonic history of the area and the presumed moment of dyke intrusion after peak metamorphism and during post-orogenic extension. However, there are also some samples in Figure 32b that plot inside the syn-collision field, including samples M05101 and M10101 from the north-western dyke system. The previously discussed fractionation of zircon could provide an explanation; Yb is a HREE and thus strongly partitioned in the zircon crystal lattice. The relatively low Yb content of the samples that plot into the syn-collision field could therefore be linked to zircon fractionation.



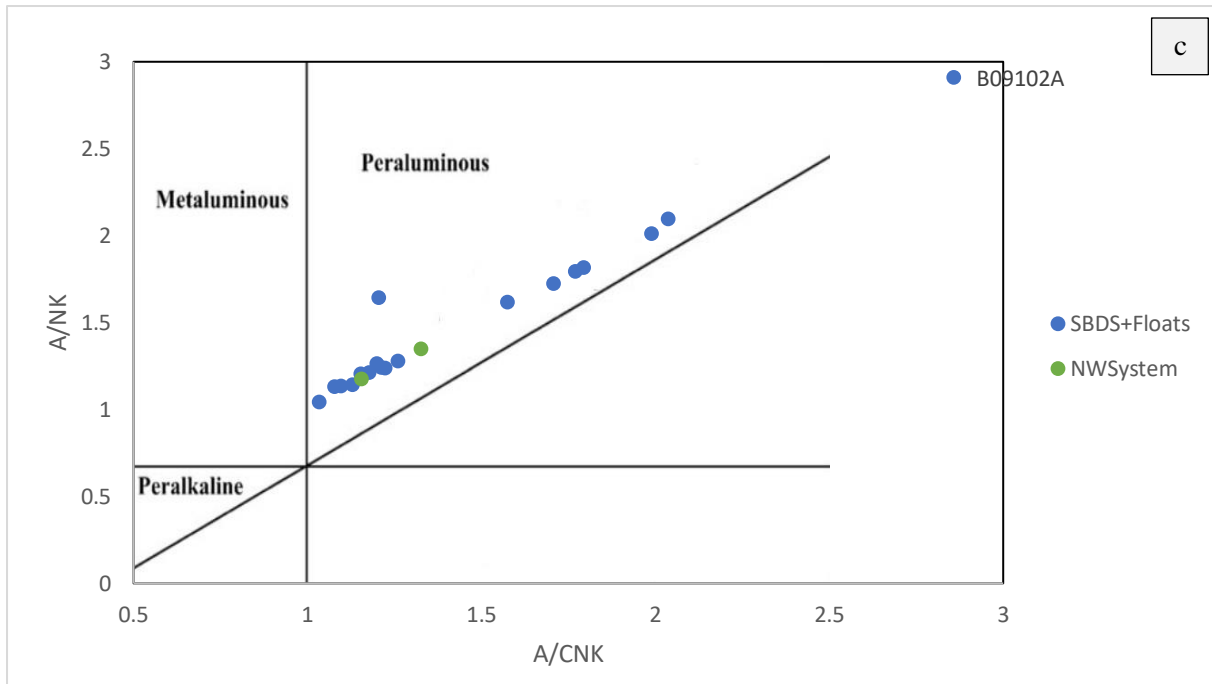


Figure 32: a) $Zr+Nb+Ce+Y$ vs. $(Na_2O+K_2O)/CaO$ granite classification diagram after Whalen et al. (1987). b) Yb vs. Ta tectonic discrimination diagram after Pearce et al. (1984). c) A/CNK vs. A/NK rock classification diagram after Shand (1943).

As discussed before in the context of alteration processes, the negative Ce anomaly in fresh granites could be inherited from a magma source that previously existed near the surface (Lee et al. (2013) and references therein). However, since the rocks from the Freiberg district can be classified as peraluminous A-type rhyolites that are emplaced in a syn- to post-collisional tectonic setting, a near-surface magma source is unlikely. Therefore the hydrothermal activity that occurred in the district after dyke emplacement is the only point that is left to discuss in context of the cause for an oxic environment and anomalous Ce behaviour, which will be done later.

5.6 Link between the Sayda-Berggiesshübel dyke swarm and the Altenberg Teplice Caldera

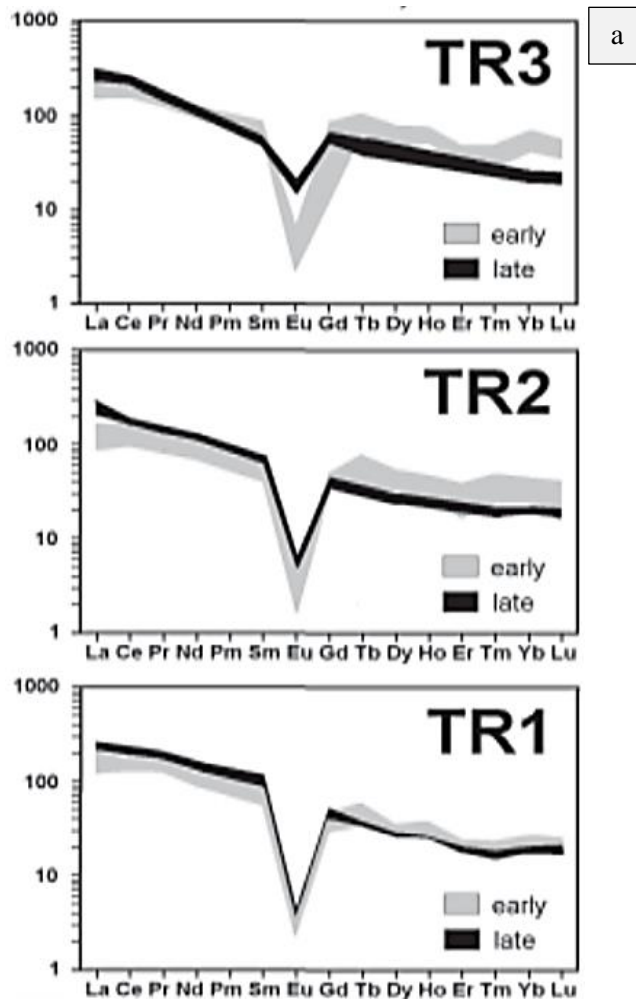
As stated before, the formation of the SBDS and the north-western dykes in the Freiberg district occurred during an episode of extensive magmatism in the region (Förster et al., 1999; Burisch et al., 2019). In this context, any link between the dykes and other igneous systems in the area could be expected. In fact, it has previously been suggested by Winter et al. (2008) that the SBDS worked as a vent and/or feeding system for the ATC, based on geochemical and structural similarities between ignimbrites from the SBDS and the ATC. This idea will now be further discussed.

Recent data review from both structural relations and U-Pb zircon dating indicates that the formation of the Teplice Rhyolite intra-caldera deposits from the ATC ranges between 325 Ma and 317 Ma (Casas-García et al., 2019). The TR comprises a diverse group of lithologies, including crystal-poor to crystal-rich rhyolitic tuffs or ignimbrites and rhyolitic lavas (Casas-García et al., 2019 and references

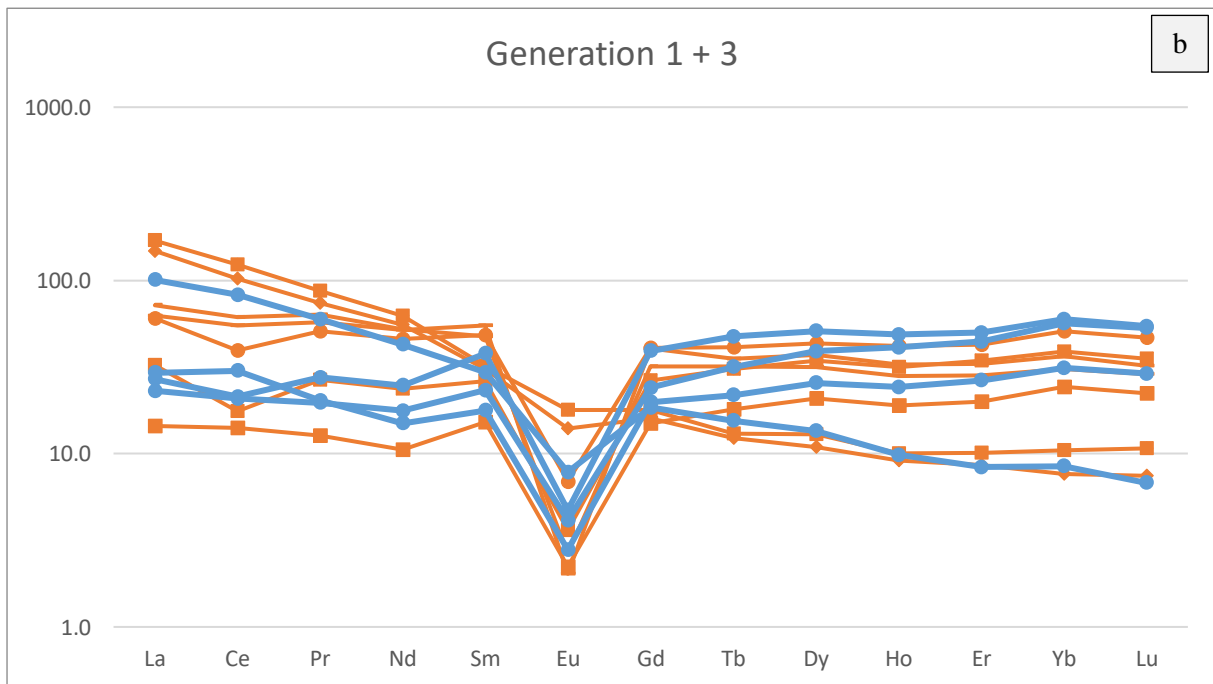
therein). According to Wetzel (1984), these rhyolitic rocks postdate the first generation of rhyolite dykes from the SBDS, but predate the second and third generation, based on structural data. Therefore, these characteristics may support the idea of Winter et al. (2008) and the dyke system could have both acted as a feeding and/or vent system of the ATC.

The SE-NW orientated flow direction for the FF-dyke, as determined by Freyemark et al. (2015) and as previously discussed, provides another indicated of a possible genetic relation of the SBDS to the ATC, since the ATC is located south-east of this large dyke (Figure 2). Also the transition from a phenocryst-rich rhyolite type in the south-eastern part of the FF-dyke to a phenocryst-poor rhyolite type in the north-western part of the FF-dyke could be linked to a difference in magma cooling rate as a function of the distance to the magma reservoir underneath the ATC. Similarly, the contact of the rhyolite and host gneiss at sampling site B09101, B09102, with a SE dipping orientation, could also be linked to this idea of the location of the magma source.

Furthermore, Breiter et al. (2001) found that the TR consists of three independent rhyolitic units that represent three different eruption cycles. All three units show a similar chemical trend from relatively more evolved rocks at the bottom to less evolved rhyolites at the top (Figure 33a), which will be further discussed later on (Breiter et al., 2001). In general, the REE patterns strongly resemble the REE patterns from the SBDS (Figure 32b). Also, Breiter (2012) found that the TR contains slightly peraluminous A-type rhyolites, similar to the rocks from the SBDS. In addition, the slightly peraluminous rocks from the TR have very low phosphorus contents (below 0.05 wt.%) (Breiter, 2012), as do the samples from this study (Table 3). All these facts support the possible genetic link between the SBDS and the ATC. However, the A-type rhyolites from the ATC show an increase in Pb content with increasing fractionation, which is in contrast with the rocks from the SBDS (Figure 27).



a



b

Figure 33: a) Chondrite normalised REE patterns of the three eruption cycles of the TR (normalization values from Henderson et al. 1984). From Breiter et al. (2001). b) Chondrite normalized REE patterns of the first (red) and third (blue) generations of the SBDS. Plotted for comparison.

Accessory minerals such as zircon may contain information to further investigate the link between the SBDS and the ATC. Zircons are common in all felsic igneous rocks in the Erzgebirge (Breiter, 2012). However, the A-type rhyolites from the ATC contain zircon that is particularly rich in Th, Y, Yb and sometimes As (Breiter, 2012; Breiter et al., 2014). Also transition phases of zircon, thorite and xenotime are common in the more fractionated A-type rocks, probably linked to fast cooling of some intrusions (Breiter, 2012). In contrast, zircons from other, felsic S-type lithologies in the Erzgebirge, are usually rich in P, U and Al and poor in Th, Y and Yb (Breiter, 2012). In future work, microprobe analysis of the zircons from the SBDS could thus be interesting.

Another strong indication for a genetic relation between the SBDS and the ATC is found in the disequilibrium textures that indicate magma mixing, as discussed above. The magma chamber that worked as a source for the TR was chemically zoned and presumably involved some form of magma mixing, as indicated by similar disequilibrium textures in the TR as for the SBDS, such as sieve textured plagioclase and resorbed quartz (Müller et al., 2005; 2010). This magma mixing most likely occurred in the form of self-mixing (i.e. closed-system mixing) in the stratified chamber due to ponding of hotter, isotopically similar magma (Casas-García et al., 2021), which will be further discussed below. The zoned magma chamber yielded the normally zoned volcanic complex, with the three rhyolites including a trend from evolved to less evolved phases for each eruption cycle (Müller et al., 2005; Casas-García et al., 2021). Since the rhyolite dykes from the SBDS in the Freiberg district are hypothesized to have acted as a complex feeding/vent system for the rhyolitic magma of the ATC (Winter et al., 2008; Casas-García et al., 2019) the difference in the geochemical content of the dykes and the variable degree of magma evolution within each dyke generation could be related to the stratified magma chamber of the ATC. This is also reflected in the previously discussed similarity between the dyke generations in the Harker diagrams (Figure 27). Also the fact that Winter et al. (2008) found evidence for magma-mixing with a more intermediate melt at the rhyolite dome of Rötherbacher berg, could fit into this picture. In addition, Couch et al. (2001), who investigated the process of convective self-mixing in a magma chamber, determined that this mechanism can cause all disequilibrium textures as found in the samples from the SBDS (and the ATC (Casas-García et al., 2021)). In this context, further investigation of the resorbed and possibly zoned quartz phenocrysts in the SBDS could also provide further information about the relation between the dyke swarm and the ATC.

Casas-García et al. (2021) suggested a model for the large scale structure of the magma reservoir of the ATC, based on their geochemical and petrological findings. They build upon the work of Müller et al. (2005), who investigated the Schellerhau granite, one of the volcanic units in the ATC. Müller et al. (2005) found that the Schellerhau granite is highly fractionated and does not show any signs of magma mixing, hence it does not include any previously mentioned disequilibrium textures. However, the Schellerhau granite does contain one type of zoned quartz phenocrysts that is also present in the other

ATC units and thus indicates a genetic relationship (Müller et al., 2005). Their explanation for this is a deeper magma reservoir beneath the ATC that was not affected by the mixing event. Casas-García et al. (2021) adopt this idea, since they do not find any evidence for magma mixing with a mafic magma in the ATC deposits, but they do find an indication of a heterogeneous/intermediate magma source in the isotopic fingerprints of the rocks. This is likely due to a combination in protolith of deeper and shallower located source rocks and reservoirs in the middle-crust and upper-crust, that were melted by dehydration melting and heat advection (Casas-García et al., 2021). Disequilibrium textures, like the resorbed quartz and mantled feldspar, could then be formed by self-mixing in the lower parts of the shallower magma chamber induced by the ponding of hotter magma, ascending from the deeper reservoir (Casas-García et al., 2021) (Figure 34). This could also explain why Müller et al. (2008) could not find any isotopical evidence for magma mixing in the zoned quartz and mantled feldspar they investigated from the ATC and interpreted to be caused by mafic magma addition to the felsic source. Since the SBDS does show similar disequilibrium textures as the ATC lithologies, it could be derived that the magma source of the dykes was related to the shallower magma chamber of the ATC rather than a deeper/other reservoir.

It is important to note that the exact timing of dyke formation is still not exactly known. The geochronological data, that is currently being obtained, may shed new light on the relation between the ATC and the SBDS.

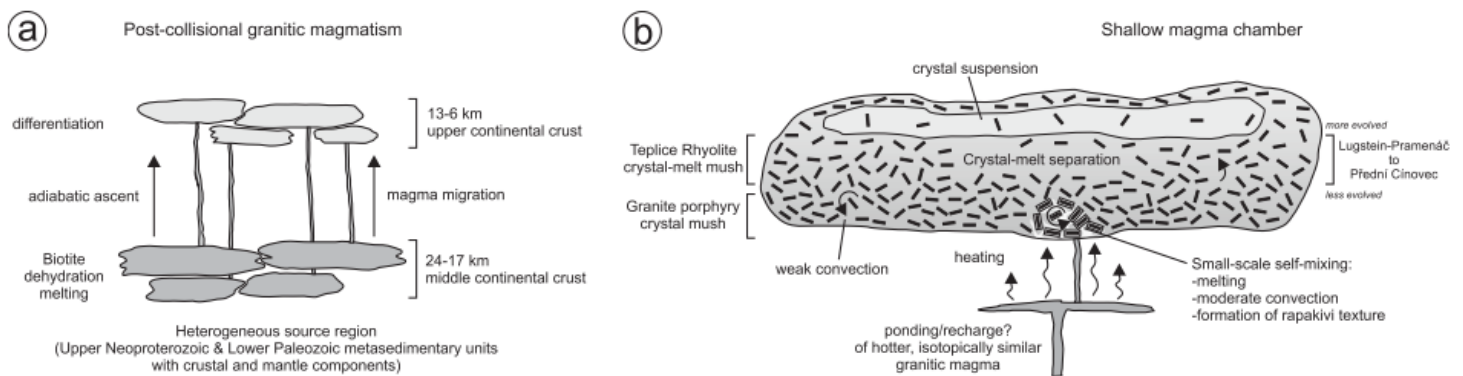


Figure 34: Conceptual model of the origin and evolution of the chemically zoned TR of the ATC. a) Overview of the two-level magma storage for the granites of the Erzgebirge. b) Sketch of the magma chamber for the TR. From Casas-García et al. (2021).

It remains difficult to say something about how the north-western dykes of the Freiberg district fit into this story of the link between the SBDS and ATC. For the most part, the old German geological literature about the area is inaccessible and/or includes no clear arguments about these dykes. The geological map of Wetzel (1984) (and therefore also the corresponding geochemical data) suggests that the two dyke systems from this study have different source intrusions and that the north-western dykes have a more intermediate composition (Figure 35). However, the geochemical data from samples M05101 and M10101, with >78% SiO₂ for both rocks, does not indicate a more intermediate composition. Therefore, more work is required to test this theory.

Legend



-  Rhyolite, igneous rocks from the older post-kinematic complexes from the Erzgebirge
-  Rhyolite to dacite dykes, derived from plutonic intrusions with no link to igneous complexes

Figure 35: Translated part of the legend from the geological map of Wetzel (1984). Samples from the SBDS are classified as upper legend unit in the figure, samples M05101 and M10101 from the north-western dykes are classified as lower legend unit in the figure.

5.7 Link to hydrothermal system

In addition to broad dyke characterization and determining magma evolution, this thesis also has the goal to identify whether there is a link between the rhyolite dykes of the Freiberg district and the regional hydrothermal system. Therefore, it is important that, even though the exact timing of the formation of the SBDS is unknown, the upper time constraint for the emplacement of the rocks is given by the end of the large scale magmatism in the Erzgebirge around 295 Ma (Förster et al., 1999; Burisch et al., 2019). This means that the dykes have formed prior to the extensive hydrothermal vein mineralization that started around 280 Ma (Bauer et al., 2019; Burisch et al. 2019). Any hydrothermal influence on the dykes' composition and/or textural characteristics could thus be expected. In this context, the abundant sericitic alteration in the matrix and feldspar phenocrysts in the rhyolite dykes of the SBDS (Figure 6f) may be important. Sericitic alteration of granitic rocks has often been linked to hydrothermal influences (e.g. Alderton et al., 1980; Juliani et al., 2002; Li et al., 2013). In fact, further south-west of the Freiberg district, the Erzgebirge hosts the Eibenstock granite that has been intruded by rhyolite stocks and dykes (Kempe et al., 2004 and references therein). Both the granite and the rhyolites have been hydrothermally altered and are, as a consequence, affected by sericitization and greisenization (Kempe et al., 2004). Similarly to the Freiberg district, the sericitic alteration has mainly affected the glassy matrix and feldspar phenocrysts in the rhyolites and the hydrothermal activity has caused the formation of polymetallic ore veins (Kempe et al., 2004).

Furthermore, the source intrusion for the hydrothermal system in the area around Freiberg is still unknown, but the relatively low salinity of the fluid that formed the hydrothermal ores is typical for distal magmatic-hydrothermal systems that occur up to 6 km away (Swinkels et al., 2021). Therefore, the rhyolite dykes of the SBDS may have influenced and/or accommodated the fluid pathways in the Freiberg district due to a possible contrasting permeability to the host rock and thereby got affected by the hydrothermal activity, as is also concluded for the rhyolitic dykes in the hydrothermal system of the Taupo Volcanic Zone in New Zealand (Rowland & Sibson, 2004).

However, in contrast to the clear sericitization in the petrological features of the rhyolites from the south-western Erzgebirge, Kempe et al. (2004) do not see clear signs of this alteration process in the geochemistry of their samples. Their indisputable evidence for hydrothermal alteration of the rocks is

provided by the unambiguous petrological and geochemical indications of greisenization. In contrast, there is no sign of any greisenization in the dykes from the Freiberg district and no clear indication of strong hydrothermal influences on the geochemical pattern in the rocks, apart from one geochemical feature. Only the (slightly) anomalous behaviour of Ce in the REE pattern of some samples (M04104A, M04104B, B09101, B05105, B07101B and B09104) could indicate a link to the hydrothermal system. Due to the previously discussed redox sensitivity of the element, it can behave differently from other REEs. Therefore, it is possible that due to hydrothermal activity, oxidation – reduction transformations occur and mostly Ce is leached out of the system (resulting in a negative anomaly) or all other REEs are leached out and Ce stays behind (resulting in a positive anomaly). In addition, in the samples that display anomalous Ce behaviour, there is no link between the measured LOI values and the strength and/or nature of this anomaly. Therefore, weathering processes as a cause for the change in oxidation state of Ce, as previously discussed, seem unlikely.

Despite anything to the contrary, there is still another possible explanation for the Ce anomaly. This explanation requires coming back to the fractionation of accessory minerals such as monazite. In the most common endmember of the accessory mineral monazite ($\text{REE}(\text{PO}_4)$), Ce is included in the crystal structure, which could then be replaced by other LREEs to form other, rare endmembers. At first glance the Ce Harker plot mainly shows scattered data. However, this scatter is mostly caused by floatstone samples and the samples that were taken in situ actually form a negative correlation up to the point of 78% silica, possibly caused by monazite fractionation. The same pattern can be observed in the Harker diagram that plots the total REE concentration as previously mentioned. In fact, the Ce anomaly that is observed in the REE pattern of some samples and in all these samples coincides with a relatively low LREE content, could thus be another indication of accessory mineral, or to be more specific, monazite fractionation. Even more so, since in peraluminous granites, monazite is a common accessory phase that has been previously studied in the Erzgebirge due to its abundance and diverse composition in the area (Förster, 1998; Breiter & Förster, 2021).

Overall, based on the strong sericitization in the rhyolitic rocks, together with their origin in the centre of a vast hydrothermal system, some chemical and petrological characteristics of the rhyolite dykes in the Freiberg district are likely related to hydrothermal influences. Also, the slightly anomalous behaviour of Ce in some samples could be a result of the regional hydrothermal overprint. However, since this chemical alteration that may result from this hydrothermal process is only small and could also be explained by fractional crystallization processes, there is no indisputable evidence that the regional hydrothermal activity affected the rhyolite dykes from the SBDS.

Also, note that the two samples from the north-western dykes in the Freiberg district do not include any sericite (Appendix 4). This provides yet another indication for a contrasting emplacement and/or alteration history to the SBDS. To further investigate this contrast between the north-western dykes and the SBDS and to further investigate the general link between the rhyolite dykes and the

hydrothermal activity in the Freiberg district, more research is required such as chemical analysis of fluid inclusions.

6. Conclusions

The numerous rhyolite dykes in the Freiberg district that were analysed in this study, including part of the SBDS and a dyke system located further to the north-west of Freiberg, have an interesting geological history. Despite poor exposure in the field and a weathered appearance of multiple samples, analysis of weathering features and assessment of the degree of weathering of the rocks has indicated that primary rock composition and texture were not significantly influenced by weathering processes. Mineralogical and petrological analysis has yielded that the dykes have a typical rhyolitic mineralogical composition of quartz, plagioclase, K-feldspar, mica and some opaque minerals, with a strong variation in matrix percentage and modal mineral abundances. This rhyolitic composition is also reflected in their major geochemical signature. In addition, the geochemical content of the dykes features a strong variation, with variable trace element and REE patterns that represent variable degrees of source magma evolution. Harker diagrams show fractionation trends of the typical rhyolitic rock forming minerals such as plagioclase and K-feldspar, but together with the REE patterns and TTSEM analysis also provide evidence for fractional crystallization of accessory minerals during magma evolution. The negative correlation trends in the Zr and Hf Harker diagrams and HREE depletion that is featured in many samples indicate the importance of zircon fractionation for both the SBDS and the north-western dykes. The fact that zircons were identified under the TTSEM for several samples of the first generation of the SBDS is consistent with this geochemical pattern. Similarly, the MREE depletion in some samples, the negative correlation pattern in the TiO_2 Harker diagram and the identification of titanite and/or rutile crystals in generations one and three of the SBDS and the north-western dykes under the TTSEM, indicates the important role of fractionation of these minerals during the magmatic history of the rocks. Apart from zircon, titanite and rutile, no other accessory minerals were identified under the TTSEM. Nevertheless, the LREE depletion in the REE pattern of some samples and the negative correlation pattern in the P_2O_5 Harker diagram strongly suggest that late stage fractionating minerals such as allanite and/or monazite are also important in the fractional crystallization history of the dykes from the Freiberg district. In addition to mineral fractionation trends for the total SBDS, Harker diagrams also show that for the individual dyke generations one and three, similar fractionation trends can be applied.

Parallel to the story of fractional crystallization in the magmatic origin of the dykes runs the story of magma mixing in the magma source. Several mineralogical textures that are featured in the rhyolite dykes, such as abundant quartz resorption, oscillatory zoned K-feldspar and sieve textured K-feldspar are interpreted as representing disequilibrium textures that could be caused magma mixing. The outcrop-scale ductile deformation structures as identified in the open pit mine at the R othenbacher Berg could support an event of mixing during the magmatic history of the dykes and was, in fact, in previous work interpreted to represent such an event.

The combination of the fractional crystallization and magma mixing processes as outlined above have yielded rhyolite dykes with an A-type affinity and peraluminous characteristics, that were emplaced in an extensional regime during orogenic collapse of the Erzgebirge. In this context, many of the geochemical and petrological characteristics that define the dykes in the Freiberg district, similarly define the TR that forms part of the ATC which also formed during the Permian orogenic collapse of the Erzgebirge. Similarly to how the SBDS consists of three slightly peraluminous dyke generations, the TR consists of slightly peraluminous rhyolites that were formed during three eruption cycles. In both the SBDS and the TR, these generations/cycles all include a range in geochemical content with different degrees of evolution. Also, the disequilibrium textures that are found in the SBDS and may represent magma mixing during magma evolution have also been identified in the TR and been linked to the magma mixing process. In addition, structural characteristics such as the SE-dipping contact between a rhyolite dyke from the SBDS and the host gneiss, the north-western flow direction of the FF-dyke and the fact that the FF-dyke has a decrease in phenocryst content away from the ATC could support the idea of a link between the SBDS and a magma source underneath the caldera.

How the north-western dykes, that are not part of the SBDS, fit into the geological history of the Freiberg district remains difficult to say. These dykes may have been formed during a (partly) separate magmatic history, based on their particularly strong MREE depletion in comparison to the other dykes from the area, indicating a particularly important role of titanite fractionation. Unfortunately, the suite of samples from this dyke system remains small and in terms of magma evolution there are no other indications of a significant difference between the SBDS and the north-western dykes.

To further investigate the relation between the SBDS and other rhyolite dykes in the Freiberg district, and the possible relation between the rhyolite dykes and the ATC, more work needs to be done.

After the magmatic and emplacement history that formed (part of) the petrological and geochemical characteristics of the rhyolite dykes from the Freiberg district, any alteration processes may also have been of influence. Apart from weathering processes that undoubtedly affected the rocks after formation but were determined to be insignificant in terms of rock geochemistry, hydrothermal alteration processes may have been important. A key factor that suggests a link between the rhyolite dykes and the famous hydrothermal system from the Freiberg district may be the sericitized minerals that are featured in the rocks; sericitic alteration has often been linked to hydrothermal influences. The anomalous behaviour of Ce that is common in the samples from this study could also be linked to hydrothermal alteration, due to the strong influence of these processes on redox conditions that affect Ce concentrations. However, fractional crystallization of accessory minerals might provide a sufficing explanation for the Ce anomaly in the REE pattern. Therefore, more research is required to accurately identify and/or define the link between the rhyolite dykes and hydrothermal system of the Freiberg district.

7. Acknowledgements

Special thanks to Manuel Lapp from the Geological Survey of Freiberg, for enthusiastic thinking along with this project and providing samples and literary material from the Geological Archive of Freiberg. Also thanks for the delicious quince pie and beautiful bike ride around the city.

I would like to extend my thanks to my supervisors Prof. Paul Mason from Utrecht University and Prof. Mike Buxton and Dr. Feven Desta from the TU Delft for guiding me through the project. Lastly, also many thanks to Dr. Mathias Burish from the TU Freiberg for providing the idea for this research. This research project was supported by the Olaf Schuilingfonds of Utrecht University Fund.

8. References

- Alderton, D. H. M., Pearce, J. A. and Potts, P. J. (1980) 'Rare Earth Element Mobility during Granite Alteration: Evidence from Southwest England', *Earth and Planetary Science Letters*, 49, pp. 149–165.
- Baldridge, A. M., Hook, S. J., Grove, C. I. and Rivera, G. (2009) 'The ASTER Spectral Library Version 2.0. Remote Sensing of Environment', vol 113, pp. 711-715.
- Bauer, M. E., Burisch, M., Ostendorf, J., Krause, J., Frenzel, M., Seifert, T. and Gutzmer, J. (2019) 'Trace element geochemistry of sphalerite in contrasting hydrothermal fluid systems of the Freiberg district, Germany: insights from LA-ICP-MS analysis, near-infrared light microthermometry of sphalerite-hosted fluid inclusions, and sulfur isotope geochemi', *Mineralium Deposita*. Springer Verlag, 54(2), pp. 237–262. doi: 10.1007/S00126-018-0850-0.
- Blake, R.L., Hessevick, R.E., Zoltai, T., and Finger, L.W. (1966) 'Refinement of the hematite structure', *American Mineralogist*, 51, pp. 123-129.
- Bowen, N. L. (1922) 'The Reaction Principle in Petrogenesis', *The Journal of Geology*, 30(3), pp. 177–198. doi: 10.1086/622871.
- Breiter, K., Förster, H. J. and Seltmann, R. (1999) 'Variscan silicic magmatism and related tin-tungsten mineralization in the Erzgebirge-Slavkovsky les metallogenic province', *Mineralium Deposita*, 34(5–6), pp. 505–521. doi: 10.1007/s001260050217.
- Breiter, K., Novák, J. and Chlupáčová, M. (2001) 'Chemical evolution of volcanic rocks in the Altenberg-Teplice Caldera (Eastern Krušné hory Mts., Czech Republic, Germany)', *Geolines*, 13, pp. 17–22. Available at: <http://geolines.gli.cas.cz/fileadmin/volumes/volume13/G13-017.pdf> (Accessed: 17 July 2021).
- Breiter, K. (2012) 'Nearly contemporaneous evolution of the A- and S-type fractionated granites in the Krušné hory/Erzgebirge Mts., Central Europe', *Lithos*. Elsevier, 151, pp. 105–121. doi: 10.1016/j.lithos.2011.09.022.
- Breiter, K. and Förster, H. J. (2021) 'Compositional variability of monazite–cheralite–huttonite solid solutions, xenotime, and uraninite in geochemically distinct granites with special emphasis to the strongly fractionated peraluminous li–f–p-rich podlesí granite system (Erzgebirge/krušné hor)', *Minerals*. Multidisciplinary Digital Publishing Institute, 11(127), pp. 1–21. doi: 10.3390/min11020127.
- Breiter, K., Lamarão, C. N., Borges, R. M. K., Dall'Agnol, R. (2014) 'Chemical characteristics of zircon from A-type granites and comparison to zircon of S-type granites', *Lithos*. Elsevier B.V., 192–195, pp. 208–225. doi: 10.1016/j.lithos.2014.02.004.
- Burisch, M., Frenzel, M., Seibel, H., Gruber, A., Oelze, M., Pfänder, J. A., Sanchez-Garrido, C. and Gutzmer, J. (2021) 'Li-Co–Ni-Mn-(REE) veins of the Western Erzgebirge, Germany—a potential source of battery raw materials', *Mineralium Deposita*. Springer Berlin Heidelberg. doi: 10.1007/s00126-021-01061-4.

Burisch, M., Hartmann, A., Bach, W., Krolow, P., Krause, J. and Gutzmer, J. (2019) 'Genesis of hydrothermal silver-antimony-sulfide veins of the Bräunsdorf sector as part of the classic Freiberg silver mining district, Germany', *Mineralium Deposita*, 54(2), pp. 263–280. doi: 10.1007/s00126-018-0842-0.

Carl, B. and Glazner, A. (2002) 'Extent and significance of the Independence dike swarm, eastern California', *Geological Society of America, Memoir*, 195, pp. 117–130. doi: 10.1130/0-8137-1195-9.117.

Casas-García, R., Rapprich, V., Breitzkreuz, C., Svojtka, M., Lapp, M., Stanek, K., Hofmann, M. and Linnemann, U. (2019) 'Lithofacies architecture, composition, and age of the Carboniferous Teplice Rhyolite (German–Czech border): Insights into the evolution of the Altenberg-Teplice Caldera', *Journal of Volcanology and Geothermal Research*, 386, pp. 1–22. doi: 10.1016/j.jvolgeores.2019.106662.

Casas-García, R., Rapprich, V., Repstock, A., Magna, T., Schulz, B., Erban Kochergina, Y. V. and Breitzkreuz, C. (2021) 'Crustal vs. mantle contributions in the Erzgebirge/Krušné hory Mts. magmatism: Implications for generation of zoned, A-type silicic rocks in the late-Variscan Altenberg-Teplice Caldera, Central Europe', *Lithos*, 404–405(8), pp. 1–18. doi: 10.1016/j.lithos.2021.106429.

Couch, S., Sparks, R. S. J. and Carroll, M. R. (2001) 'Mineral disequilibrium in lavas explained by convective self-mixing in open magma chambers', *Nature*, 411(6841), pp. 1037–1039. doi: 10.1038/35082540.

Dini, A., Westerman, D. S., Innocenti, F. and Rocchi, S. (2008) 'Magma emplacement in a transfer zone: the Miocene mafic Orano dyke swarm of Elba Island, Tuscany, Italy', *Geological Society, London, Special Publications*, 302, pp. 131–148. doi: 10.1144/SP302.10.

Ernst, R. E., Grosfils, E. B. and Mège, D. (2001) 'Giant Dike Swarms: Earth, Venus, and Mars', *Annu. Rev. Earth Planet. Sci*, 29, pp. 489–534. Available at: www.annualreviews.org (Accessed: 4 February 2022).

Esri. "Topographic" [basemap]. Scale Not Given. "World Topographic Map". August 3, 2021. <http://www.arcgis.com/home/item.html?id=30e5fe3149c34df1ba922e6f5bbf808f>. (April 12, 2022).

Förster, H. J., Tischendorf, G., Trumbull, R. B. and Gottesmann, B. (1999) 'Late-collisional granites in the Variscan Erzgebirge, Germany', *Journal of Petrology. Oxford Academic*, 40(11), pp. 1613–1645. doi: 10.1093/petroj/40.11.1613.

Förster, H. J. (1998) 'The chemical composition of REE-Y-Th-U-rich accessory minerals in peraluminous granites of the Erzgebirge-Fichtelgebirge region, Germany, Part I: The monazite-(Ce)-brabantite solid solution series', *American Mineralogist*, 83(3–4), pp. 259–272. doi: 10.2138/am-1998-3-409.

Förster, H. J., Ondrejka, M. and Uher, P. (2011) 'Mineralogical responses to subsolidus alteration of granitic rocks by oxidizing As-bearing fluids: REE arsenates and As-rich silicates from

the Zinnwald granite, Eastern Erzgebirge, Germany', *Canadian Mineralogist*, 49(4), pp. 913–930. doi: 10.3749/canmin.49.4.913.

Freyemark, J., Lapp, M., Breitzkreuz, C., Altenberger, U., Stanek, K. and Grund, K. (2015) 'Texture and geochemistry of the Late Paleozoic Freiberg-Frauenstein rhyolite dike (East Erzgebirge, Saxony): flow differentiation vs. magma composition', *Jahresberichte und Mitteilungen des Oberrheinischen Geologischen Vereins*, 97, pp. 269–300. doi: 10.1127/jmogy/97/0012.

Gatti, A. (2022) 'An integrated analysis of infrared and X-ray fluorescence technologies for enhanced characterization of minerals from various deposits', BSc-thesis, TU Delft.

Ginibre, C., Kronz, A. and Wörner, G. (2002) 'High-resolution quantitative imaging of plagioclase composition using accumulated backscattered electron images: New constraints on oscillatory zoning', *Contributions to Mineralogy and Petrology*, 142(4), pp. 436–448. doi: 10.1007/s004100100298.

Hibbard, M. J. (1981) 'The magma mixing origin of mantled feldspars', *Contributions to Mineralogy and Petrology*, 76(2), pp. 158–170. doi: 10.1007/BF00371956.

Hogan, J. P. (1993) 'Monomineralic Glomerocrysts: Textural Evidence for Mineral Resorption During Crystallization of Igneous Rocks', *The Journal of Geology*, 101, pp. 531–540.

Hoth, K., Wasternack, J., Berger, H.-J., Breiter, K., Mlcoch, B. and Schovánek, P. (1995) 'Geologische Karte Erzgebirge/Vogtland', 1:100000. Sachsisches Landesamt für Umwelt und Geologie Freiberg.

Juliani, C., Corrêa-Silva, R. H., Monteiro, L. V. S., Bettencourt, J. S. and Nunes, C. M. D. (2002) 'The Batalha Au-granite system - Tapajós Gold Province, Amazonian craton, Brazil: Hydrothermal alteration and regional implications', *Precambrian Research*, 119(1–4), pp. 225–256. doi: 10.1016/S0301-9268(02)00124-9.

Kempe, U., Bombach, K., Matukov, D., Schlothauer, T., Hutschenreuter, J., Wolf, D. and Sergeev, S. (2004) 'Pb/Pb and U/Pb zircon dating of subvolcanic rhyolite as a time marker for Hercynian granite magmatism and Sn mineralisation in the Eibenstock granite, Erzgebirge, Germany: Considering effects of zircon alteration', *Mineralium Deposita*, 39, pp. 646–669. doi: 10.1007/s00126-004-0435-y.

Kjøll, H. J., Galland, O., Labrousse, L. and Andersen, T. B. (2019) 'Emplacement mechanisms of a dyke swarm across the brittle-ductile transition and the geodynamic implications for magma-rich margins', *Earth and Planetary Science Letters*. Elsevier, 518, pp. 223–235. doi: 10.1016/J.EPSL.2019.04.016.

Kramer, (1962) Unpublished Dissertation: 'Petrographische und geochemische Untersuchung der Porphyrgänge des Freiburger Raumes', Bergakademie Freiberg (in German).

Kröner, A. and Willner, A. P. (1998) 'Time of formation and peak of Variscan HP-HT metamorphism of quartz-feldspar rocks in the central Erzgebirge, Saxony, Germany', *Contrib Mineral Petrol*, 132, pp. 1–20.

Kroner, U., Linnemann, U. and Hahn, T. (2007) 'The variscan orogeny in the saxo-thuringian zone - Heterogenous overprint of Cadomian/Paleozoic Peri-Gondwana crust', Special Paper of the Geological Society of America, 423, pp. 153–172. doi: 10.1130/2007.2423(06).

Kroner, U. and Romer, R. L. (2013) 'Two plates - Many subduction zones: The Variscan orogeny reconsidered', Gondwana Research. International Association for Gondwana Research, 24(1), pp. 298–329. doi: 10.1016/j.gr.2013.03.001.

Lafuente B., Downs R. T., Yang H., Stone N. (2015) 'The power of databases: the RRUFF project', Highlights in Mineralogical Crystallography, W. De Gruyter Berlin, Germany, 1-30.

Le Bas, M. J., Le Maitre, R. W., Streckeisen, A. and Zanettin, B. (1986) 'A Chemical Classification of Volcanic Rocks Based on the Total Alkali-Silica Diagram', Journal of Petrology, 27(3), pp. 745–750.

Lee, S. G., Asahara, Y., Tanaka, T., Lee, S. R. and Lee, T. (2013) 'Geochemical significance of the Rb-Sr, La-Ce and Sm-Nd isotope systems in A-type rocks with REE tetrad patterns and negative Eu and Ce anomalies: The Cretaceous Muamsa and Weolaksan granites, South Korea', Chemie der Erde. Elsevier GmbH., 73(1), pp. 75–88. doi: 10.1016/j.chemer.2012.11.008.

Lesaignoux, A., Fabre, S. and Briottet, X. (2013) 'Influence of soil moisture content on spectral reflectance of bare soils in the 0.4-14 µm domain', International Journal of Remote Sensing, 34(7), pp. 2268–2285. doi: 10.1080/01431161.2012.743693.

Li, L. T. (1978) Petrographische und geochemische Bearbeitung der sauren variszischen Magmatite des Erzgebirges.

Li, X. C., Fan, H. R., Santosh, M., Hu, F. F., Yang, K. F. and Lan, T. G. (2013) 'Hydrothermal alteration associated with Mesozoic granite-hosted gold mineralization at the Sanshandao deposit, Jiaodong Gold Province, China', Ore Geology Reviews. Elsevier B.V., 53, pp. 403–421. doi: 10.1016/j.oregeorev.2013.01.020.

McDonough, W. F. and Sun, S. s. (1995) 'The composition of the Earth', Chemical Geology, 120(3–4), pp. 223–253. doi: 10.1016/0009-2541(94)00140-4.

Meerdink, S. K., Hook, S. J., Roberts, D. A. and Abbott, E. A. (2019) 'The ECOSTRESS spectral library version 1.0. Remote Sensing of Environment', 230(111196), 1–8.

Middelburg, J. J., van der Weijden, C. H. and Woittiez, J. R. W. (1988) 'Chemical processes affecting the mobility of major, minor and trace elements during weathering of granitic rocks', Chemical Geology, 68(3–4), pp. 253–273. doi: 10.1016/0009-2541(88)90025-3.

Miller, C. F. and Mittlefehldt, D. W. (1982) 'Depletion of light rare-earth elements in felsic magmas', Geology, 10(3), pp. 129–133. doi: 10.1130/0091-7613(1982)10<129:DOLREI>2.0.CO;2.

Morgan, G. B. and London, D. (2012) 'Process of granophyre crystallization in the Long Mountain Granite, southern Oklahoma', GSA Bulletin, 124(7–8), pp. 1251–1261. doi: 10.1130/B30569.1.

Müller, A., Breiter, K., Seltmann, R. and Pécskay, Z. (2005) 'Quartz and feldspar zoning in the eastern Erzgebirge volcano-plutonic complex (Germany, Czech Republic): Evidence of multiple magma mixing', *Lithos*, 80(1-4 SPEC. ISS.), pp. 201–227. doi: 10.1016/j.lithos.2004.05.011.

Müller, A., Seltmann, R., Kober, B., Eklun, O., Jeffries, T. and Kronz, A. (2008) 'Compositional Zoning of Rapakivi Feldspars and Coexisting Quartz Phenocrysts', *The Canadian Mineralogist*, 46, pp. 1417–1442. doi: 10.3749/canmin.46.6.1417.

Müller, A., van den Kerkhof, A. M., Behr, H. J., Kronz, A. and Koch-Müller, M. (2010) 'The evolution of late-Hercynian granites and rhyolites documented by quartz – a review', *Earth and Environmental Science Transactions of the Royal Society of Edinburgh*, 100, pp. 185–204. doi: 10.1017/S17556909016144.

Müller, H. (1901) *Die Erzgänge des Freiburger Bergrevieres*, K. Finanz-Ministerium.

Nelson, S. T. and Montana, A. (1992) 'Sieve-textured plagioclase in volcanic rocks produced by rapid decompression', *American Mineralogist*, 77, pp. 1242–1249.

Pearce, J. A., Harris, N. B. W. and Tindle, A. G. (1984) 'Trace element discrimination diagrams for the tectonic interpretation of granitic rocks', *Journal of Petrology*, 25(4), pp. 956–983. doi: 10.1093/petrology/25.4.956.

Rowland, J. V and Sibson, R. H. (2004) 'Structural controls on hydrothermal flow in a segmented rift system, Taupo Volcanic Zone, New Zealand', *Geofluids*, 4, pp. 259–283.

Shand, S.J. (1943) 'Eruptive Rocks. Their Genesis Composition. Classification, and Their Relation to Ore-Deposits with a Chapter on Meteorite.', John Wiley & Sons, New York.

Swinkels, L. J., Frenzel, M., Schultz-Isenbeck, J. and Gutzmer, J. (2021) 'Spatial and Temporal Evolution of the Freiberg Epithermal Ag-Pb-Zn District, Germany', *Economic Geology*, 116(7), pp. 1649–1667. doi: 10.5382/econgeo.4833.

Swinkels, L., Burisch, M. and Rossberg, C. M. (2019) 'Mineralogical zoning within the Freiberg epithermal Ag-(Au)-Pb-Zn-Cu system, Germany', in *Life with Ore Deposits on Earth – 15th SGA Biennial Meeting*, pp. 342–345.

Wetzel, (1984) Unpublished Dissertation: 'Late Variscan Faulting and Subsequent Magmatic Dykes as Expression of Cortical Development in the Eastern Erzgebirge (Altenberg Block)', Zentralinstitut für Physik der Erde Potsdam, Academy of Sciences of the GDR (364 pp., in German).

Whalen, J. B., Currie, K. L. and Chappell, B. W. (1987) 'A-type granites: geochemical characteristics, discrimination and petrogenesis', *Contributions to Mineralogy and Petrology*, 95(4), pp. 407–419. doi: 10.1007/BF00402202.

Winter, C., Breitzkreuz, C. and Lapp, M. (2008) 'Textural analysis of a Late Palaeozoic coherent-pyroclastic rhyolitic dyke system near Burkertsdorf (Erzgebirge, Saxony, Germany)', *Geological Society London, Special Publications*, 302, pp. 199–221. doi: 10.1144/SP302.14.

Xu, H., Qiu, J. S., Wang, X. L., Hong, Y. F., Wang, R. Q. and Li, Y. F. (2022) 'Slow crystal settling controls the diversity of high-silica granites of the Late Cretaceous Shengsi Pluton at

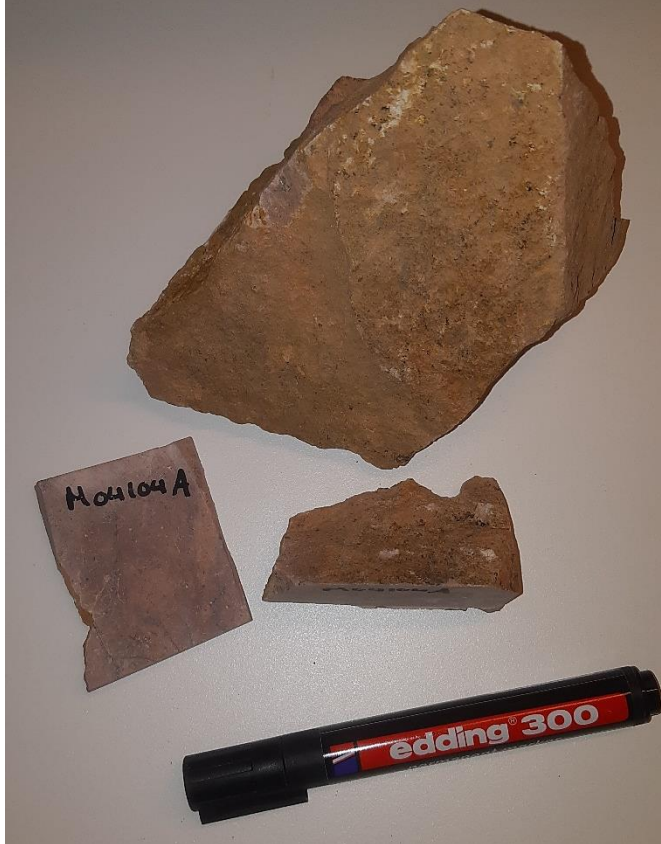

northeastern tip of southeast China', *Journal of Asian Earth Sciences*. Elsevier Ltd, 223, pp. 1–16. doi: 10.1016/J.JSEAES.2021.104986.

Yurimoto, H., Duke, E. F., Papike, J. J. and Shearer, C. K. (1990) 'Are discontinuous chondrite-normalized REE patterns in pegmatitic granite systems the results of monazite fractionation?', *Geochimica et Cosmochimica Acta*, 54(7), pp. 2141–2145. doi: 10.1016/0016-7037(90)90277-R.


Appendices

Appendix 1: Sample pictures

Table 1: Sample pictures. Marker (14 cm) and marker cap (2.8 cm) for scale.

Sample	Picture	Important notes
M04104A	 A photograph of a large, irregular, brownish-tan rock fragment. Below it are a smaller, similar fragment and a red and black marker labeled 'edding 300'. A small piece of paper with 'M04104A' written on it is also visible.	
M04104B	 A photograph of a smaller, irregular, brownish-tan rock fragment with a visible crack. Below it is a black marker labeled 'permanent marker'. A small piece of paper with 'M04104B' written on it is also visible.	Sample includes clear shear banding.

		
<p>M05101</p>		<p>Sample includes orange-weathered phenocrysts.</p>
<p>M05103</p>		<p>Sample from floatstone.</p>

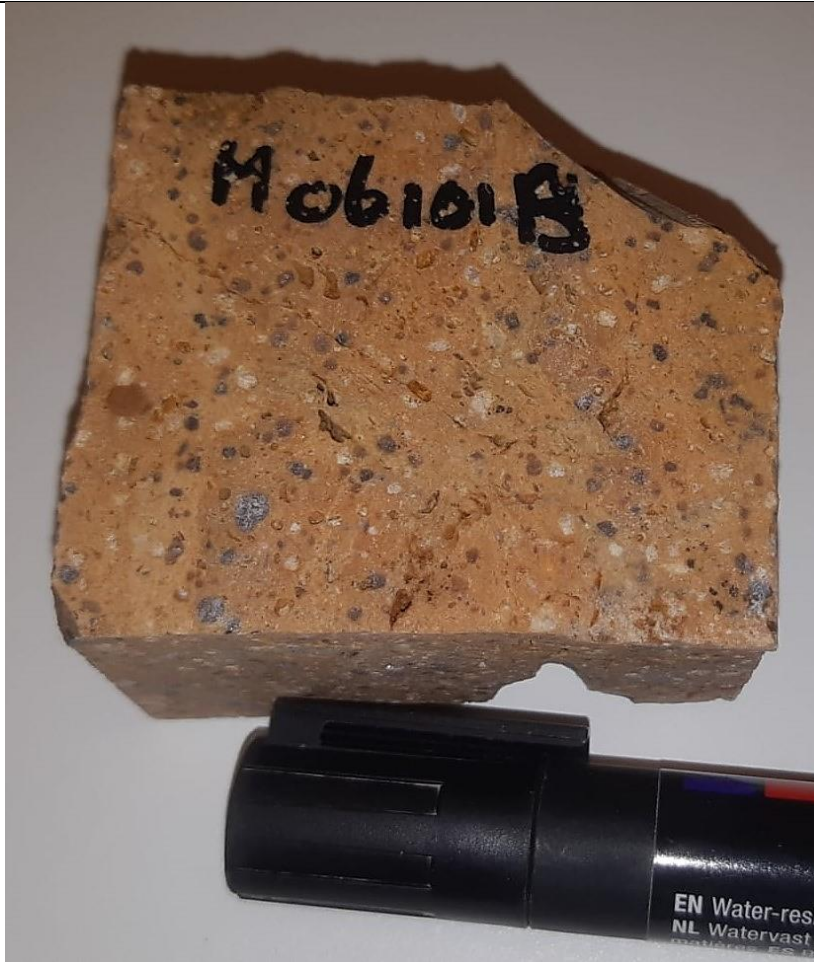
B05104		Sample from floatstone. Sample includes abundant secondary veins.
B05105		

M06101A



Sample from floatstone. Sample includes orange-weathered phenocrysts.

M06101B



Sample from floatstone. Sample may include vesicles.

B07101A



Sample from floatstone.

B07101B




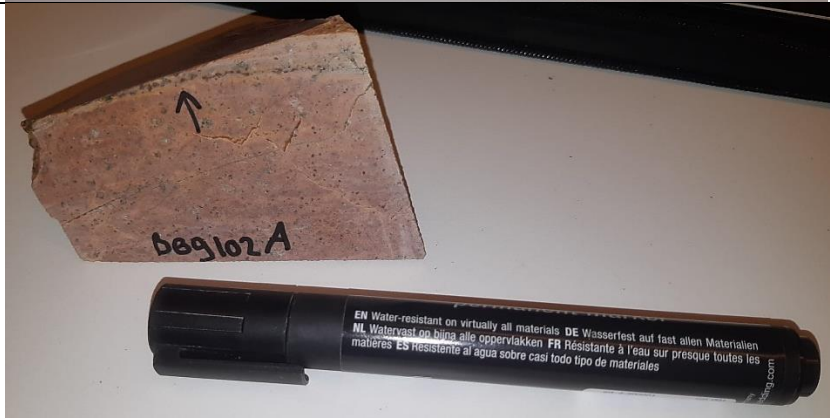
Sample from floatstone. Sample includes abundant red-altered phenocrysts.

B07102

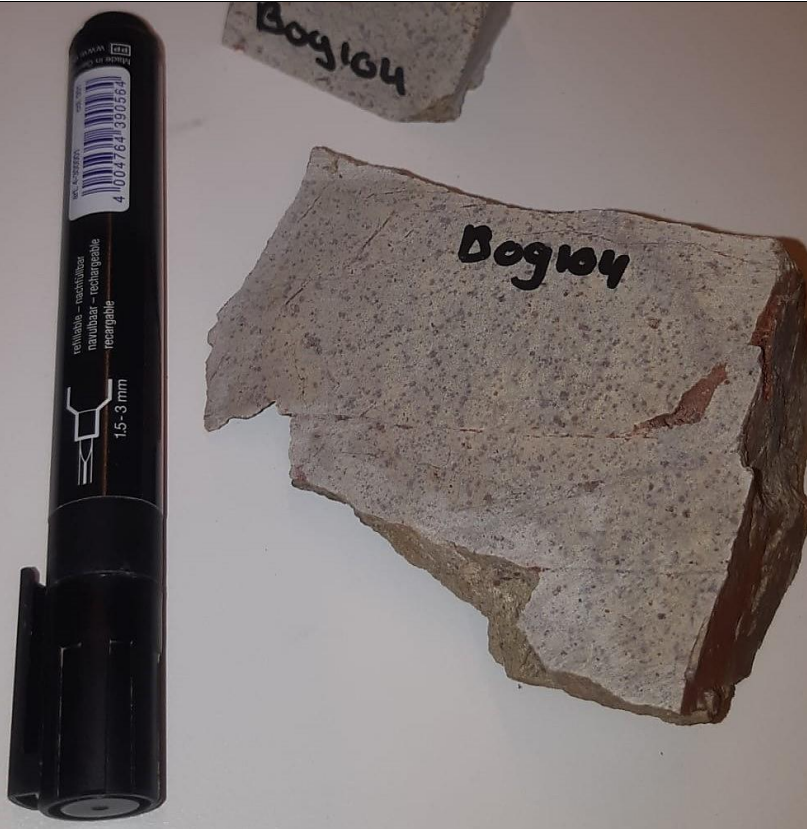


B07103



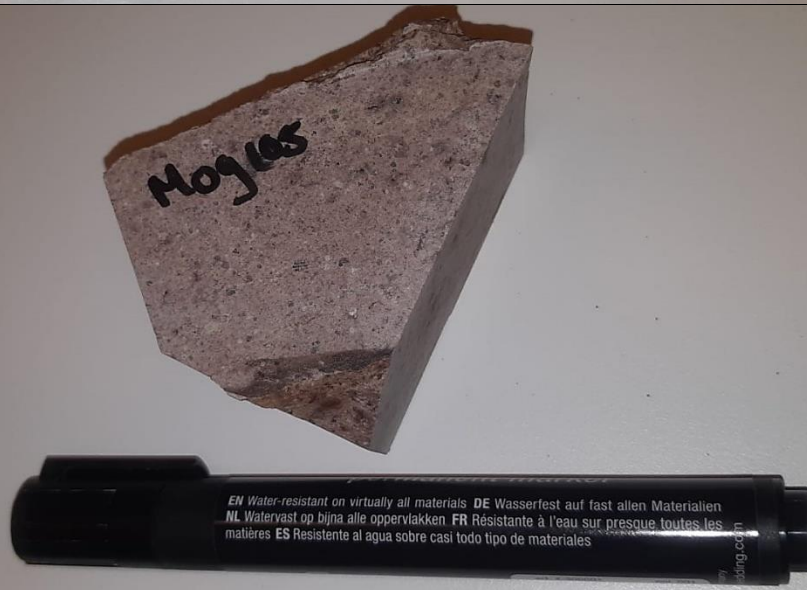
<p>B09101</p>		<p>Sample includes abundant secondary veins.</p>
<p>B09102A</p>		<p>Sample includes abundant secondary veins and alternating bands of light and darker coloured matrix.</p>

B09104



Sample from floatstone. Sample matrix has greenish colour and includes red-altered phenocrysts.

M09105



M09106



M10101



Sample includes alternating bands of light and dark coloured matrix.

84LTL



Sample has green colour.

88LTL



Sample includes bleached spots.

Appendix 2: Field measurements

Table 2: Overview of structural field measurements.

Sample	Plane	Orientation	Sample collected in orientation
M04104	Outcrop face	034/50 NE	no
B09101	Outcrop face	160/78 W	yes
	Foliation front	158/90	
	Foliation side	088/58 N	
B09102A	Contact zone	048/74 SE	no
M09105	Foliation front	130/76 SW	no
	Foliation side	170/32 W	
	Fault	dipping SE	
M09106	Foliation front	016/40 W	yes
	Foliation side	096/70 N	
M10101	Foliation front	055/90	yes
	Foliation side	164/80 E	

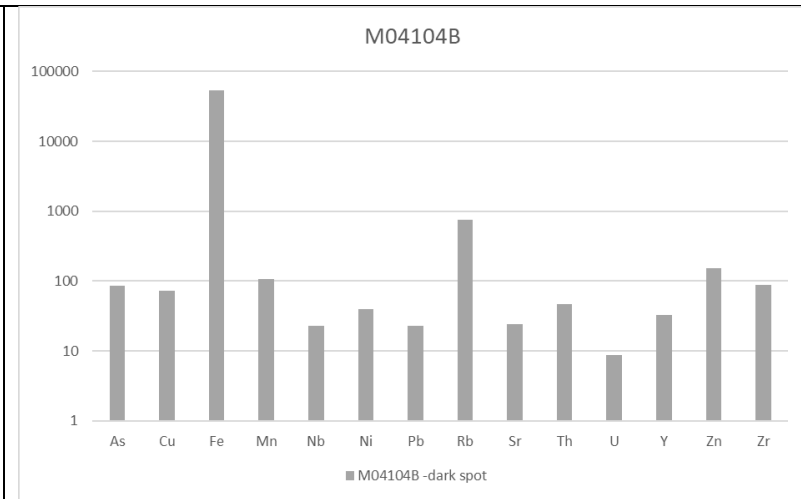
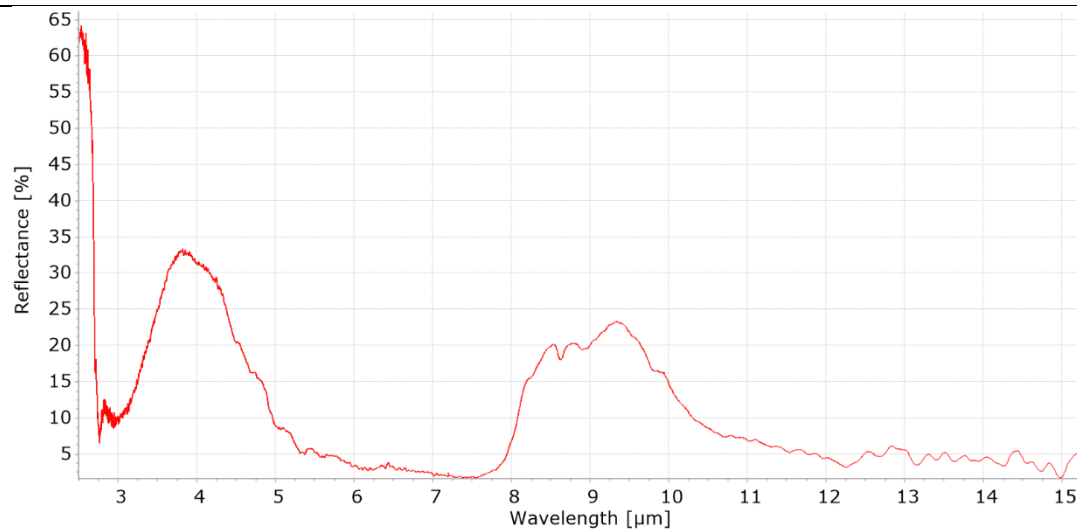
Appendix 3: FTIR spectroscopic and pXRF chemical data

For Table 3, note the logarithmic scale on the y-axis of the bar graphs. Values for chemical data are given in ppm.

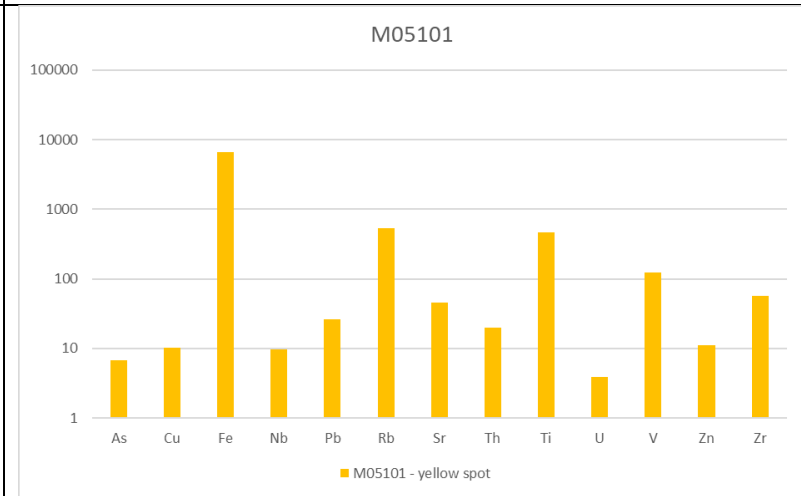
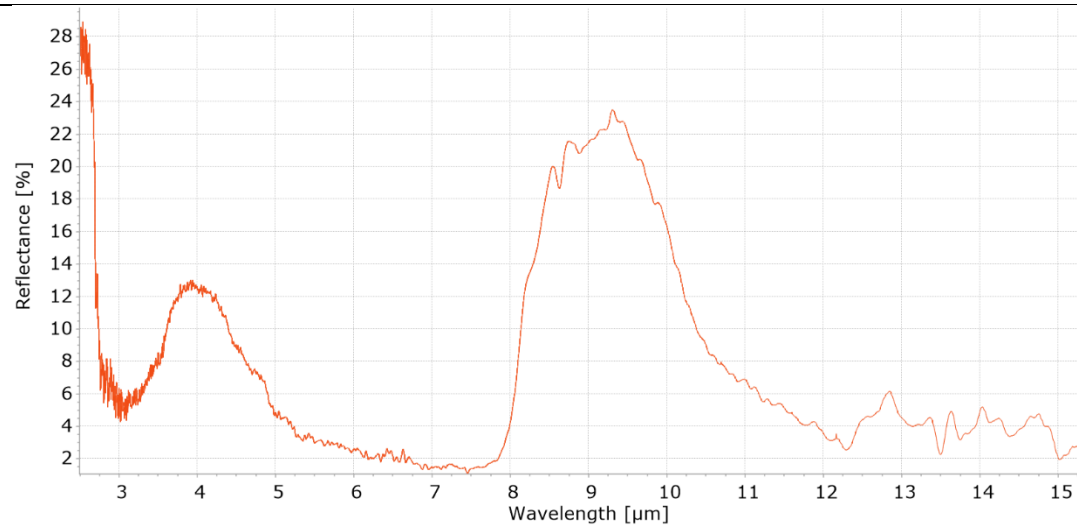
Table 3: Overview of representative pFTIR and pXRF analysis per sample.

Sample name + point description	FTIR-spectrum	pXRF data
M04104A Dark vein	<p>The FTIR spectrum shows reflectance [%] on the y-axis (5 to 35) and wavelength [µm] on the x-axis (3 to 15). Key features include a sharp peak at approximately 3.4 µm, a broad peak at 4.0 µm, a sharp peak at 8.2 µm, and a very sharp peak at 9.1 µm. The reflectance is generally low (below 10%) between 5 and 10 µm.</p>	<p>The pXRF data bar chart shows the concentration of various elements in ppm for sample M04104A - dark vein. The y-axis is logarithmic, ranging from 1 to 100,000 ppm. The elements and their approximate concentrations are: As (~5), Cu (~15), Fe (~15,000), Mn (~70), Nb (~25), Pb (~15), Rb (~400), Sr (~20), Th (~40), U (~5), Y (~35), Zn (~80), and Zr (~90).</p>

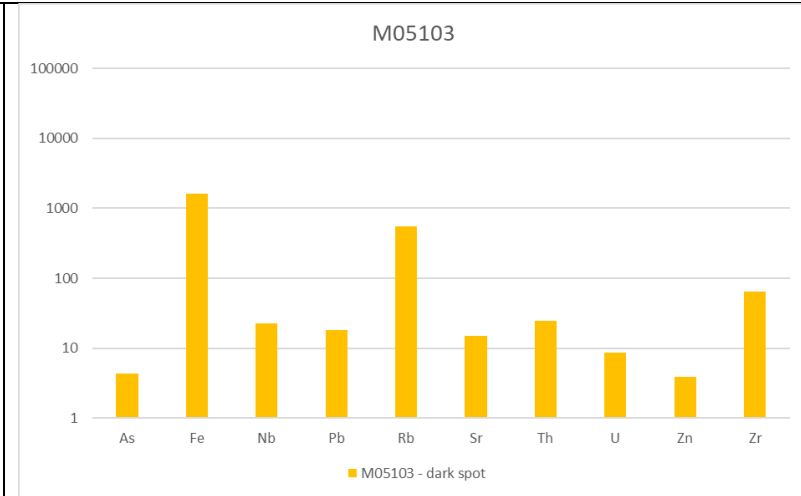
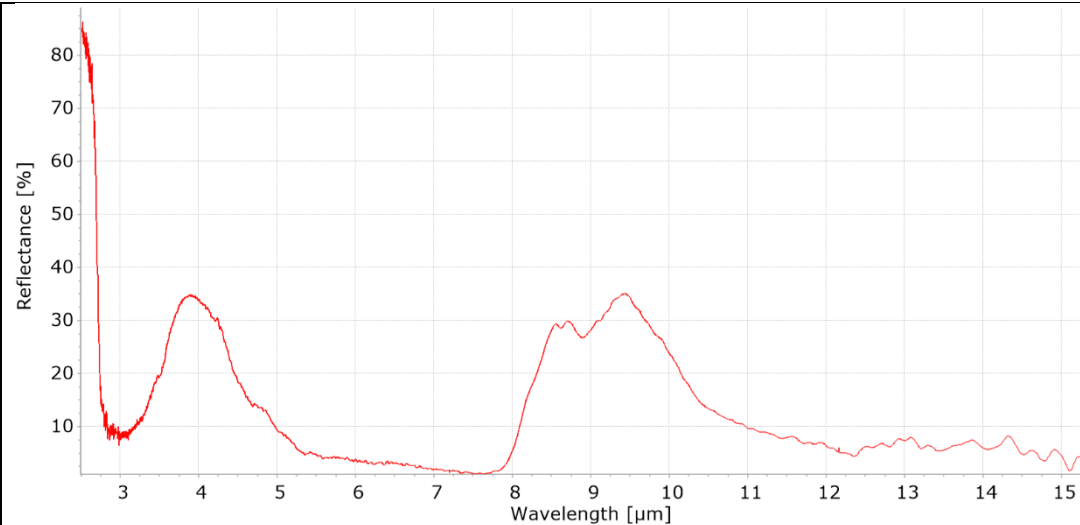
M04104B
Dark spot



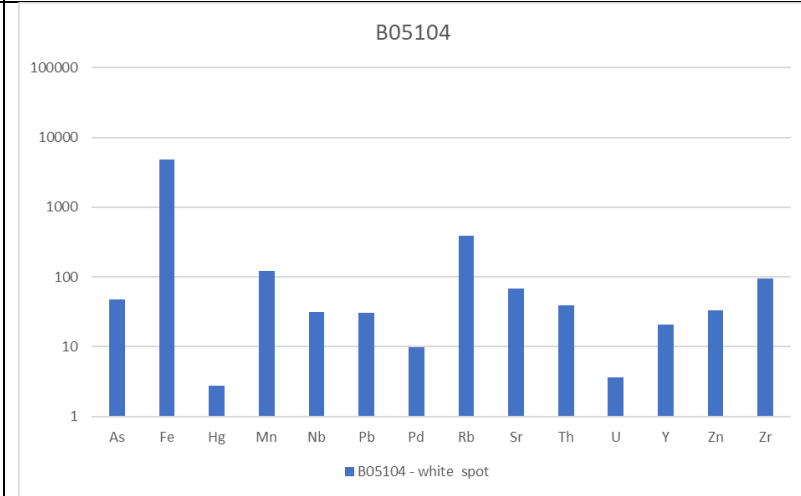
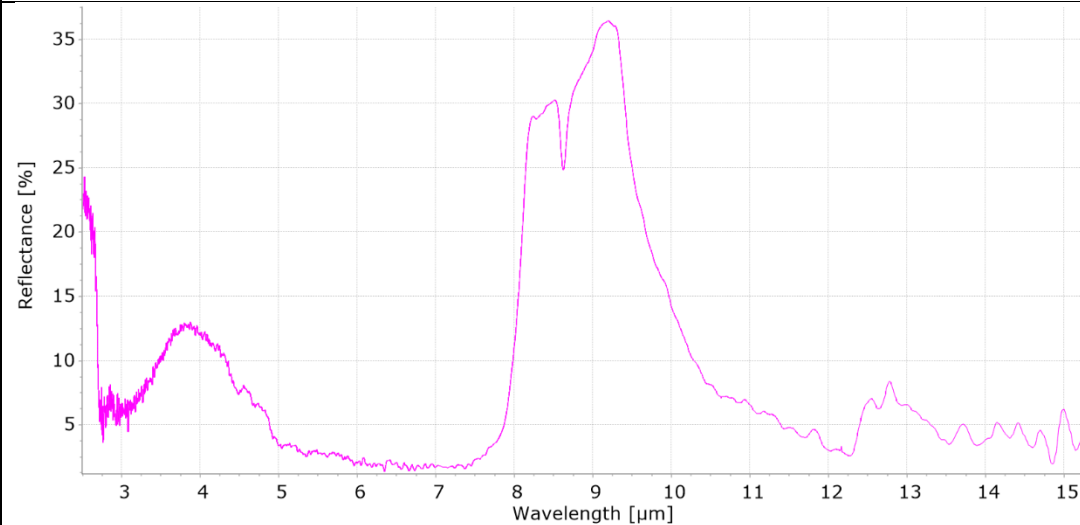
M05101
Yellow spot



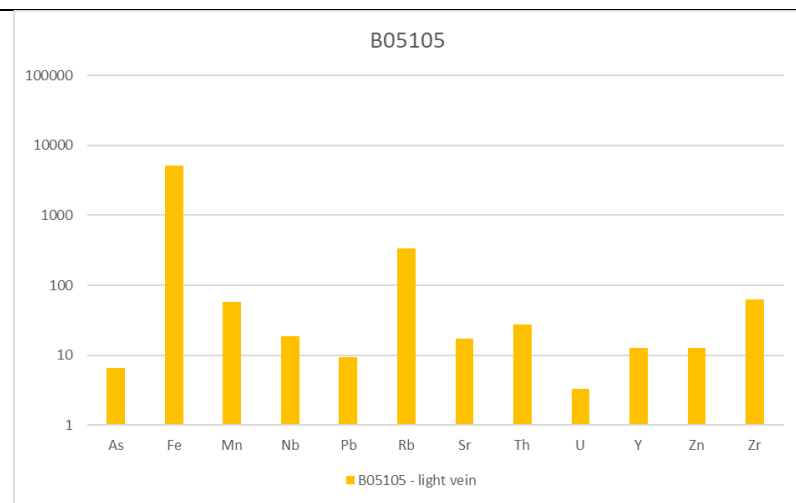
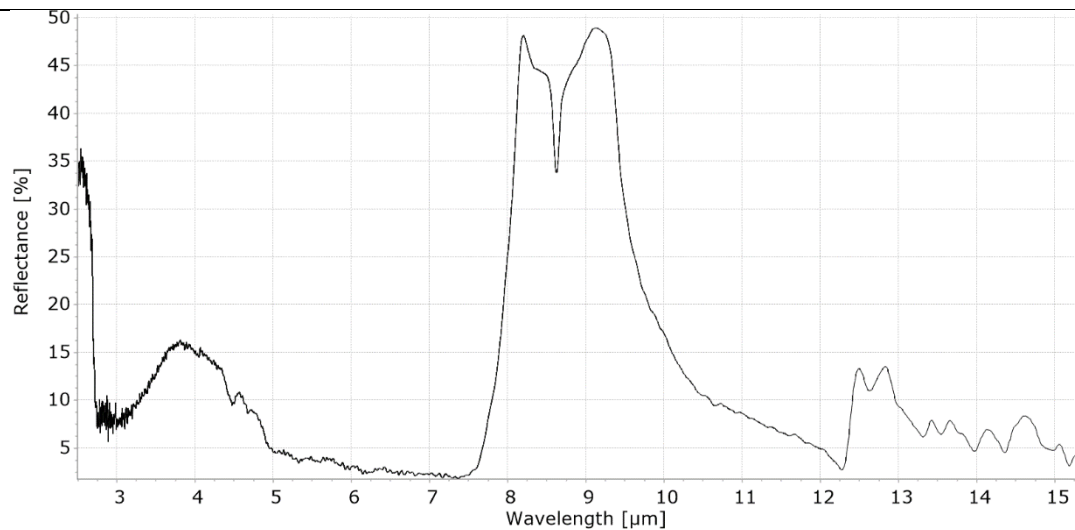
M05103
Dark spot



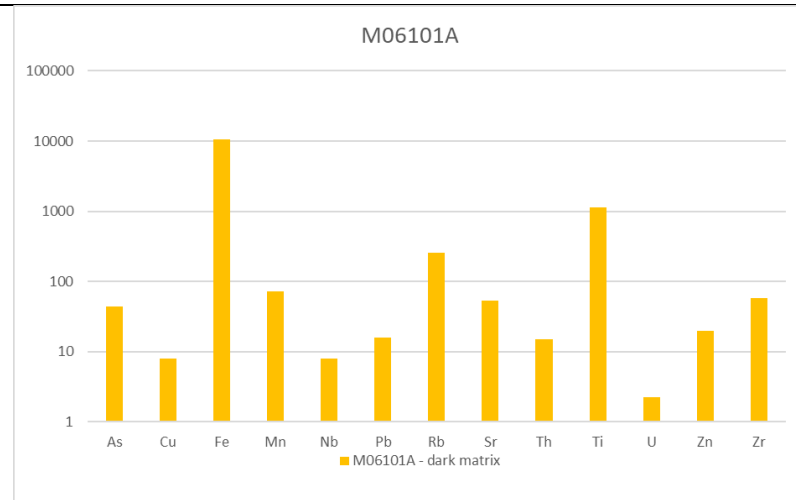
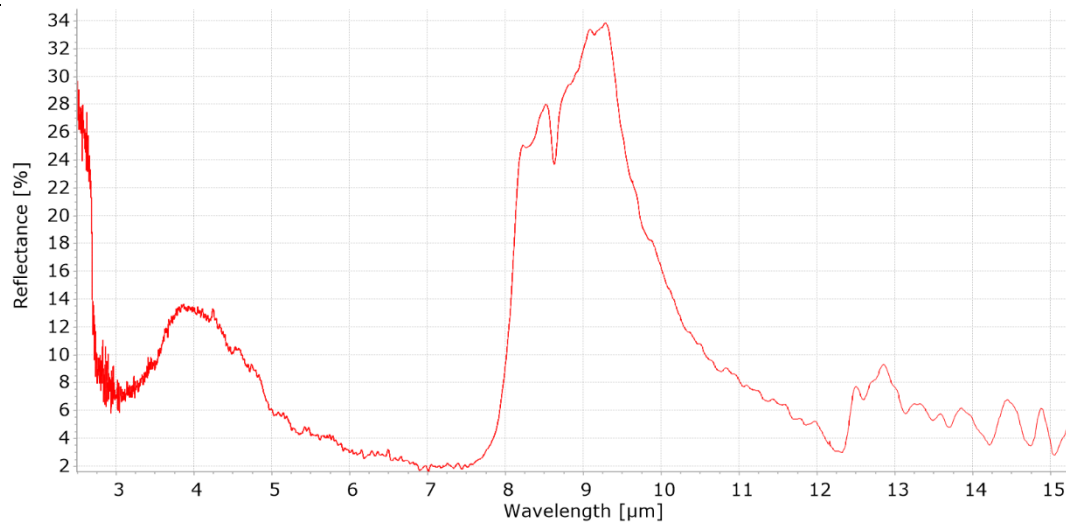
B05104
White spot



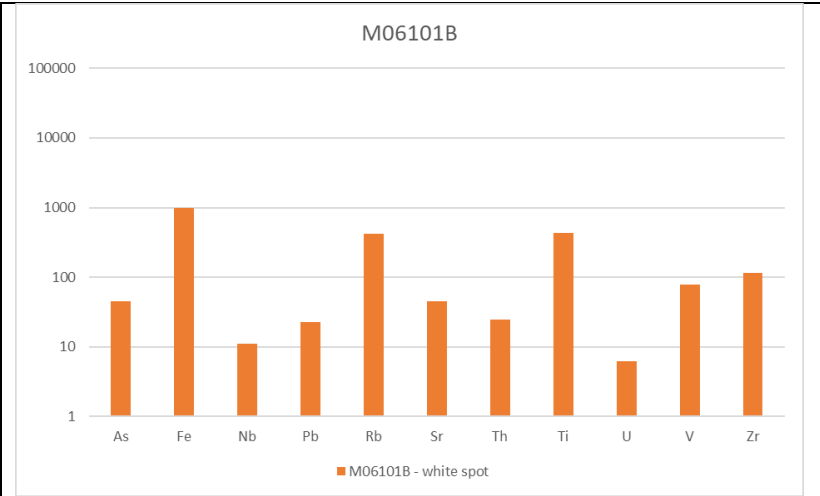
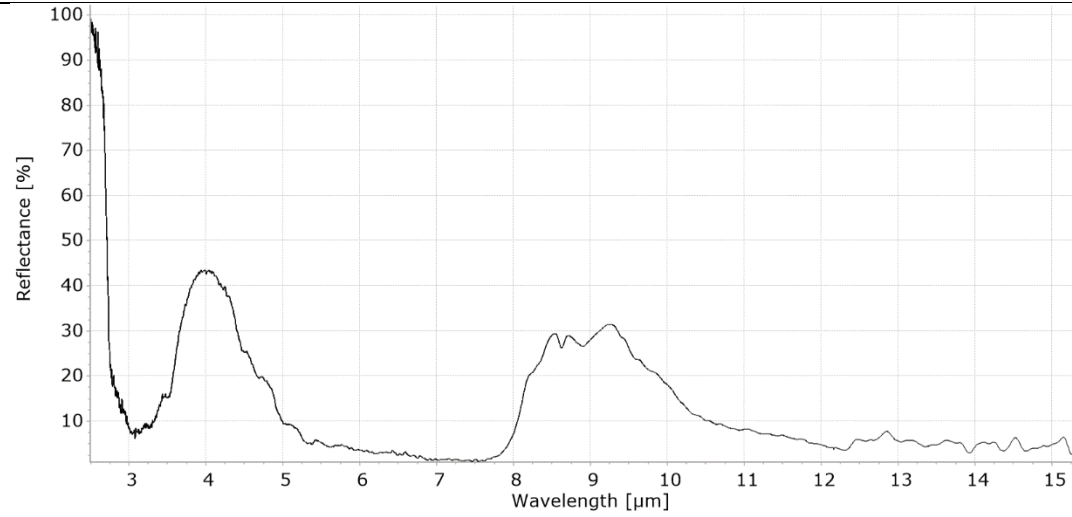
B05105
Light vein



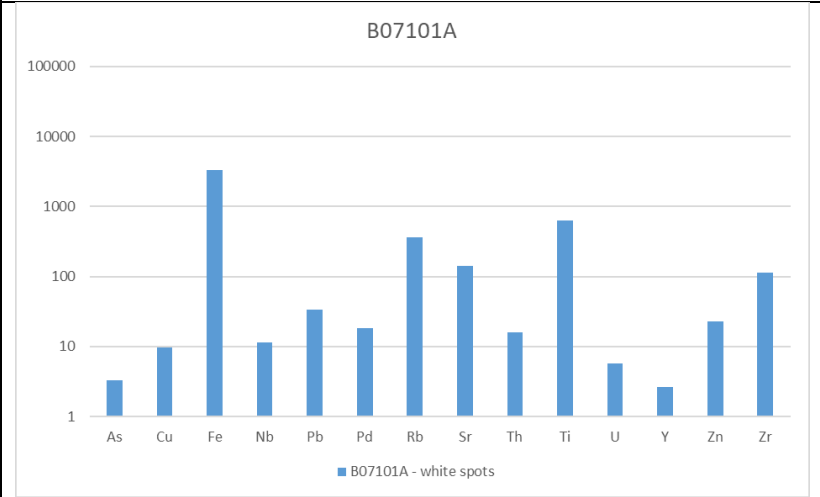
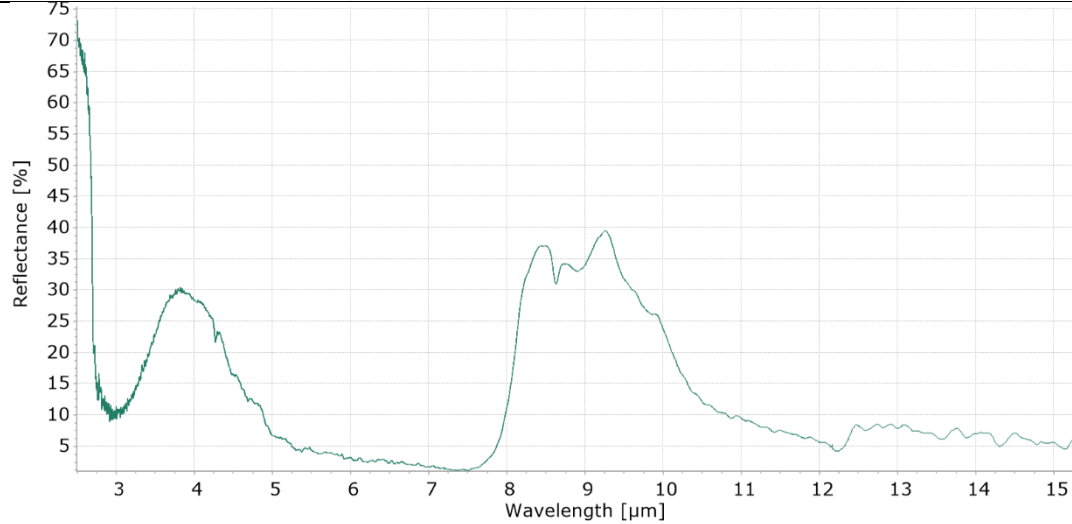
M06101A
Dark matrix



M06101B
White spot



B07101A
White spot

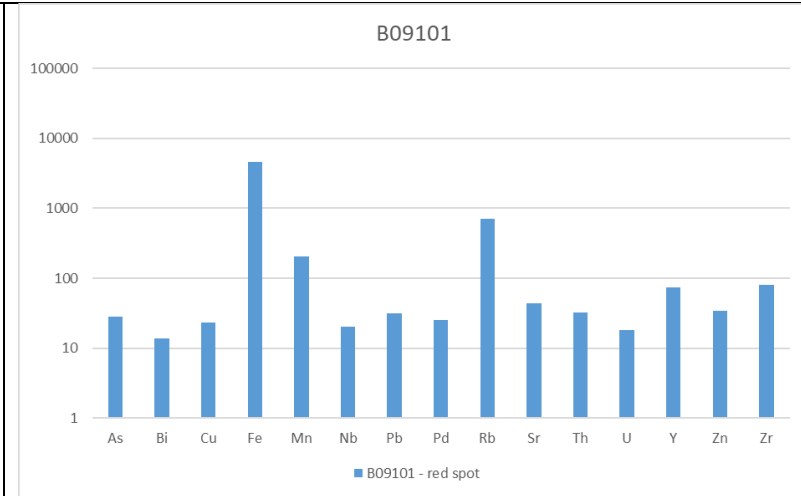
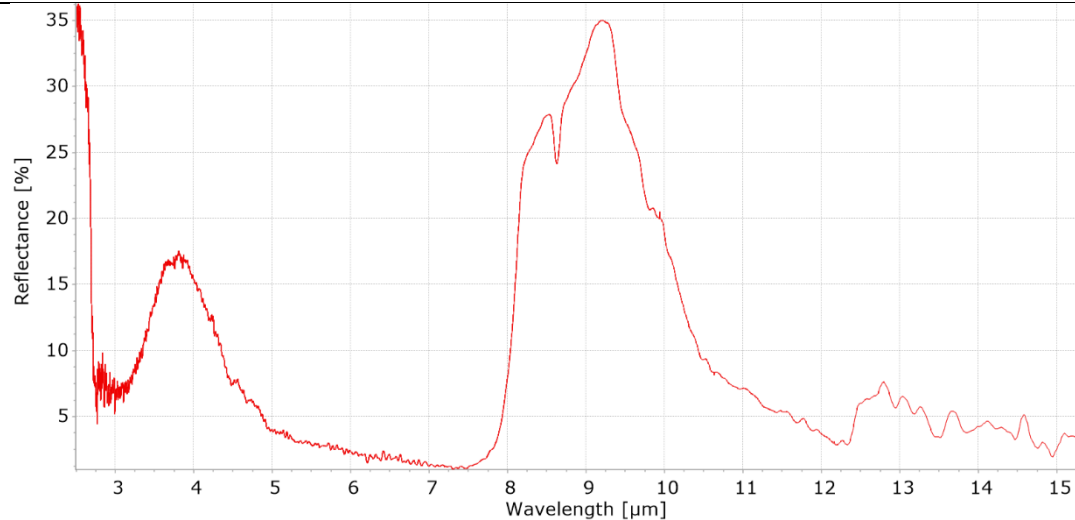


B07101B In results

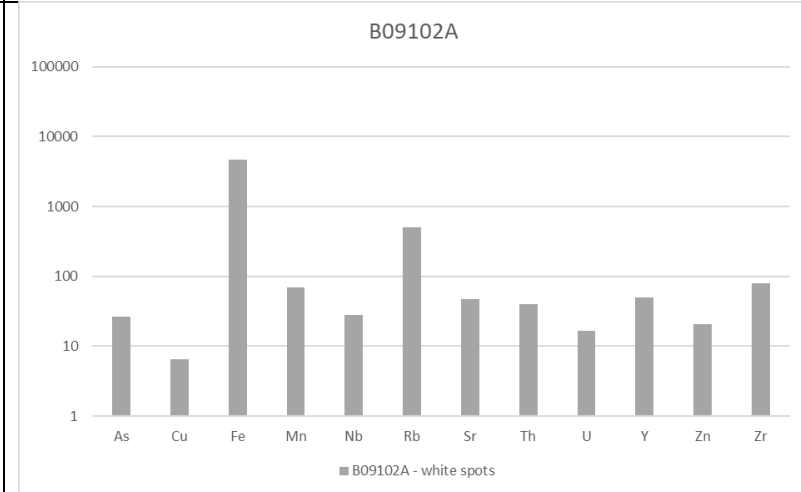
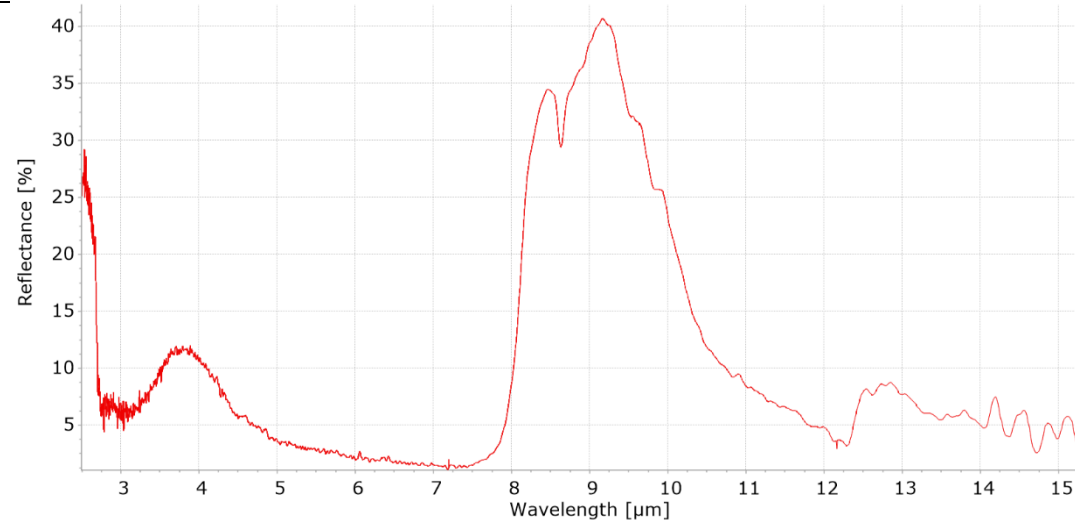
B07102 In results

B07103 In results

B09101
Red spot

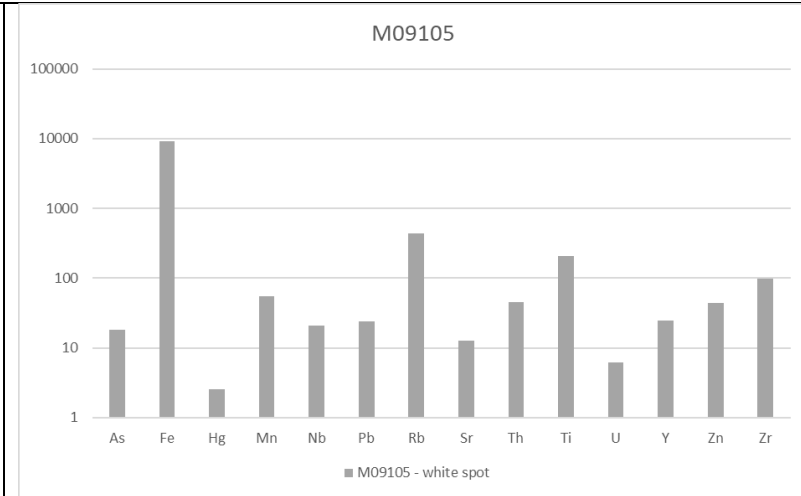
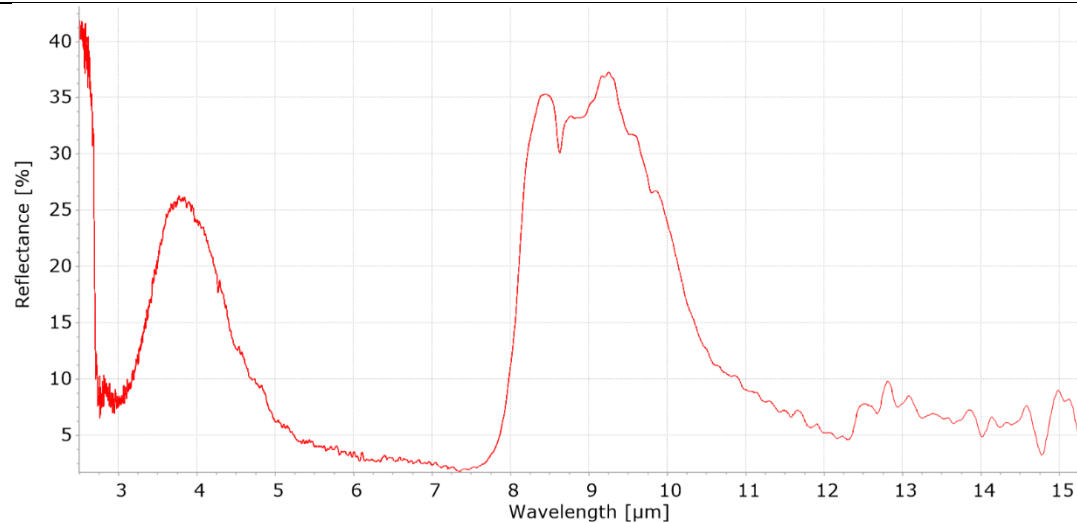


B09102A
White spot

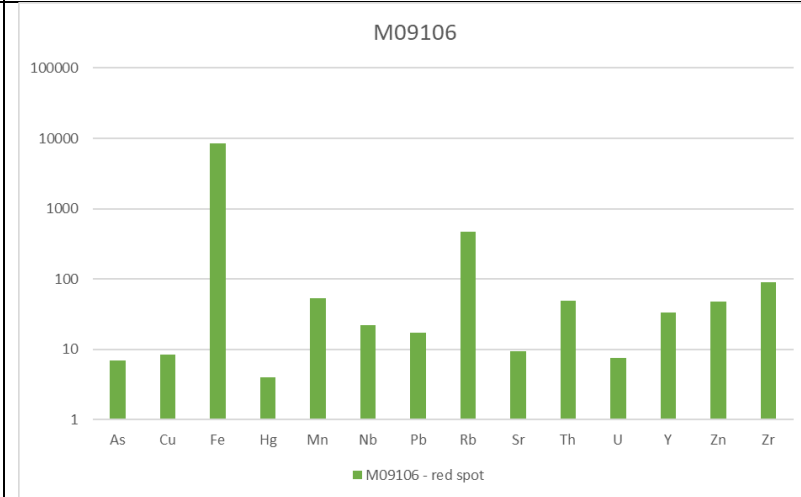
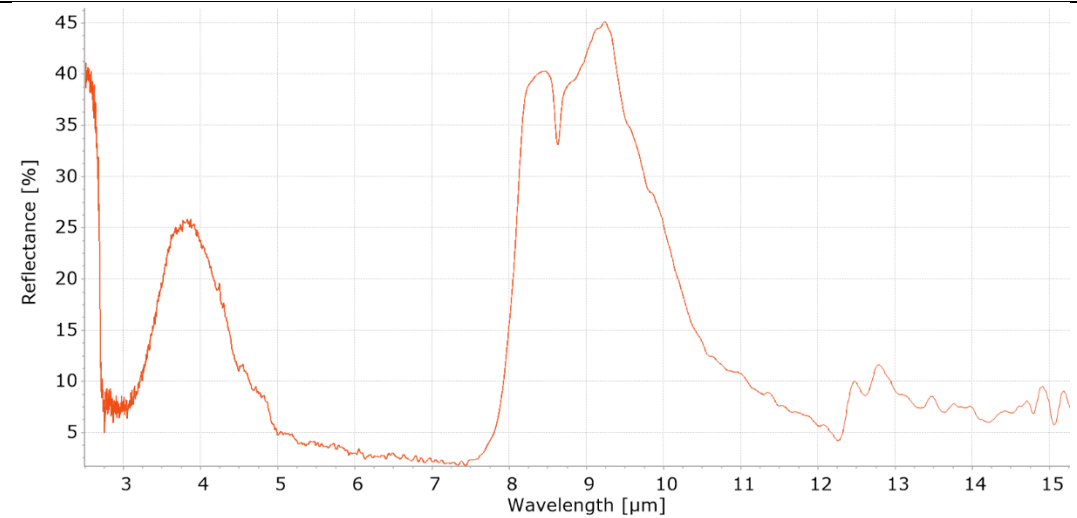


B09104 In results

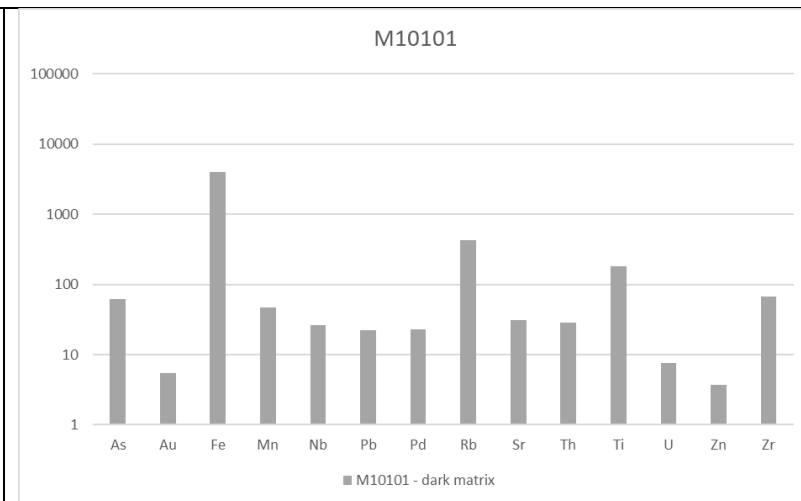
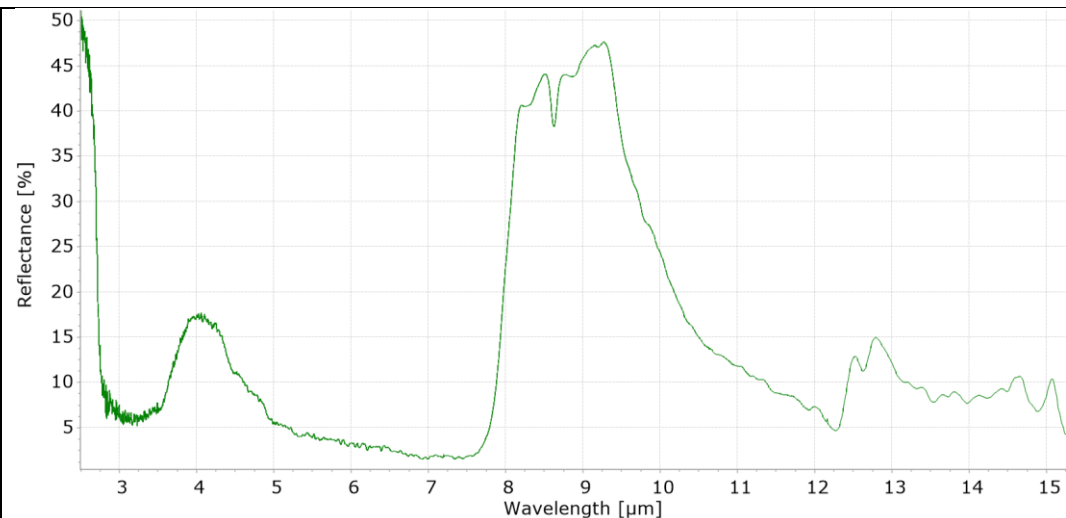
M09105
White spot



M09106
Red spot



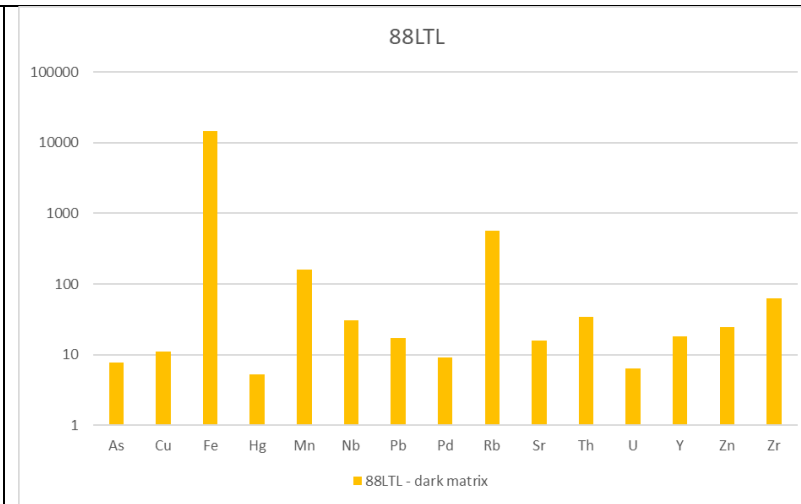
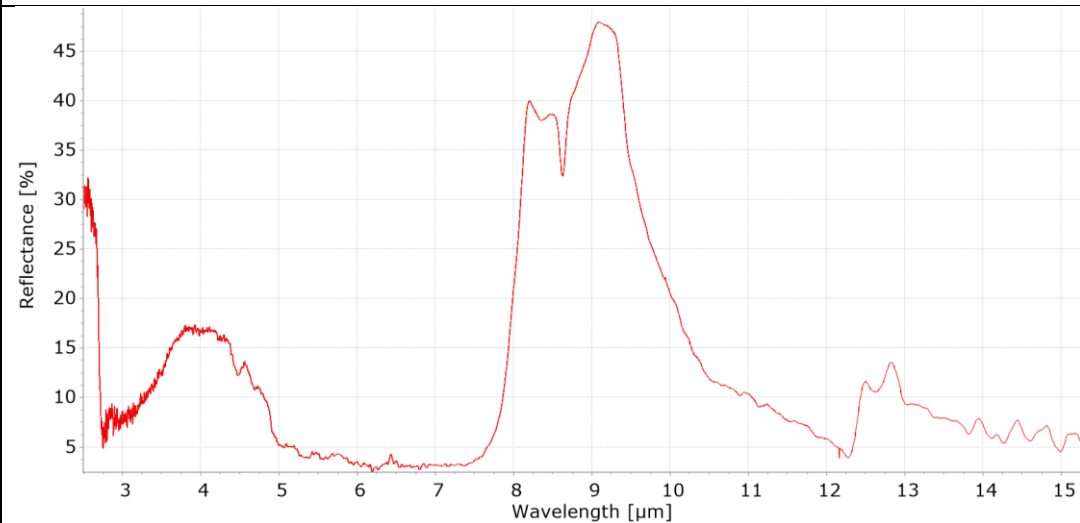
M10101
Dark matrix



84LTL

In results

88LTL
Dark matrix



Appendix 4: Microscopic textural and alteration features

Table 4: Overview of petrological structures. Note: Resorbed quartz phenocrysts and a devitrified matrix are featured in (almost) all samples.

Sample	Granophyric texture	K-feldspar zoning	Sieved/dendritic plagioclase	Foliated matrix	Preferred oriented phenocrysts	Accessory minerals identified	Sericitization
M04104A	✓		✓				✓
M04104B	✓		✓	✓			✓
M05101		✓		✓	✓	✓	
M05103	✓						
B05104							✓
B05105							✓
M06101A		✓	✓			✓	✓
M06101B					✓		
B07101A							✓
B07101B				✓			✓
B07102						✓	✓
B07103					✓	✓	✓
B09101	✓						✓
B09102A	✓						✓
B09104	✓		✓				✓
M09105							✓
M09106	✓						✓
M10101	✓			✓			
84LTL						✓	✓
88LTL							✓

Appendix 5: Table-Top Scanning Electron Microscopy

Table 5: Overview of TTSEM data.

Sample M05101											
Analysis nr.	CO ₂	Na ₂ O	Al ₂ O ₃	SO ₃	SiO ₂	K ₂ O	TiO ₂	FeO	ZrO ₂	PtO ₂	V ₂ O ₅
001			0.19		0.45		99.36				
002			0.89		0.95	0.25	97.02	0.89			
003			0.57		0.71	0.11	97.85	0.75			
004			1.26		1.01		6.08	91.65			
005			0.42		0.39	0.09	98.36	0.74			
Sample M06101A											
Analysis nr.	CO ₂	Na ₂ O	Al ₂ O ₃	SO ₃	SiO ₂	K ₂ O	TiO ₂	FeO	ZrO ₂	PtO ₂	V ₂ O ₅
001							100				
002			1.41		30.13				68.46		
003					30.47				51.86	17.67	
Sample B07102											
Analysis nr.	CO ₂	Na ₂ O	Al ₂ O ₃	SO ₃	SiO ₂	K ₂ O	TiO ₂	FeO	ZrO ₂	PtO ₂	V ₂ O ₅
001			7.22		10.65		82.13				
Sample B07103											
Analysis nr.	CO ₂	Na ₂ O	Al ₂ O ₃	SO ₃	SiO ₂	K ₂ O	TiO ₂	FeO	ZrO ₂	PtO ₂	V ₂ O ₅
001		1.17	1.74		33.91				50.81	12.38	
002			2.59		11.32		86.09				
003		1.54	1.86		34.8				61.8		
004		1.32	1.6		34.38				62.7		
005					30.25				69.75		
006					0.95		96.82				2.23
007			1.86		35.4				62.74		
009			5.36		16.07	0.87	4.7	73			
010			3.22		12.34		84.44				
Sample M10101											
Analysis nr.	CO ₂	Na ₂ O	Al ₂ O ₃	SO ₃	SiO ₂	K ₂ O	TiO ₂	FeO	ZrO ₂	PtO ₂	V ₂ O ₅
001								100			
Sample 84LTL											
Analysis nr.	CO ₂	Na ₂ O	Al ₂ O ₃	SO ₃	SiO ₂	K ₂ O	TiO ₂	FeO	ZrO ₂	PtO ₂	V ₂ O ₅
001			1.99		35.26				50.57	12.19	
002*					29.84				60.18	9.99	
003	27.16				22.49				44	6.34	
004	37.35			43.88				18.77			
*approximately same spot as analysis 001											
Oxides in wt. %											

The EDS spectra and SEM analysis of some of the zircons show significant contents of PtO₂ (6.34 – 17.67 wt.%) (Table 5, yellow marked fields). However, the peaks in the EDS spectra of Zr and Pt are proximally located at 2.042 keV and 2.048 keV respectively (Figure 1), so interference/misinterpretation is common and the supposed PtO₂ content of the zircons is likely to represent additional ZrO₂.

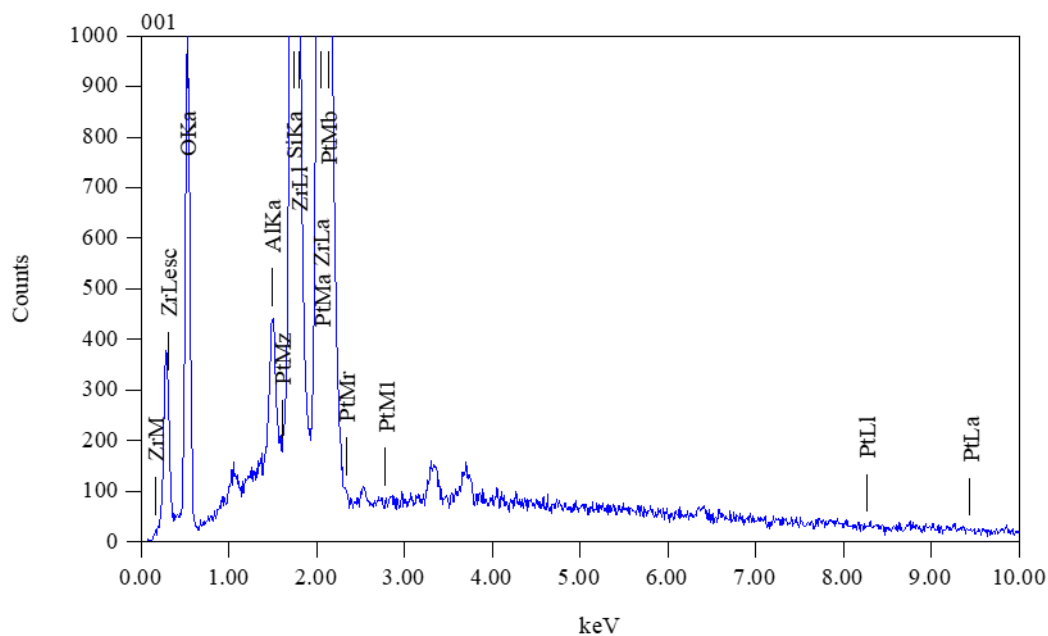


Figure 1: EDS spectrum of analysis nr. 001 from sample 84LTL. Figure 23d from the results section shows analysed zircon crystal.

The concentrations of CO₂, SO₃ and V₂O₅ (Table 5, orange marked fields) that are measured in samples B07103 and 84LTL are the results of sample weathering and (hydrothermal) mineral alteration.